EXPERIMENTS AT THE INTERSECTION OF GEOMETRY, MECHANICS, AND MICROSTRUCTURE

A Dissertation

Presented to the Faculty of the Graduate School

of Cornell University

in Partial Fulfillment of the Requirements for the Degree of

Doctor of Philosophy

by

Jesse L. Silverberg

August 2014

EXPERIMENTS AT THE INTERSECTION OF GEOMETRY, MECHANICS, AND MICROSTRUCTURE

Jesse L. Silverberg, Ph.D.

Cornell University 2014

Using enabling technologies, we examine the role geometry, mechanics, and microstructure play in a variety of systems. This includes 3D time-lapse imaging of growing plant roots, confocal elastography of articular cartilage, the use of origami design principles to make mechanical metamaterials, and quantitative image analysis to study the statistical nature of human collective motion at heavy metal concerts. In each case, these projects explore the underlying mechanisms that lead to emergent macroscopic function and form.

BIOGRAPHICAL SKETCH

Jesse started college as a major in graphic design, but left when he discovered the difference between "art for the sake of art" and "art for the sake of selling a product." After taking some time off, he later returned to school for physics because it would "keep him out of trouble." Five years later, he graduated with three BS degrees from Northeastern University – one each in physics, mathematics, and philosophy – as well as a completed minor in graphic design. Jesse's personal interest in art and music have found outlets in his research on the mechanics of origami, human collective motion at heavy metal concerts, and the innumerable figures he's designed over the course of his PhD at Cornell University.

This thesis is dedicated to all those who encouraged my antics and helped steer me away from trouble.

ACKNOWLEDGEMENTS

I'd like to acknowledge the guidance of my many peers and advisers who have taught me how to be a practicing scientist. Project-specific acknowledgments are included at the end of each chapter.

TABLE OF CONTENTS

LIST OF FIGURES

CHAPTER 1

INTRODUCTION

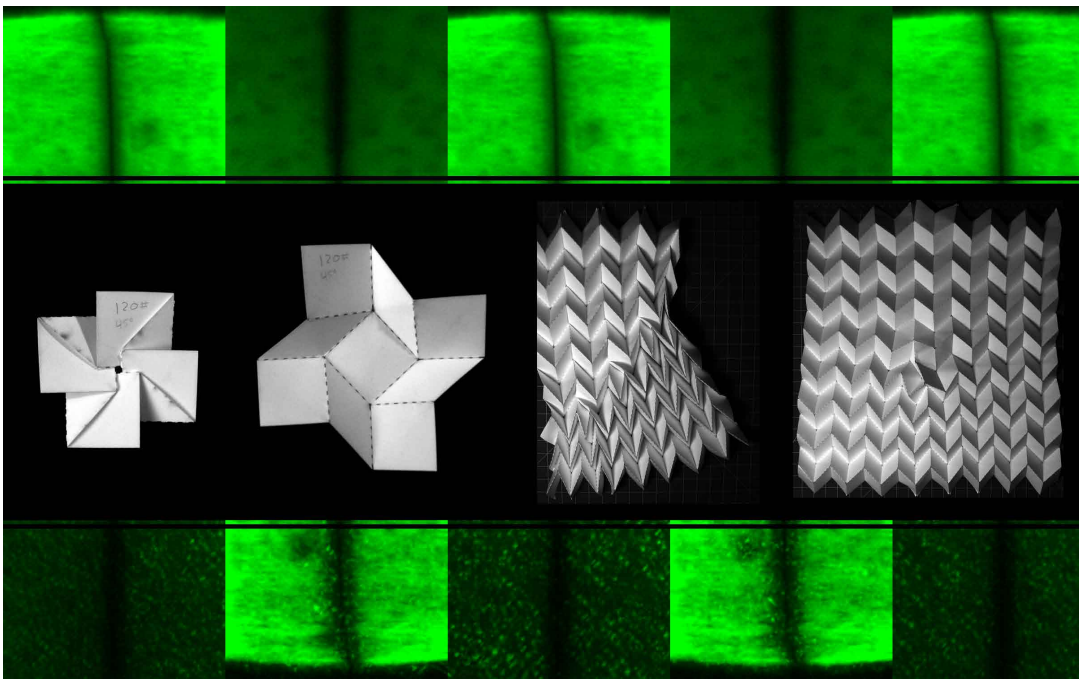

> In every line of inquiry into something that has principles or causes or elements, we achieve knowledge - that is, scientific knowledge - by cognizing them; for we think we cognize a thing when we know its primary causes and primary principles, all the way to its elements. Clearly, then, it is also true in the science of nature that our first task is to determine the principles.
>
> Aristotle, *Physics* (*Φυσικη ακροασις*), Book I

In its earliest conception, the task of understanding the underlying causes and mechanisms of nature was laid out as a fundamental goal of science. Modern thought on this subject has identified two fundamental approaches that

emerge as stylistic opposites. On one hand, *hypothesis-driven science* starts with a core question to be tested, then designs experiments and analyses to check the proposed explanation against a null hypothesis. On the other hand, *exploratory science* sets out to identify patterns in nature and incorporates intuition and luck in order to make new discoveries[1]. In both cases, new technologies can be enabling for progress, though in fundamentally different ways. For example, hypothesis-driven science uses technology to achieve greater precision and accuracy, while exploratory science uses technology to ask new questions.

In this collection of work, there are a number of methods, analyses, and models that are used to study an equally diverse assortment of systems. At times, the work is hypothesis-driven, and others, much more exploratory. In all cases, however, the research is driven by enabling technologies. Whether it be a custom-built 3D time-lapse imaging system to quantify plant root growth, or a laser cutter to fabricate pre-crease-free origami structures, these tools form the experimental backbone of this research.

The title of this thesis refers to three reoccurring themes that appear, in various proportions in, in each chapter. In Chapter 2, the interaction of *Medicago truncatula* roots with physical barriers is investigated. This system can be thought of as a 1D growing filament obstructed by a 2D barrier, all of which is embedded in a 3D elastic medium. Through the use of detailed mechanical modeling, we conclude the plant responds to the barrier by a microstructural rearrangement that twists its tip, ultimately leading to the observed growth patterns. In Chapters 3 and 4, the depth-dependent mechanical properties of carti-

[1]Note, exploratory science is not to be confused with *discovery science*, which acquires large genetic data sets and algorithmically seeks correlations between genes and phenotypes. Implicitly, this is a hypothesis-driven science, as it presupposes that a given phenotype has a genetic cause.

lage are investigated using confocal elastography. The key feature of interest is a highly localized surface region that is 10 to 100 times more compliant than the bulk. Combining mechanical measurements with quantitative polarized light microscopy and Fourier transform infrared imaging, we uncover an unexpected structure-function relationship that we interpret with a microstructural model based on rigidity percolation. In Chapters 5 and 6 we explore origami design principles as a framework for mechanical metamaterial design. By tuning the underlying folding geometry, we find tessellated origami structures can exhibit exotic bulk mechanical properties such as negative Poisson ratio, can have their modulus tuned by orders of magnitude, and can host reversible lattice defects such as dislocations and grain boundaries. We also show that a mechanically bi-stable folded structure known as the square twist exhibits a first order phase transition as a function of the underlying geometry and externally applied load. In chapter 7, we use quantitative image analysis to study human collective motion at heavy metal concerts where we find the statistical motion in *mosh pits* follows a 2D Maxwell-Boltzmann distribution. Using self-propelled particles subject to inter-particle mechanical forces as a model for the crowd, we are able to reproduce the crowds statistical motion. Moreover, the model predicts a vortex-like state that is also observed at these concerts, which it is commonly called a *circle pit*. Finally, in Chapter 8, we close with some broader reflections and remarks about future directions.

CHAPTER 2

3D IMAGING AND MECHANICAL MODELING OF HELICAL BUCKLING IN *MEDICAGO TRUNCATULA* PLANT ROOTS

Jesse L. Silverberg, Roslyn D. Noar, Michael S. Packer, Maria J. Harrison, Christopher L. Henley, Itai Cohen, and Sharon J. Gerbode, *PNAS* **109**, 16794-16799 (2012).

2.1 Abstract

We study the primary root growth of wild-type *Medicago truncatula* plants in heterogeneous environments using 3D time-lapse imaging. The growth medium is a transparent hydrogel consisting of a stiff lower layer and a compliant upper layer. We find that the roots deform into a helical shape just above the gel layer interface before penetrating into the lower layer. This geometry is interpreted as a combination of growth-induced mechanical buckling modulated by the growth medium and a simultaneous twisting near the root tip. We study the helical morphology as the modulus of the upper gel layer is varied and demonstrate that the size of the deformation varies with gel stiffness as expected by a mathematical model based on the theory of buckled rods. Moreover, we show that plant-to-plant variations can be accounted for by biomechanically plausible values of the model parameters.

2.2 Introduction

Plant growth and crop productivity depends on the ability of plant root systems to secure water and nutrients from the heterogeneous terrestrial environment in which they grow. Soil compaction resulting from agricultural activities or from environmental changes such as drought, impedes root growth and consequently has severe negative effects on yield [1]. As world population continues to rise, plant breeding programs are challenged with the need to increase crop yields while facing a decline in agricultural soil quality including increased mechanical impedance of soil. Thus, there is a need to better understand the strategies that roots employ to grow in mechanically heterogeneous environments. Pioneering investigations have described the buckling of roots traversing air gaps in soils [2, 3, 4] and measured the forces generated during root growth [5, 6, 7, 8], however further progress has been hindered by the opaque nature of soil.

Here, we build on recent imaging techniques [9, 10, 11, 12, 13, 14] to investigate the growth of roots through mechanically heterogeneous environments. Our apparatus is distinct in that it employs a laser sheet and a translational stage to rapidly scan the region of root growth. Using this three dimensional (3D) time-lapse imaging system, we observe primary *Medicago truncatula* roots growing through a transparent hydrogel composed of a compliant upper layer and stiff lower layer. The structural heterogeneity in the growth medium allows us to mechanically perturb the root in a controlled fashion. Consistently, we find the roots deform into a helical shape before penetrating into the lower layer as shown in Figure 2.1. Because the length of the helical region is comparable to the length of the elongation zone in *Medicago* plants, it may be supposed that

this morphology is purely a biological process such as circumnutation. However, our analysis reveals that (1) when the root encounters the stiff lower layer, tissue near the root tip twists via a remodeling process and (2) the mechanical buckling of the twisted root within the gel accounts for the observed helical shape. Collectively, these results demonstrate an important example of the interplay between mechanics and morphology during root growth in heterogeneous environments.

2.3 Experimental Procedures

2.3.1 Helical root growth

A two layer medium 8 cm thick was prepared using a transparent isotropic nutrient gel [15] solidified with two different concentrations of Gelrite. Using an Anton-Paar rheometer, we measured the shear modulus and found $G_B \approx 1500$ Pa for the bottom layer and $G \approx 400$ Pa for the top layer (see SI). Thus, the abrupt increase in stiffness at the gel/gel interface forms an elastic mechanical barrier to root growth. Through most of the top layer, roots grew straight down; if present, any root circumnutation was too subtle to observe. Just above the interface however, we observed pronounced helical root deformations as shown in Figure 2.1. Repeating the experiment, we found the general root morphology was reproducible, though each time there were variations in the shape and size of the helical deformations. From our visual inspections, we also noted that 74% of the root helices were right handed while the remaining 26% were left handed (est. uncertainty ±9%).

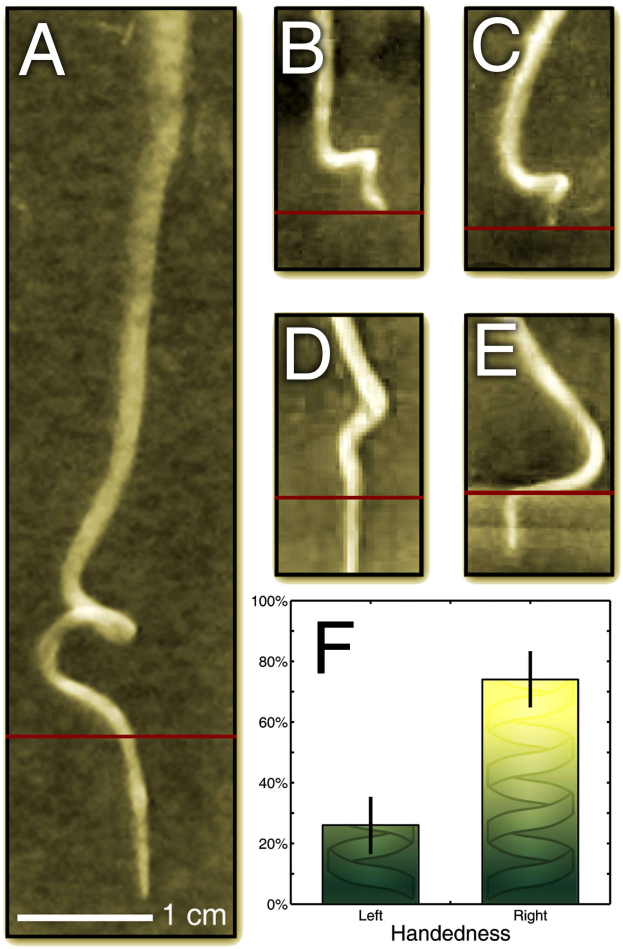

Figure 2.1: (A-E) This gallery of contrast-enhanced digital photographs is a representative selection of the helical root growth observed at the interface of compliant (above red line) and stiff (below red line) gels. They illustrate both the consistency and variation of the phenomenon. (F) The number of left and right handed helices were asymmetrical as shown by the histogram (est. uncertainty $1/\sqrt{N}$).

2.3.2 Mechanical interpretation

Based on our observations, we interpret the helical deformation as a form of mechanical buckling that occurs when the tip's motion is halted by the stiff gel while the root continues to elongate. To investigate how this driving mechanism can lead to the observed root shapes, we developed a simple experimental model consisting of an axially compressed metal rod as a mechanical analog for the root. The rod, a nylon-coated stainless steel wire 0.4 mm in diameter and 8 cm long, was held vertically with the top end fixed to a stationary plate using epoxy. Axial force was manually applied with tweezers by pushing the lower end upward to compress the filament. When the wire is compressed in air, the resulting long wavelength deformation shown in Figure 2.2(A) is consistent with the expected Euler buckling; the deformation occurs in a plane (Figure 2.2(A) inset) and extends the full length of the wire.

In contrast, the root deformations were localized close to the tip (Figure 2.1). To produce this effect in the mechanical model, we embedded the same wire in gelatin (Jell-O) and again applied axial compression from the lower end leading to reversible deformations. As shown in Figure 2.2(B) and inset, localized planar buckling was induced near the region where force was applied. This can be understood in the following manner. Buckling takes a sinusoidal form if the longitudinal stress is uniform throughout [16]. However, the wire surface and gel adhere without slip so that displacements of the wire lead to shear deformations of the gel. Force balance shows that this gel shearing force accumulates along the wire's length, reducing the wire's internal longitudinal stress and attenuating the applied force. Thus, localized buckling occurs when a finite portion of the wire is above the buckling threshold while the rest is below

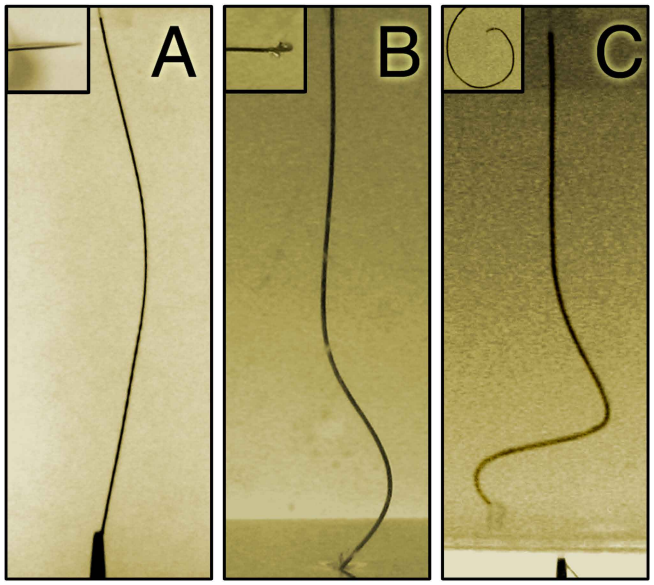

Figure 2.2: As a mechanical analog to root buckling, we axially compressed a metal filament from the lower end. In all images, the top end is epoxied to a plate (clamped boundary condition) while the lower end is held with tweezers (hinged boundary condition). (A) Euler buckling is observed when the filament is suspended in air. (B) Embedding the filament in a gel yields dampened short wavelength oscillations. (C) Twisting the lower end of the gel-embedded-filament while applying compression yields a helical shape similar to the roots. All insets are top-down views and show whether the buckling was planar or 3D.

[17]. In order to produce a 3D helical shape, we added one additional feature: We manually twisted one end of the wire during compression. As Figure 2.2(C) and inset show, this combination of compression and twisting within a supporting medium produced a localized helical deformation like the shape observed in roots.

To check whether a similar twisting mechanism is at play during helical root growth, we fluorescently stained the epidermis of roots with a solution containing 10 μg/mL of 5-DTAF (5-(4,6-dichlorotriazinyl)aminofluorescein) and im-

aged them with a confocal microscope. For roots grown in unlayered gels, cell files were aligned vertically in columns along the entire length of the root (Figure 2.3(A) and inset). In layered gels where the roots encountered the stiff lower layer, cell files were twisted around the axis of the root in the helical region (Figure 2.3(B)), and untwisted everywhere else. The localization of twisting shows that unobstructed root growth generally occurs without a visible pre-existing chirality. Moreover, we extracted and compressed several straight roots, observing planar non-localized buckling in all cases, ruling out internal helicity as a twisting mechanism. Additionally, the distribution of handedness for the root morphology shown in Figure 2.1(F) demonstrates that passive physical instabilities such as those seen during the coiling of poured viscous liquids [18] are insufficient for generating root twisting because they would lead to, on average, equal numbers of either handedness. Finally, we note that differential elongation as currently understood would only produce planar buckling.

Collectively, these observations suggest that the twisting involved in helical buckling arises from a touch-activated biological remodeling in response to axial loads. Though the microscopic dynamics were not observable in our experiments, the process may be related to the thigmotropic-modulated gravitropism previously reported in *Arabidopsis* [19].

2.4 Model

The wire model provides a qualitative understanding of helical root buckling. It is unclear however, whether the mechanistic interpretation of the root as a twisted buckled rod embedded in a gel can capture the plant-to-plant varia-

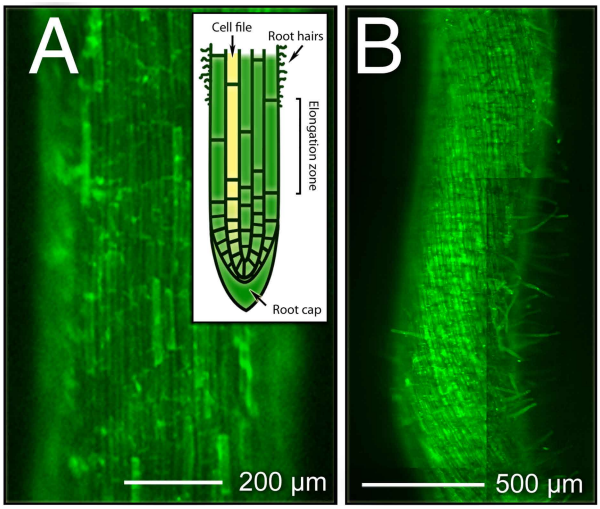

Figure 2.3: Roots were stained and imaged with confocal microscopy to examine the local surface structure. The inset illustrates schematically the developmental physiology of the growth zone in roots. In particular, cells are arranged in vertical columns called *cell files*, which extend from the root cap toward the soil surface. Primary root growth occurs when the cells near the root cap undergo cell division and elongation, adding material within each column. Consequently, the cell file pattern serves as an indicator for the history of root growth. (A) A section of a straight, undeformed root exhibits vertical cell files. (B) In contrast, cell files within the helically-deformed region are wrapped around the roots axis indicating a twisting of the root.

tions typically seen in our experiments (Figure 2.1). Towards this end, we (1) developed an experimental protocol for measuring variations in root morphology, (2) developed a mathematical formulation of the buckled rod model, (3) fitted the model to the data, and (4) determined whether the fitted values of the model parameters are biomechanically plausible.

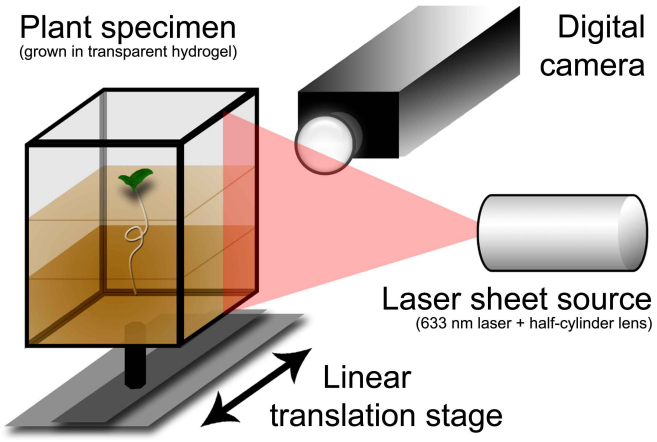

Figure 2.4: This schematic illustration highlights the essential features of the 3D-TIGR apparatus used to quantify helical root buckling. An automated data acquisition program translates the plant specimen through a laser sheet while a digital camera captures a series of images of reflected light. Since the growth medium is transparent, only light scattered off the root is recorded in the scan.

2.4.1 Measurements of root geometry

To quantify the plant-to-plant variations in root morphology, we measured the shape of the helical regions using a unique imaging technique we developed for 3D Time-lapse Imaging of Growing Roots (3D-TIGR). In essence, our apparatus (Figure 2.4) scans the region of root growth with a laser sheet while taking image slices spaced every 0.150 mm. Each scan took less than 5 min. The image slices were then processed in IMARIS 6.0 to create a 3D reconstruction of the root and to extract its spatial coordinates $\langle x(z), y(z), z \rangle$.

The total imaging time for each root growth experiment was approximately 100 h. To establish an experimental protocol for measurement of the helical morphology, we recorded time-lapse movies for 13 roots at a rate of one 3D scan/hour (SM1 - SM3). These movies reveal that when steady growth is im-

peded by the stiff gel, the root abruptly deforms in the transverse direction as expected for a buckled rod. Moreover, because the shape is already helical, root twisting must initiate before buckling. Continued growth leads to the stereotypical shapes shown in Figure 2.1. After the tip penetrates into the lower layer, the radial extent of the helix rapidly shrinks by 30 ± 10% (Figure 2.7). Thus, for the following analysis, we scanned each root after it passed through the barrier, and then linearly scaled the transverse size of the helix by 1.43 to recover the buckled shape before penetration.

To quantify the size of the helical deformation, we defined two length scales, the average vertical extent of the helix $\langle L \rangle$, and the average squared radius of the helix $\langle R^2 \rangle$. These longitudinal and transverse measures are depicted schematically in the insets of Figure 2.5. We calculated $\langle L \rangle$ and $\langle R^2 \rangle$ from the scaled 3D-TIGR root coordinate data using

$$\langle L \rangle = \frac{\left[\int r^2 \, dz\right]^2}{\int r^4 \, dz}, \quad \langle R^2 \rangle = \frac{\int r^4 \, dz}{\int r^2 \, dz}, \tag{2.1}$$

where $r^2 = x(z)^2 + y(z)^2$ is measured from the central axis of the helix, which was oriented to coincide with the z axis. Bounds of the integrals were defined by noting the curvature of $r(z)$ is zero outside the helical region, however, we note Eqs.(2.1) are generally insensitive to the choice of endpoints.

For the gel system shown in Figure 2.1 where $G \approx 400$ Pa, there were substantial root-to-root variations in both $\langle L \rangle$ and $\langle R^2 \rangle$ (Figure 2.5). To gain further insight into the range of possible root morphologies and their dependence on G, we grew 67 plants in gels where the top layer modulus was varied from about 100 Pa to 1500 Pa. For these gels, we saw no apparent dependence of the root radius or length on the modulus, however $\langle L \rangle$ and $\langle R^2 \rangle$ were found to depend inversely on G (Figure 2.5). Furthermore, the spreads in $\langle L \rangle$ and $\langle R^2 \rangle$ at fixed

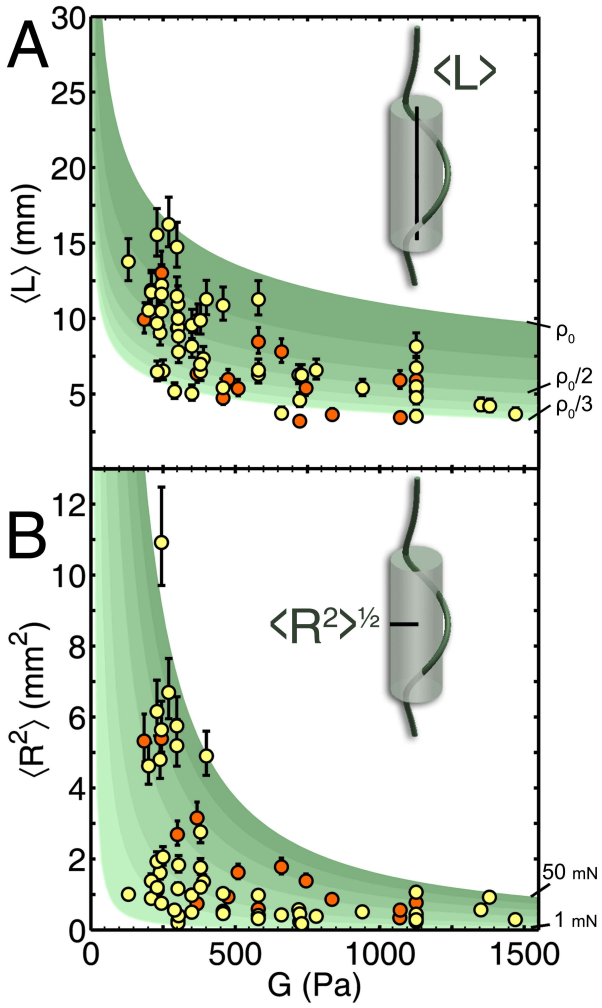

Figure 2.5: Experimental measurements of the (A) longitudinal and (B) transverse length scales of the helical root morphology as defined in Eq.(2.1) are plotted against the top gel layer modulus G. We find that both length scales decrease in stiffer gels, while their variations at a given stiffness tends to increase in compliant gels. The contours were produced by numerical integration of Eqs.(2.2) over a range of parameter values given by the contours shown in Figure 2.6. In particular, the spread in $\langle L \rangle$ was found to correlate with variations in the bending modulus (Figure 2.6(B), green contours), while the spread in $\langle R^2 \rangle$ was found to correlate with variations in the tip compressive force (Figure 2.6(D), green contours). Red data points are roots that violated the small deflection approximation used in the mathematical model.

G are also inversely related to the modulus: at $G \approx 250$ Pa there is a three fold variation in $\langle L \rangle$ and over an order of magnitude variation in $\langle R^2 \rangle$, whereas at $G \approx 1500$ Pa these variations are significantly reduced. Evidently, the root geometry and its variations are strongly dependent on the stiffness of the growth medium.

2.4.2 Theoretical model: development and quantitative fitting

For simplicity, we modeled the root tissue from the helical region as a homogeneous inextensible isotropic cylindrical rod. These assumptions are consistent with experimental observations: (1) root cells are roughly 10^2 times smaller than the typical dimensions of the helix (Figure 2.3), (2) the time scale for growth is much longer than the buckling instability time scale (SM1 - SM3), and (3) neither the material properties nor root radius vary significantly over the length of the helical region [20]. These assumptions allow the rod to be described by a constant bending modulus EI with Young's modulus E and moment of area I. Next, we embed the theoretical rod in a linear elastic gel with shear modulus G. Based on the growth of fine hairs that anchor the root to its growth medium [8, 20], we assume a no-slip boundary condition. For simplicity, we neglect viscoplastic effects in the gel; rheological measurements, elastic relaxation of roots after penetration into the lower gel, and the absence of cavitation bubbles support this assumption. Finally, we specifically focus on variations in root morphology and therefore exclude the dynamic components of touch-activated twisting from our model.

The general data trends can be understood by basic scaling arguments. A

force T_0 greater than the critical buckling force F_c causes a rod to buckle into an arc of length L with amplitude u and bending energy $\sim EI(u/L^2)^2 \times L$. The buckled rod causes a volume $\sim L^3$ of the embedding gel to deform with an energy $\sim G(u/L)^2 \times L^3$. For a fixed force T_0, we minimize the sum of these energies with respect to arc length to find $L \sim \ell$, where the characteristic length scale $\ell \equiv (EI/G)^{1/4}$. Therefore, we expect $\langle L \rangle \sim G^{-1/4}$. Furthermore, the scaled transverse displacement $\langle R^2 \rangle / \ell^2$ increases with the scaled excess force $(T_0 - F_c)/F_0$, where the characteristic force scale $F_0 \equiv [(EI)G]^{1/2}$. Thus $\langle R^2 \rangle$ will have an inverse dependence on G due to the factor of ℓ^2 and because F_0 is larger in stiffer gels. These arguments for $\langle L \rangle$ and $\langle R^2 \rangle$ predict smaller root deformations in stiffer gels. While the experimental measurements qualitatively agree, the data have significant scatter and are too limited in range to test the predicted scaling.

Using a more detailed application of the theoretical rod model, we test whether mechanical buckling can account for the entire morphology of each root as well as the individual variability. Parameterizing the centerline of the rod as $\langle x(z), y(z), z \rangle$, the key mechanical quantities of interest are the longitudinal compressive force $T(z)$ and the axial moment $M_z(z)$. Within the small deflection approximation where the infinitesimal element of arclength $ds \cong dz$, the equations of equilibrium for the transverse forces per unit length are:

$$\begin{aligned} EIy'''' - [M_z(z)x']'' - [T(z)y']' &= -\alpha y, \\ EIx'''' + [M_z(z)y']'' - [T(z)x']' &= -\alpha x. \end{aligned} \tag{2.2}$$

Primes indicate differentiation with respect to z, and $\alpha \approx 2G$ is the effective transverse spring constant per unit length due to the gel elasticity (see SI for detailed derivation). In each equation, the left hand side includes terms for (1) the bending force of the rod, (2) the force required for torque balance when the

centerline is twisting, and (3) the projection of $T(z)$ along the rod's path. To calculate the dependence of $\langle L \rangle$ and $\langle R^2 \rangle$ on the gel modulus, we first determine $T(z)$, $M_z(z)$, and the appropriate boundary conditions.

We find the compressive force $T(z)$ by considering growth just prior to buckling when the tip has made contact with the stiff lower gel. Because growth is obstructed, root elongation, which occurs at the tip, leads to a uniform longitudinal upwards displacement of the entire root. However, fine hairs anchor the root to the embedding gel leading to a downward linear restoring force acting on each portion of the root. Assuming no slip between the root and gel, force balance yields:

$$T(z) = -T_0(1 - z/Z), \tag{2.3}$$

where T_0 is the force applied on the root tip by the lower gel and Z is the length of the root. Eq.(2.3) models the non-uniform compressive force previously discussed.

In roots, the moment $M_z(z)$ arises from the response of individual cells to their local loading conditions and likely results in a remodeling of the root's elastically unstrained reference state. Because the in vivo details are unknown, we take a phenomenological approach and calculate the required moment to produce a given helical morphology by integrating the equations of equilibrium over 20 experimentally measured root contours (see SI). Generally, we find the moment is zero outside the helical region, and non-zero within (Figure 2.8). Following this trend, we approximate the functional form as

$$M_z(z) = M_0 = \text{constant}. \tag{2.4}$$

M_0 has two contributions: (1) the previously discussed remodeling of root tissue, and (2) the root's intrinsic elasticity. While the latter contribution gives

rise to a twist per unit length $\Delta\tau$ beyond the remodeled reference state, both are related to the observed cell file twisting. If elasticity dominates the moment, then $M_0 = C(z)\Delta\tau(z)$, where for a homogeneous isotropic inextensible rod, the torsional rigidity $C(z) = (2/3)EI = \text{constant}$ [21]. Thus, the expression $\Delta\tau(z) = 3M_0/2EI = \text{constant}$ is a bound on the rate of cell file twisting.

To determine the boundary conditions and test the model, we performed an iterative non-linear least-squares fitting of the root coordinate data from the helical region to Eqs.(2.2-2.4). Specifically, we use the Levenberg-Marquardt algorithm to determine the best-fit values for the model parameters EI, T_0, and M_0 as well as the transverse forces and moments at both ends of the fitting interval. This process was repeated for all roots; 49 of the 67 plants had convergent fits (Figure 2.6(A)). Of the nonconvergent fits, an inspection of the complete 3D-TIGR data revealed helical morphologies that violated the small deflection approximation.

From the convergent fits we infer the appropriate boundary conditions. Generally, the transverse forces $F_x \propto x$ and $F_y \propto y$ vanished at both ends. Similarly, the transverse moments $M_x \propto y''$, and $M_y \propto x''$ were smallest at $z = 0$, while the tangent components x' and y' vanished at $z = Z$. Collectively, these results yield a hinged boundary condition ($x, y, x'', y'' = 0$) at the bottom of the rod, and a clamped boundary condition ($x, y, x', y' = 0$) at the top. Additionally, we found the majority of best-fit values for EI and T_0 were spread over two orders of magnitude (Figure 2.6(B) and (D), yellow crosses), while the estimated twist per unit length $3M_0/2EI$ was clustered between 0.1 and 1.0 rad/mm (Figure 2.6(E), yellow crosses).

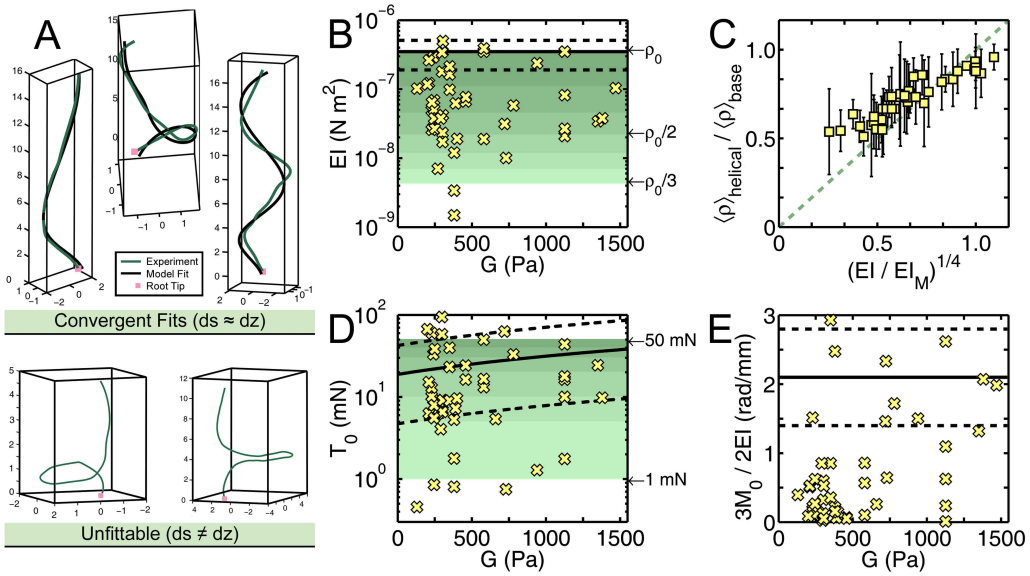

Figure 2.6: This figure shows the results of numerical fits of Eqs.(2.2) to experimental root coordinate data. (A) Examples of best-fits that converged ($ds \cong dz$). In each case, the green curve is experimental data, the black curve is the best fit, the red square is the root tip, and the scale is in mm. In the lower portion, we show root coordinate data which was unfittable due to violations of the small deflection approximation ($ds \ncong dz$). (B) The best-fit values for the bending modulus EI are plotted against G (yellow crosses). The majority of values are spread over two orders of magnitude. Here, ρ_0 is the root radius corresponding to the measured average bending modulus EI_M (solid and dashed black lines). Variations in ρ_0 by up to $1/3$ accounts for most of the spread in the fitted values of EI. Noting that $\rho/\rho_0 = (EI/EI_M)^{1/4}$, these results can be used to predict the tapering of the root radius. (C) Comparing the predicted reduction in root radius $(EI/EI_M)^{1/4}$ to the measured reduction $\langle\rho\rangle_{\text{tip}}/\langle\rho\rangle_{\text{base}}$, we find a correlation confirming that variations in the root radius accounts for the variations in EI. (D) The best fit values for the tip compressive force T_0 are shown as a function of G (yellow crosses). The spread has substantial agreement with estimates based on experimentally observed dimpling of the gel interface (solid and dashed black lines), though various factors can cause T_0 to deviate from these bounds. (E) The best-fit values for the estimated twist per unit length $3M_0/2EI$ are plotted as a function of G. The experimentally measured twist is plotted for comparison (solid and dashed black lines).

2.4.3 Independent checks of fitted parameters

To check whether the values for the fitting parameters are biomechanically plausible, we independently estimated EI, T_0, and M_0. Starting with the bending modulus, we measured EI for 16 roots in a 3-point bending apparatus (see SI). Unfortunately, root tissue from the helical region was too short and fragile to work with. Therefore, we made measurements on the older, more lignified root tissue between the helical growth and the base of the plant. Because this tissue was typically 5-7 days old, it was thicker and easier to work with. Indeed, we measured $EI_M = (3.5 \pm 1.6) \times 10^{-7}$ Nm^2 (SD) (Figure 2.6(B), black solid and dashed lines), which agrees with the upper range predicted by fitting.

Concerning root-to-root variations, it is unlikely that Young's modulus E varies enough to account for the spread in the fitted EI. However, if each root has a distinct radius ρ in the helical region, there can be significant variation in the moment of area $I = (\pi/4)\rho^4$ (Figure 2.6(B), green contours). To investigate this possibility, we assumed E was constant and that differences between the fitted EI and measured EI_M were due solely to ρ. We then calculated the predicted reduction in root radius relative to mature tissue, $(EI/EI_M)^{1/4}$. From the raw 3D-TIGR data, we measured the average root radius in the helically buckled and basal regions to find $\langle\rho\rangle_{\text{helical}}/\langle\rho\rangle_{\text{base}}$. Comparing these quantities, we find a strong correlation confirming that variations in the root radius can account for spread in the fitted EI (Figure 2.6(C)).

While T_0 is difficult to measure experimentally, estimates of its value can be made from deformations in the gel interface induced by the root tip. Detailed calculations [21] show that a point force T_D on a half-infinite elastic medium causes a dimple of depth D and radius ρ. Here, ρ is the same as the root tip

radius. Because we have two elastic mediums, $T_D = 4\pi(G + G_B)D\rho$, where G and G_B are the shear moduli of the top and bottom gel layers respectively. Visual observations show $D \approx 2 \pm 1$ mm, and $\rho \approx 0.50 \pm 0.25$ mm.

Assuming $T_0 \cong T_D$, we estimate the tip force along with upper and lower bounds as a function of the top gel modulus (Figure 2.6(D), black solid and dashed lines). Values range from 5 to 100 mN and agree with 80% of the fits, consistent with the possibility that some of the scatter in T_0 arises from variations in G. Additional estimates based on a Hertz contact or the gel fracture strength are consistent with these results (see SI). Deviations from theoretical expectations can be accounted for by imperfect coupling between the root and the gel or variations in the root tip's angle of attack resulting in a decreased normal force on the gel surface.

To check the range of best-fit values for the moment M_0, we used confocal images to measure the cell file angle with respect to the root axis in the helically buckled region. Imaging several roots, we found an average twist of $\tau_M = (2.1 \pm 0.7)$ radians/mm (SD) (Figure 2.6(E), black solid and dashed lines). Comparing with the fits, we see τ_M overestimates $\Delta\tau = 3M_0/2EI$. This overestimate can be attributed to remodeling of the unstrained reference state wherein an elastically relaxed configuration still exhibits twisted cell files. Root-to-root variation in M_0 can be attributed to differences in the growth rate of individual plants.

Collectively, the range of best fit values for the bending modulus EI, the tip compressive force T_0, and the moment M_0 are consistent with our independent checks and thus biomechanically plausible. These findings demonstrate our simplified mathematical model is capable of quantitatively accounting for the variations observed in the root morphology.

2.4.4 Relating model parameters to root morphology

To identify the connection between variation in specific model parameters and root morphology, we used Eqs.(2.2-2.4) to simulate the dependence of $\langle L \rangle$ and $\langle R^2 \rangle$ on EI, T_0, and M_0. Specifically, we performed sets of numerical solutions while systematically varying the model parameters within the ranges determined by fitting. In our simulation, we increased T_0 until the rod buckled, at which point we evaluated $\langle L \rangle$ and $\langle R^2 \rangle$ from the solution $\langle x(z), y(z), z \rangle$.

Over the experimental range of G, we found that $\langle L \rangle$ depends primarily on EI, $\langle R^2 \rangle$ depends primarily on T_0, while neither depends strongly on M_0. Specifically, we fixed $T_0 = 10$ mN, $3M_0/2EI = 0.45$ radians/mm, and varied EI over the range illustrated by the green contours in Figure 2.6(B) producing a corresponding set of contours for $\langle L \rangle$ as a function of G (Figure 2.5(A)). Similarly, we fixed $EI = 2.2 \times 10^{-8}$ Nm^2, $3M_0/2EI = 0.45$ radians/mm, and varied T_0 over the range illustrated by the green contours in Figure 2.6(D). This produced a set of contours for $\langle R^2 \rangle$ as a function of G (Figure 2.5(B)). The dependence of $\langle R^2 \rangle$ on EI and $\langle L \rangle$ on T_0 was negligible and could not account for variations at fixed G. Finally, we fixed $EI = 2.2 \times 10^{-8}$ Nm^2, $T_0 = 10$ mN, and varied $3M_0/2EI$ from 0.1 to 0.7 radians/mm to produce a set of contours (Figure S3) that showed weak sensitivity of $\langle L \rangle$ and $\langle R^2 \rangle$ on M_0.

From the contours in Figure 2.5 we are able to read off the scaling relations for $\langle L \rangle$ and $\langle R^2 \rangle$. We find $\langle L \rangle \approx 2.7\ell$, and $\langle R^2 \rangle \approx 0.74(\ell/Z)(T_0/F_0)\ell^2$, where ℓ and F_0 are the length and force scales defined previously in the scaling arguments. Indeed, these numerically determined expressions agree well with theoretical expectations.

2.5 Conclusions

Using 3D-TIGR, we studied the helical buckling of *Medicago truncatula* roots due to a physical barrier in their growth medium. This morphology could impact the fitness of *Medicago* plants in at least two ways. First, the helical geometry converts axial loads into transverse loads allowing the root to brace against the surrounding medium and generate a greater force at the tip. Second, touch-activated twisting induced by impenetrable barriers such as rocks leads to a mechanical instability that redirects root growth along the surface of the obstruction [22]. Thus, helical buckling could enhance the root's ability to force through or around physical barriers allowing greater access resources in its environment.

Finally, we speculate that the root geometry observed here may be related to the skewed sinusoidal growth pattern known as *root waving* in which roots growing on tilted 2D surfaces oscillate rather than growing straight down the slope [23, 24, 25]. Though further experiments are necessary, we may discover in time that this growth behavior, along with other plant morphologies, have explanations rooted in the mechanics of growing materials.

2.6 Acknowledgments

The authors would like to thank A. Moore, L. Ristroph, J. Savage, Z. Chen, L. Manning, M. Lapa, M. Haataja, J. Sethna, A. Alemi, B. Davidovitch, C. Orellana, E. Kolb, the Cohen lab and the Mahadevan lab for stimulating conversation. We would also like to thank J. Gregoire and S. Iams for assisting in appara-

tus development, J. Fetcho for kindly allowing us to use Imaris, M. Venkadesan for kindly loaning the translation stage, and J. Puzey for critically reading this manuscript. This work was supported by the National Science Foundation through a Graduate Research Fellowship to J.L.S., grant #IOS-0842720 supporting R.D.N., grant #DMR-1056662 supporting I.C., and Cornell's IGERT Program in Nonlinear Systems (NSF grant #DGE-9870631) supporting S.J.G.. This work was supported by the US DOE through grant #DE-FG02-89ER-45405 supporting M.S.P. and C.L.H., and #DE-FG02-08ER46517 supporting S.J.G..

REFERENCES

[1] T. T. Kozlowski. Soil compaction and growth of woody plants. *Scand. j. for res.*, 14:596–619, 1999.

[2] G. M. Whiteley, J. S. Hewitt, and A. R. Dexter. The buckling of plant roots. *Phsiol. plant*, 54:333–342, 1982.

[3] G. M. Whiteley and A. R. Dexter. The behaviour of roots encountering cracks in soil. *Plant soil*, 77:141–149, 1984.

[4] A. R. Dexter and J. S. Hewitt. The deflection of plant roots. *J. agric. eng. res.*, 23:17–22, 1978.

[5] A. G. Bengough and C. E. Mullins. Mechanical impedance to root growth: a review of experimental techniques and root growth responses. *J. soil sci.*, 41:341–358, 1990.

[6] L. J. Clark, W. R. Whalley, and P. B. Barraclough. How do roots penetrate strong soil? *Plant soil*, 255:93–104, 2003.

[7] G. M. Whiteley, W. H. Utomo, and A. R. Dexter. A comparison of penetrometer pressures and the pressures exerted by roots. *Plant soil*, 61:351–364, 1981.

[8] A. G. Bengough, B. M. McKenzie, and T. A. Valentine. Root elongation, water stresses, and mechanical impedance: a review of limiting stresses and beneficial root tip traits. *J. exp. bot.*, 62:59–68, 2010.

[9] A French and et al. High-throughput quantification of root growth using a novel image-analysis tool. *Plant physiol.*, 150:1784–1795, 2009.

[10] A French, S. Ubeda-Tomás, Tara J Holman, Malcolm J Bennett, and Tony Pridmore. High-throughput quantification of root growth using a novel image-analysis tool. *Plant j.*, 60:1096–1108, 2009.

[11] Anjali S Iyer-Pascuzzi, Olga Symonova, Yuriy Mileyko, Yueling Hao, Heather Belcher, John Harer, Joshua S Weitz, and Philip N Benfey. Imaging and analysis platform for automatic phenotyping and trait ranking of plant root systems. *Plant physiology*, 152(3):1148–1157, 2010.

[12] Randy T Clark, Robert B MacCurdy, Janelle K Jung, Jon E Shaff, Susan R McCouch, Daniel J Aneshansley, and Leon V Kochian. Three-dimensional root phenotyping with a novel imaging and software platform. *Plant physiology*, 156(2):455–465, 2011.

[13] Giovanni Sena, Zak Frentz, Kenneth D Birnbaum, and Stanislas Leibler. Quantitation of cellular dynamics in growing arabidopsis roots with light sheet microscopy. *Plos one*, 6(6):e21303, 2011.

[14] Stefan Mairhofer, Susan Zappala, Saoirse R Tracy, Craig Sturrock, Malcolm Bennett, Sacha J Mooney, and Tony Pridmore. Rootrak: automated recovery of three-dimensional plant root architecture in soil from x-ray microcomputed tomography images using visual tracking. *Plant physiology*, 158(2):561–569, 2012.

[15] Jinyuan Liu, Laura A Blaylock, Gabriella Endre, Jennifer Cho, Christopher D Town, Kathryn A VandenBosch, and Maria J Harrison. Transcript profiling coupled with spatial expression analyses reveals genes involved in distinct developmental stages of an arbuscular mycorrhizal symbiosis. *The plant cell online*, 15(9):2106–2123, 2003.

[16] Clifford P Brangwynne, Frederick C MacKintosh, Sanjay Kumar, Nicholas A Geisse, Jennifer Talbot, L Mahadevan, Kevin K Parker, Donald E Ingber, and David A Weitz. Microtubules can bear enhanced compressive loads in living cells because of lateral reinforcement. *The journal of cell biology*, 173(5):733–741, 2006.

[17] Moumita Das, Alex J Levine, and FC MacKintosh. Buckling and force propagation along intracellular microtubules. *Epl (europhysics letters)*, 84(1):18003, 2008.

[18] George Barnes and Richard Woodcock. Liquid rope-coil effect. *American journal of physics*, 26(4):205–209, 2005.

[19] Gioia D Massa and Simon Gilroy. Touch modulates gravity sensing to regulate the growth of primary roots of arabidopsis thaliana. *The plant journal*, 33(3):435–445, 2003.

[20] M Schwarz, P Lehmann, and D Or. Quantifying lateral root reinforcement in steep slopes–from a bundle of roots to tree stands. *Earth surface processes and landforms*, 35(3):354–367, 2010.

[21] L. D. Landau and E. M. Lifshitz. *Itheory of elasticity*. Pergamon, New York, 3rd edition, 1986.

[22] Matthew V Thompson and N Michele Holbrook. Root-gel interactions and the root waving behavior of arabidopsis. *Plant physiology*, 135(3):1822–1837, 2004.

[23] Kiyotaka Okada and Yoshiro Shimura. Reversible root tip rotation in arabidopsis seedlings induced by obstacle-touching stimulus. *Science*, 250(4978):274–276, 1990.

[24] Michele Oliva and Christophe Dunand. Waving and skewing: how gravity and the surface of growth media affect root development in arabidopsis. *New phytologist*, 176(1):37–43, 2007.

[25] Fernando Migliaccio, Alessio Fortunati, and Paola Tassone. Arabidopsis root growth movements and their symmetry. *Plant signal. behav*, 4:183–190, 2009.

2.7 Supplemental Information

In the following supplemental materials, we provide additional details relating to our experimental observations of helical root buckling as well as explicit calculations to guide the reader through our mathematical model. This material is not necessary to understand the flow of the main text, however, it attempts to provide extra insights the reader may find useful.

2.7.1 Heterogeneous gel preparation

To prepare the two-layer gel growth medium, first a 3 cm layer containing 5.00 g/L of Gelrite was poured into a $6.5 \times 6.5 \times 8$ cm^3 Magenta box and allowed to set for 3 hours. Subsequently, a second 5 cm layer was poured with 2.50 g/L of Gelrite to yield a more compliant upper layer. To systematically study the root morphology and its dependence on the upper gel layer stiffness, we varied the concentration of Gelrite from 1.25 g/L to 5.00 g/L. When measuring the gel's rheological properties, we varied the shearing frequency from 1 to 100 Hz. Over this range, the elastic moduli G quoted in the text were independent of

frequency and larger than the loss modulus by approximately two orders of magnitude.

2.7.2 3D-TIGR

Before imaging, wild-type *Medicago truncatula* seedlings were germinated and the growth medium was prepared as described previously [1]. Forming the layered hydrogel growth medium in a Magenta box, the seedlings were planted and the sample container was mounted on a linear translation stage controlled by a Parker Hann Corp GV-U6E servo drive that was aligned to move the specimen through a laser sheet. To produce the laser sheet, we employed a 633 nm Thorlabs HRR050 laser and a half-cylinder lens. The laser sheet, linear stage, and stepper motor were enclosed in a growth chamber with a computer-controlled growth light. In a sequence of actions executed by LabVIEW 8.20 using a National Instruments PCI-6220 DAQ, our automated data acquisition program collected image slices of the growing root at regular intervals. Specifically, once an hour the program turned off the growth light and repeatedly stepped the translation stage by 150 μm while recording a digital image of the reflected laser light with an Allied Vision Technologies Marlin F-080C USB camera. Each complete scan took less than 5 minutes and produced a series of image slices along the translation axis with a voxel resolution of $66\times66\times150\ \mu m^3$. These images were reconstructed using IMARIS 6.0 to form a 3D visualization of the root's growth in space and time. The coordinates of the root for each frame were then extracted using the IMARIS filament-tracking algorithm and exported for analysis in MATLAB 7.0.

2.7.3 Relaxation of roots

From the 3D-TIGR data, we found that the transverse deflection $\langle R^2 \rangle$ (see Eq.(2.1) in the main text) tended to increase after the onset of buckling. This continued until the root tip penetrated into the lower layer, an event which coincided with a sudden decrease in $\langle R^2 \rangle$ which we interpret as an elastic relaxation of the root-in-gel system (Supplemental movies SM1, SM2, and SM3). Measurements of $\langle L \rangle$ and $\langle R^2 \rangle$ at the moment of maximum deformation and long after the elastic relaxation showed that $\langle L \rangle$ was essentially uneffected while $\langle R^2 \rangle$ decreased to nearly 70% its maximum value. Figure S2.7 shows data taken from 11 plants along with a linear fit. As described in the main text, we use this relation to rescale the root coordinate data to an earlier point in time, just before the root passed through the barrier.

2.7.4 Measuring the bending modulus of roots

To measure the bending modulus EI_M of *Medicago* roots, sections of 5-7 day old undeformed root tissue $2 \sim 3$ cm in length and roughly constant radius ($\rho \approx 0.3 - 0.4$ mm) were clamped at both ends and immersed horizontally in a water bath. Small stainless steel or copper weights were hung at the center of the root and digital photographs were taken of the resultant deflection δu. Using software written in MATLAB, the deflection was measured as a function of the applied force δF with corrections made to account for a small, but non-zero, buoyant force. Staying within the regime where deflection was linear with force, we used

$$EI_M = \frac{Z^3}{192} \frac{\delta F}{\delta u}, \tag{2.5}$$

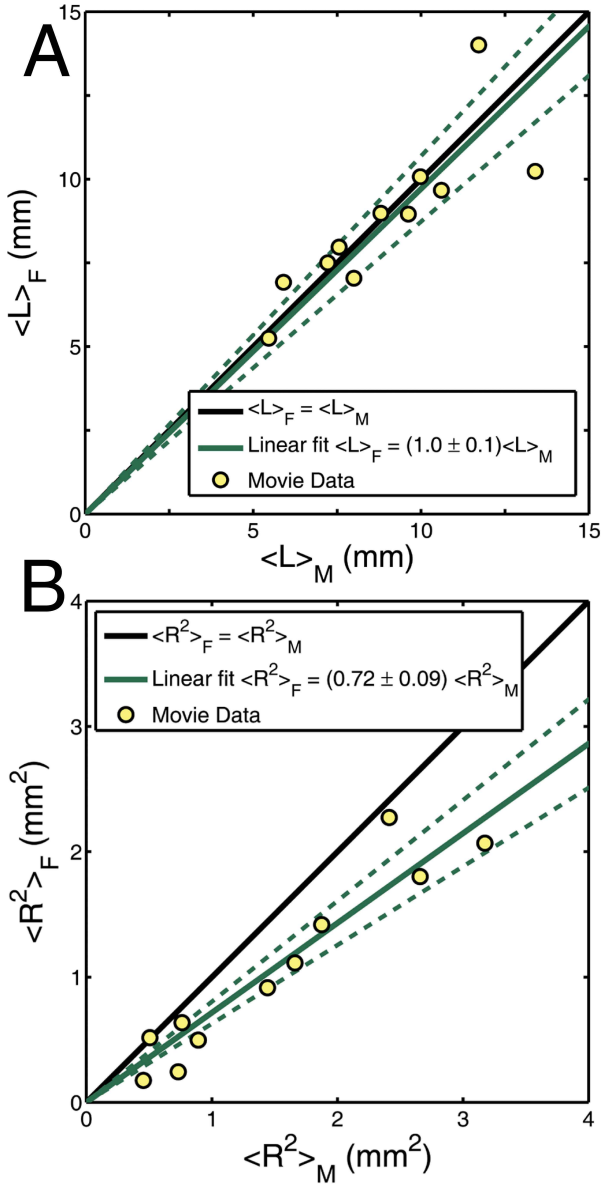

Figure 2.7: Noticing that the roots elastically relax after penetrating into the lower layer, we used 3D time-lapse movie data to identify the moment of maximum deformation. Measuring $\langle L \rangle_M$ and $\langle R^2 \rangle_M$ at this time and comparing to the values of the roots' final configuration, $\langle L \rangle_F$ and $\langle R^2 \rangle_F$, we found that (A) the longitudinal extent was largely unaffected while (B) the transverse size decreased to nearly 70% it's maximum size.

where Z was the length of root being measured, to calculate the bending modulus [2]. Averaging over 16 roots, we found $EI_M = (3.5 \pm 1.6) \times 10^{-7}$ Nm^2. In our measurements, the deflection of the roots was found to be symmetric about the point of applied force. This suggests that the bending modulus is reasonably constant over the region studied. Furthermore, because the roots used were nearly one week old, their radius ρ was larger than young root tissue found near the tip. Thus, we expect the measured value reported here to be an upper bound for the root tissue subject to helical deformations.

2.7.5 Detailed scaling arguments

In the main text, we presented two scaling arguments to determine how the measured quantities $\langle L \rangle$ and $\langle R^2 \rangle$ depend on the mechanical properties of the system. We provide here a more detailed step-by-step approach. To begin, we consider a rod embedded in a gel without slip such that deflections of the former induce deformations of the the latter. Both the rod and gel are treated as linearly elastic, homogeneous, isotropic, and incompressible, so that the mechanical quantities of interest are the rod's bending modulus EI and the gel's shear modulus G. Next, we suppose the rod is subject to an axial load and moment such that a localized helical buckling is induced (i.e., Figure (2.2) in the main text). This geometry has a characteristic length L and amplitude u. Because the system is buckled, the end-to-end distance of the buckled region will be shorter than the total arc length by an amount $\delta_z \sim (u/L)^2 \times L = u^2/L$. For a fixed δ_z, we seek expressions for L and u.

To determine the scaling of $\langle L \rangle$, we consider the rod's bending energy per

unit length, which is proportional to the bending modulus times the curvature squared,

$$U_{\text{rod}}/L \sim EI\left(\frac{u}{L^2}\right)^2 = EI\frac{\delta_z}{L^3}. \tag{2.6}$$

Because the rod and gel are coupled without slip, a volume of gel will be sheared by the rod's deformations. In the frame of the undeformed system, the volume affected will scale as $\sim L^3$, and the corresponding strain energy density will be

$$U_{\text{gel}}/L^3 \sim G\left(\frac{u}{L}\right)^2 = G\frac{\delta_z}{L}, \tag{2.7}$$

where the strain $\sim u/L$. This expression can be reexpressed as a more familiar Hookean-spring type formula: $U_{\text{gel}} \sim (GL)u^2$. Here, GL is the effective spring constant of the rod in gel, and u is the gel's displacement. Thus, the total energy of the rod and gel will scale as the sum of Eqs.(2.6) and (2.7):

$$U_{\text{tot}} \sim EI\frac{u^2}{L^3} + GLu^2 - T\delta_z, \tag{2.8}$$

where the third term is the work done by the external force T that induces buckling. For a deflection with fixed δ_z, the length L that minimizes Eq.(2.8) is given by $L \sim (EI/G)^{1/4} \equiv \ell$. Here, ℓ can be interpreted as the natural length scale determined by the mechanical quantities of the system. Noting that the experimentally measured $\langle L\rangle$ is comparable to the characteristic length of the deformation L we conclude $\langle L\rangle \sim G^{-1/4}$.

To find an analogous scaling relation for $\langle R^2\rangle$, we substitute the expression for L that minimizes the energy back into Eq.(2.8), $U_{\text{tot}} \sim (F_0 - T)\delta_z = -\Delta F\delta_z$, where $F_0 = \sqrt{(EI)G}$ is the natural force scale of the system. Just beyond the buckling threshold when ΔF is small, higher-order terms in δ_z arising from the rod's inextensibility, which were previously considered small, become important. The first correction to the rod's arc length is $\sim (u/L)^4 \times L = \delta_z^2/L$, so that

the total energy is $U_{\text{tot}} \sim -\Delta F \delta_z + c F_0 \delta_z^2 / L$, where c is a constant of order unity. Minimizing with respect to δ_z yields

$$\left(\frac{u}{\ell}\right)^2 \sim \frac{\Delta F}{F_0}. \tag{2.9}$$

The experimentally measured transverse deflection $\langle R^2 \rangle$ is, by definition, a measure of u^2. Therefore

$$\frac{\langle R^2 \rangle}{\ell^2} \sim \frac{\Delta F}{F_0}. \tag{2.10}$$

Eq.(S2.10) shows $\langle R^2 \rangle \sim \ell^2 (\Delta F / F_0)$, or in terms of the shear modulus G,

$$\langle R^2 \rangle \sim \frac{1}{G}. \tag{2.11}$$

Thus, the magnitude of the transverse deflections becomes smaller as the gel stiffness increases.

2.7.6 Explicit derivation of the buckled rod model

To model the helical root morphology observed in our experiment, we used a theory describing twisted elastic rods subject to compression. Though the equations of equilibrium were quoted in the main text, we provide a detailed derivation here to clarify the result. Our approach follows Landau and Lifshitz [2].

We begin by abstracting the root-in-gel system to that of an incompressible rod embedded in a gel and anchored in such a fashion as to prevent "slippage" through the surrounding medium in both the transverse and longitudinal (axial) directions. The rod has a circular cross section of radius ρ_0, length Z, and its position in space is given as a function of arclength s by the vector $\vec{r}(s) = \langle x(s), y(s), z(s) \rangle$. If an infinitesimal length of the rod is $ds = (dx^2 + dy^2 + dz^2)^{1/2}$,

then the unit vector tangent to $\vec{r}$ is $\hat{t} = d\vec{r}/ds$. While this vector can be used to describe bending, it does not account for twisting of the rod about its axis. For this, we use $\phi(s)$ to express the net angle by which each part of the rod has been rotated. The amount of turning per unit length, or its *torsion*, is

$$\tau(s) = d\phi/ds. \tag{2.12}$$

Two key quantities to describe the mechanical equilibrium of the rod are the local internal force $\vec{F}(s)$ and the local internal moment (torque) $\vec{M}(s)$. Indeed, these two functions are used to relate the externally imposed forces and moments to the bending and twisting of the rod. We do this by first expressing the moment in terms of the rod's deformations through its elastic constants

$$\vec{M} = EI\hat{t} \times \frac{d\hat{t}(s)}{ds} + M_z(s)\hat{t}, \tag{2.13}$$

The first term on the right represents bending and is proportional to the curvature $d\hat{t}/ds$, while the second term represents twisting and is the projection of the total vectoral moment along the rod's axis. For a homogeneous, isotropic, and incompressible rod, the bending modulus EI is the product of Young's modulus E and the moment of area $I = (\pi/4)\rho_0^4$.

At least two additional features could be added to the model regarding the torsional moment $M_z(s)$. First, the actual root is lengthwise anisotropic and could be approximately treated as a fiber composite in which each root cell file is inextensible. If the cell files are twisted, then we would expect a twist/extension coupling in the root's elastic response. Though we mention this possibility, our model does not include twist/extension coupling because our experiments were unable to resolve the microscopic details of twisting during growth. Thus, our model remains agnostic to the dynamics during growth and focuses on the static structure of the root instead.

A second possible feature to add to the model would be the effect of biological remodeling of the root tissue. In this case, we would use the expression $M_z(s) = C(s)(\tau(s) - \tau_0(s)) = C(s)\Delta\tau(s)$. Here, $C(s)$ is the torsional elastic constant, $\tau(s)$ is the rotational strain, and $\tau_0(s)$ is the rotational strain reference state. While both rotational strains are measured with respect to an untwisted configuration (in units of radians/length), the reference state represents the effect of remodeling by shifting the elastically unstrained state. Thus, for non-zero $\tau_0(s)$ in the absence of any external moments, a rod would appear to be twisted, yet experience no elastic strain because it is in the relaxed configuration. Because the reference state $\tau_0(s)$ is not observable in our experiments, we formulate the equations of equilibrium in terms of $M_z(s)$ only. When interpreting our results in the main text, we compare $\Delta\tau$ to the observed cell file twisting in an effort to determine the biomechanical plausibility of the model. We stress that our results remain agnostic to the underlying and currently unknown biological processes involved in root twisting.

In mechanical equilibrium, external forces and torques are related to $\vec{F}(s)$ and $\vec{M}(s)$ through

$$\frac{d\vec{F}(s)}{ds} + \vec{K}(s) = 0, \tag{2.14}$$

$$\frac{d\vec{M}(s)}{ds} + \vec{t}(s) \times \vec{F}(s) = 0, \tag{2.15}$$

where $\vec{K}(s)$ is the externally applied force per unit length. To understand the second equation, we note that if a force $\vec{F}(s)$ that is not aligned with $\hat{t}$ is applied to the rod, then a infinitesimal torque $d\vec{r}(s) \times \vec{F}(s)$ will be produced. This must be balanced by the internal moment $d\vec{M}(s)$, so that summing these two terms and dividing by ds yields Eq.(S2.15).

In the present case, we will consider the unstressed rod to be straight and

aligned with the z axis such that its end points are located at $z = 0$ and $z = Z$. Furthermore, we will make use of the small deflection approximation. Mathematically this means $s \to z$ in all formulas, but physically speaking, this means all the deformations of the rod are small. Differentiating Eq.(S2.13) twice and making use of Eq.(S2.15), we find

$$EI\frac{d\hat{t}}{dz} \times \frac{d^2\hat{t}}{dz^2} + EI\hat{t} \times \frac{d^3\hat{t}}{dz^3} + \frac{d^2}{dz^2}\left(M_z\hat{t}\right) = \frac{d}{dz}\left(\vec{F} \times \hat{t}\right). \tag{2.16}$$

For small deflections, the first term on the left is negligible and can be set to 0. Expanding the right hand side of Eq.(S2.16) and substituting Eq.(S2.14) gives

$$EI\hat{t} \times \frac{d^3\hat{t}}{dz^3} + \frac{d^2}{dz^2}\left(M_z\hat{t}\right) = \vec{F} \times \hat{t}' - \vec{K} \times \hat{t}. \tag{2.17}$$

In our situation, the external force $\vec{K}(s)$ arises from deformations of the gel, which we model as a linearly elastic medium. Consequently, when the root is displaced from its initially straight configuration, the gel exerts a restoring force

$$\vec{K}(z) = -\langle \alpha u_x(z), \alpha u_y(z), \alpha_z u_z \rangle, \tag{2.18}$$

where the first two components are the displacements perpendicular to the roots axis and u_z is the longitudinal component. The effective gel spring constants per unit length in the transverse and longitudinal directions are α and α_z respectively. Furthermore, the internal forces are given by $\vec{F}(z) = \langle F_x(z), F_y(z), T(z) \rangle$ where $T(z)$ is the longitudinal force throughout the rod. In the small deflection approximation however, terms proportional to F_x and F_y are of second order in smallness and can be neglected. This can be seen by noting $\hat{t} = \langle u_x', u_y', 1 \rangle$ and expanding Eq.(S2.17) to find the linearized equations of equilibrium:

$$\begin{aligned} EIu_y'''' - (M_z(z)u_x')'' - (T(z)u_y')' + \alpha u_x &= 0, \\ EIu_x'''' + (M_z(z)u_y')'' - (T(z)u_x')' + \alpha u_y &= 0, \end{aligned} \tag{2.19}$$

where we have used the prime notation to indicate $d(\ldots)/dz$. Eqs.(S2.19) involves only two constants, EI and α, in addition to four functions of the longitudinal coordinate z: $u_x(z)$, $u_y(z)$, $T(z)$, and $M_z(z)$.

2.7.7 Calculation of the effective gel spring constants

Given an infinite isotropic 3D elastic medium with a bulk modulus B much larger than the shear modulus G, what is the effective spring constant felt by a long 1D filament displaced in the directions parallel and perpendicular to its axis? To answer this question, we use the known elastic response of the medium in terms of displacement due to a point-like force at the origin given by Green's tensor [2]

$$g_{ij}(x,y,z) = \frac{1}{4\pi G}\left[\frac{\delta_{ij}}{r} - \frac{1}{4(1-\nu)}\frac{\partial^2 r}{\partial x_i \partial x_j}\right], \tag{2.20}$$

where δ_{ij} is a Kronecker delta-function, $r(x,y,z) = (x^2+y^2+z^2)^{(1/2)}$, and the Poisson ratio $\nu = 1/2$ in the limit $B \gg G$. That is, a force F_j in the direction j causes a displacement $u_i = g_{ij}(x,y,z)F_j$ in the i direction of the medium at $\langle x,y,z\rangle$. In cylindrical coordinates,

$$[g_{ij}] = \frac{1}{4\pi G r}\begin{bmatrix} 1-\gamma\frac{z^2}{r^2} & 0 & \gamma\frac{\rho z}{r^2} \\ 0 & 1-\gamma & 0 \\ \gamma\frac{z\rho}{r^2} & 0 & 1-\gamma\frac{\rho^2}{r^2} \end{bmatrix}, \tag{2.21}$$

where r is the distance away from the location of the point force and $\gamma = 1/4(1-\nu) = 1/2$ for an incompressible medium.

We now consider the case of a 1D rod in a 3D elastic medium. If $\vec{K}(z)$ is the force per unit length on the rod due to the medium, then $-\vec{K}(z)$ is the force on the medium due to the rod. Treating this as a sum of point-like forces and using

the fact that the gel is a linear medium, we can use the principle of superposition to write the net displacement at any position. For simplicity we imagine a force $\vec{K}$ uniform in z, corresponding to a response of the gel $\vec{u}$. Assuming the rod and medium are constrained to move together (i.e., a no-slip boundary), we can obtain a force-displacement relation and extract the effective gel spring constant per unit length. Using Eq.(S2.21), we calculate $u_i = \int g_{ij}(\rho, z - z')K_j(z')\, dz'$ and integrate for the transverse component

$$u_\rho = \int_{-L}^{L} g_{\rho\rho}(\rho, z - z')K_\rho\, dz' = \frac{K_\rho}{4\pi G} \ln\left(\frac{L}{a}\right), \tag{2.22}$$

where L is the wavelength or scale over which the deviation occurs, and a is a small-distance cut-off of order the rod radius (for roots $a \approx 0.25$ mm). Therefore, Eq.(S2.22) implies

$$\alpha \approx \frac{4\pi G}{\ln(L/a)} \tag{2.23}$$

in the limit $L/a \gg 1$. A similar calculation with the force parallel to the rod gives

$$\alpha_z \approx \frac{2\pi G}{\ln(L/a)}. \tag{2.24}$$

If we substitute $L \to Z \approx 10$ cm in these expressions, we have

$$\alpha \approx 2G, \quad \text{and} \quad \alpha_z \approx G. \tag{2.25}$$

It should be noted that these expressions for the effective gel spring constants are approximate for at least three reasons. First, the theory is greatly simplified by neglecting any possible plastic deformations of the gel caused by root growth. Second, the effective scale L of the logarithm in Eqs.(S2.23) and (S2.24) is actually a function of the root morphology and changes in time as the root deforms. Indeed, it may be more appropriate to have $L \approx \ell \approx 1$ cm for the transverse displacements associated with α. Third, the denominator of

Eqs.(S2.23) and (S2.24) can contain a constant of order unity added to the logarithm which arises from the different ways one can define the ratio L/a. This factor may be significant for the relevant experimental values. Therefore, we estimate an overall uncertainty in the gel spring constants of order $\sim 50\%$.

2.7.8 The compressive force $T(z)$ and its role in buckling

We next work out the expected functional form for $T(z)$ (Eq.(3) in main text). A theoretical approach is necessary because the 3D-TIGR data does not provide sufficient information to reliably reconstruct the longitudinal force profile $T(z)$; it would require measurements of the root's z displacements. We will also show why the root's buckling instability is localized near the tip (Figures 1 and 2 in main text and [3, 4]).

Consider what happens when the root elongates while its tip is stuck at the lower gel interface in our root growth experiments. A portion D of that extra length goes into displacing the interface, which exerts an effective spring force on the tip (the formula for T_D is given in the main text in the section called *Independent checks of fitted parameters*). The force due to the lower gel determines the longitudinal force at the tip, $T(0)$. Until the buckling instability is reached, the rest of the elongation can only go into a constant uniform longitudinal shift u_z of the root, which we model here as an inextensible rod. The longitudinal restoring force K_z due to the gel, pushes in the opposite direction, so that $T(z)$ decreases with z. It is given by Eq.(S2.18) as $K_z(z) = -\alpha_z u_z$ which is constant along the length. Substituting the force into Eq.(S2.14), we find

$$\frac{dT}{dz} = \alpha_z u_z. \tag{2.26}$$

Upon integration, we obtain

$$\begin{aligned} T(z) &= -\alpha_z Z u_z (1 - z/Z) + T_{\text{top}}, \\ &= -T_0 (1 - z/Z) + T_{\text{top}}. \end{aligned} \tag{2.27}$$

where $T_0 = \alpha_z Z u_z$, and $T(z = Z) = T_{\text{top}}$ is the boundary condition at the top of the gel where an effective spring constant relates u_z to T_{top}. Given the effective spring constants at either end of the root and the spring constant due to longitudinal gel displacements $k_L = \alpha_z Z$, it is possible to solve for how the elongation $D + u_z$ and the tip force $T(0) = T_0 + T_{\text{top}}$ gets partitioned. Note that although the uniform displacement u_z implies a deformation of the upper gel surface by that amount, any such deformations were so small as to be invisible. We infer that T_{top} is small, either because the root is long enough that $\alpha_z Z$ dominates the effective spring constant at the upper end, or because the approximation of an inextensible straight rod is inexact. Therefore, for simplicity, we adopt the assumption that $T_{\text{top}} = 0$, which gives the functional form used in the main text.

The above picture is valid only until T_0 reaches the buckling threshold: what happens then? We can make contact with prior theory [2, 3, 4], that assumed a uniform $T(z)$ and found a buckling threshold when $T(z) = \text{constant} \propto F_0$, the instability being a sinusoidal buckling at a wavelength proportional to ℓ; here F_0 and ℓ are the force and length scales constructed from EI and G in the scaling arguments. In our problem, crudely speaking, buckling occurs only once $T(z) > F_0$ along a length of order ℓ. Thus the actual threshold is strictly greater than F_0 by an amount proportional to dT/dz, and the initial buckling is confined to a half-arc of oscillations over a length $\sim \ell$. This is the same key observation made qualitatively in the main text, in connection with the shape of deformations of the wire embedded in gelatin.

After buckling, the added arc length due to transverse deviations takes up the largest portion of the elongation. Quantitatively, this can be seen by comparing the effective spring constant for longitudinal displacements of the root tissue k_L to the effective spring constant for transverse deflection $k_T \approx F_c/\ell \sim [(EI)G^3]^{1/4}$. Upon simplification, we find that $k_T/k_L \sim \ell/Z \ll 1$. Thus, new growth is primarily added to the buckled region because the unbuckled tissue above the helical region is held by a stiff spring force due to the root-gel coupling. Indeed, this is consistent with the more approximate clamped boundary condition used in the main text for our numerical simulations. Furthermore, in the post-buckling regime u_z is a nonuniform function of z. However, as long as the small deflection approximation is valid, the uniform part of u_z still dominates, so we assume Eq.(S2.27) may still be used for $T(z)$ in the buckled state.

In the main text, we estimate the value of T_0 by modeling its effect on the gel as that of a point-contact on a half-infinite medium. Two additional estimates can also be made. The first estimate is an alternative model using a Hertz contact. For a rigid sphere with radius ρ exerting a force T_0 on a half-infinite elastic medium,

$$T_0 = \frac{8}{3}\frac{G}{1-\nu}D^{3/2}\rho^{1/2}, \tag{2.28}$$

where G is the gel shear modulus, ν is the gel's Poisson ratio, and D is the depth of the dimple. Substitution of numerical values show that this estimate gives similar results for T_0 as those reported in the text. The second estimate places an upper bound on T_0 by considering the force required to penetrate into the lower gel layer. Assuming the gel fractures when the strain $D/\rho \sim 1$, we find $T_0 \leq 4\pi(G + G_B)D^2$, which yields a range of 36 to 77 mN for $G = 100$ to 1500 Pa, consistent with the upper dashed line in Figure 6(D) of the main text. Further variation for fixed values of G can arise from the sharpness of the root tip, the

angle of attack, and diameter of the root.

2.7.9 Determination of the moment M_z

To discern the functional form of $M_z(z)$, we integrated Eqs.(S2.14), (S2.15), and (S2.18):

$$\begin{aligned} F_x(z) &= -\alpha \int_z^Z u_x(\hat{z})\, d\hat{z}, \\ F_y(z) &= -\alpha \int_z^Z u_y(\hat{z})\, d\hat{z}, \\ M_z(z) &= \int_z^Z \left[\vec{F}(\hat{z}) \times \vec{t}(\hat{z})\right]_z d\hat{z} \end{aligned} \tag{2.29}$$

where the notation $[\cdots]_z$ means taking the z projection, and experimental data was supplied for the coordinates $u_x(\hat{z})$ and $u_y(\hat{z})$. Performing this calculation over 20 roots, we found a significant amount of variation from root to root as shown in Figure S2.8. Nevertheless, some general features were common. In particular, above and below the helical region M_z went to zero, while in the helical region M_z tended to fluctuate. We numerically experimented with two expressions for the moment, $M_z = M_0 \sin(\pi z/Z)$ and $M_z = \text{constant}$. The former is more correct in light of our understanding of the boundary conditions and Figure S2.8, however, we chose to use the simpler latter expression since both produced similar results for the model fitting and the simulation discussed in the main text.

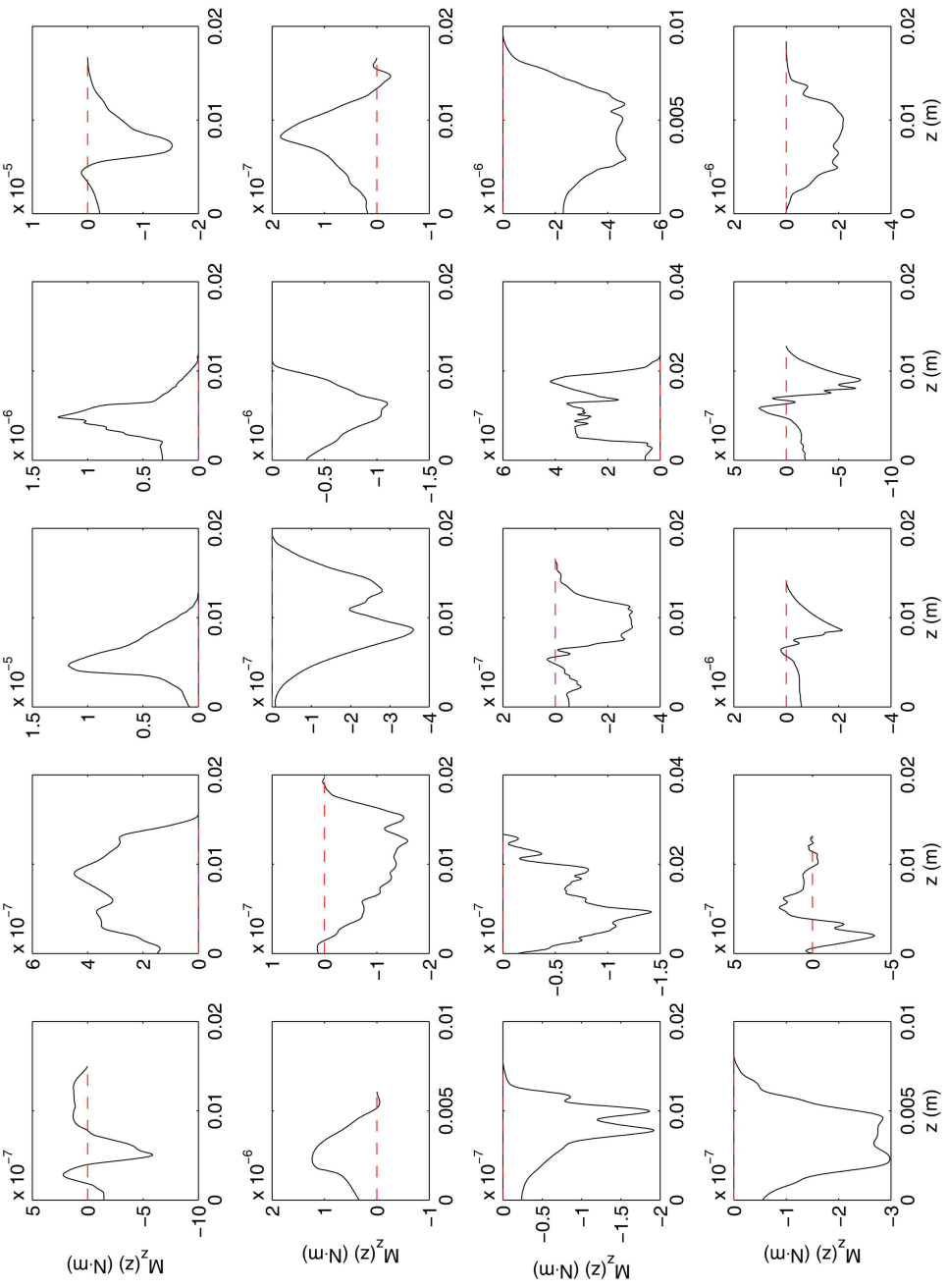

Figure 2.8: To determine the functional form of the axial moment, we used Eqs.(S2.29) to explicitly calculate $M_z(z)$ for 20 roots. The results of this procedure shown here illustrate the plant-to-plant variation. In each case, the root tip is located at $z = 0$ and the range of z corresponds to a region slightly larger than the helical deformation. The red dashed lines correspond to $M_z = 0$ to help guide the eye.

2.7.10 An alternate mechanism for buckling localization

As pointed out in the main text, Eqs.(2) assume a uniform bending modulus EI. However, this assumption may be questionable for real roots. Developmental gradients and tapering of the root diameter can affect both E and I making them functions of position. Thus, one could imagine an alternate mechanism for the localization of buckling: A local decrease of the root's modulus near the tip makes it more susceptible to compressive forces and therefore more prone to buckling. Whereas in the main text we assumed EI was constant and allowed $T(z)$ to vary, this proposed mechanism reverses the roles so that $EI(z)$ varies and $T(z) = T_0$ is constant. We now ask whether experiments can distinguish between these two scenarios.

To see how we can rule out variations in EI as the sole source of localized buckling, we recall that at the root tip, an axial force induces a dimple in the lower gel layer. When the axial force is constant throughout the root, there will be an analogous "pimple" in the top gel surface, and moreover, it will be larger than the dimple because (1) the top gel modulus is less than the lower gel modulus and (2) instead of a gel/gel interface, we have a gel/air interface. The height of this pimple can be estimated using the same formula used in the main text to relate the force exerted by the root tip to the dimensions of the dimple. Thus, we have $D = T_0/4\pi G\rho$. Taking $G = 1$ kPa, $T_0 = 40$ mN, and $\rho = 1.0$ mm, we find a pimple height of 3.2 mm. As previously mentioned, there was no observable pimple at the top gel surface. We therefore conclude that $T(z = Z) \approx 0$, which is inconsistent with $T(z = 0) = T_0$. Therefore variations in EI can not solely be the source of localization.

A more realistic model for the localization of buckling includes variations

in both the bending modulus and the longitudinal force. The question then becomes which is the dominant effect. To determine this experimentally, we manually compressed in air several roots grown in unlayered gels. Because the axial load was constant throughout, any localization of buckling or longitudinal asymmetry would be due to a spatially varying bending modulus. In all cases, we found nearly symmetric non-localized shapes. This suggests variations in $EI(z)$ are not playing a significant role in buckling localization.

To explore the consequences of a model combining $T(z)$ and $EI(z)$, we first need an expression for spatial variations of the bending modulus. One option is to use the experimentally observed variations in root radius (Figure 6(C) in main text). From the figure, we see the ratio of the root radius in the helical region to the radius near the base is greater than $2/3$ in more than half of the roots. To produce a linear tapering where the root radius ratio is exactly $2/3$, we use the expression $\rho(z) = \rho_0(1 + z/2Z)$, where ρ_0 is the effective radius of the tip, and $z = Z$ is the base of the plant. This model yields a position-dependent bending modulus $EI(z) = EI(1 + z/2Z)^4$. Though crude, it captures the essential point: $EI(z)$ can be substantially smaller near the tip than near the base as illustrated by the z^4 dependence.

Because the bending modulus varies with position, the natural force scale for buckling $F_c(z) = \sqrt{EI(z)G}$ will too. Therefore, the non-dimensional longitudinal force $T(z)/F_0(z)$ gives a local estimate of how much force above the buckling threshold each portion of the rod experiences. To determine the relative contributions to buckling localization, we compare $T_0/F_0(z)$ to $T(z)/F_0(z)$, and $T(z)/F_0$ to $T(z)/F_0(z)$. In the first case,

$$\frac{T_0}{F_0(z)} \Big/ \frac{T(z)}{F_0(z)} = \frac{T_0}{T(z)} = \frac{1}{1 - z/Z}, \tag{2.30}$$

while in the latter,

$$\frac{T(z)}{F_0}\Big/\frac{T(z)}{F_0(z)} = \frac{F_0(z)}{F_0} = (1 + z/2Z)^2. \tag{2.31}$$

In the helical region where $z/Z \ll 1$, we find that both Eq.(2.30) and (2.31) are approximated by $1 + z/Z$. Thus, for the functional forms used here, the spatially varying longitudinal force and bending modulus both contribute equally to buckling localization. However, we can explain our experimental observations with only spatial variations in $T(z)$. The converse is not true; as described above, a theory with only spatial variations in $EI(z)$ is inconsistent with our experimental observations. Thus, our mathematical model for helical root buckling adopts the minimum number of elements.

2.7.11 Model fitting and boundary conditions

When we fit the model equations to the experimental data and extracted out the values for the parameters EI, T_0 and M_0, a potentially dangerous assumption was made: the coordinate system aligned with the undeformed root is the "correct" coordinate system. Put another way, our model equations depend on the absolute displacement of the rod from the reference axis $\langle 0, 0, z\rangle$ to generate the gel restoring forces acting on the buckled root. If our assumed coordinate system is tilted by some small angle at $z = 0$, this could potentially lead to large spurious displacement forces at the far end where $z = Z$. In turn, this would be expected to produce erroneous results for the distribution of fitted parameters EI, T_0, M_z discussed in the main text as well as the measured values of $\langle L\rangle$ and $\langle R^2\rangle$.

On one hand, this objection can be refuted by the experimental movie data

where the small deflection approximation held (SM2 and SM3). In these cases, the direction of the undeformed root tissue and the centerline of the helical deformation reasonably coincide. On the other hand, we still wanted to address the concern more directly. Thus, we reanalyzed the data with deliberately tilted coordinate systems and explored the effects on EI, T_0 and M_0. We found the values of these parameters were affected by at most a factor of 2 for angular deviations of $\pm 12^\circ$. This is a relatively small difference relative to the spread over the ensemble of roots, and ought not produce significant effects in our analysis.

2.7.12 Variation with torsion

From the results of model testing, we found a range of best-fit values for the inferred twist per unit length $3M_0/2EI$ clustered around 0.1 to 1.0 radians/mm. Holding the bending modulus EI and tip tension T_0 fixed while systematically varying the twist produced the plots for $\langle L \rangle$ and $\langle R^2 \rangle$ shown in Figure S2.9. We found the range of 0.1 to 0.7 radians/mm caused negligible variation in the predicted shape of the helically buckled rod configuration. Moreover, at higher values in the range of 1.0 to 2.0 radians/mm, the solutions failed to resemble experimental data. Evidently, the torsion alone is unable to account for the variations in $\langle L \rangle$ and $\langle R^2 \rangle$.

2.7.13 Movie Legends

- SI Movie 1 shows the growth of a primary *Medicago* root in a compliant ($G \sim 250$ Pa) gel. Because the root exhibits such large deflections, it's morphology is not captured by the mathematical model. Variations in the

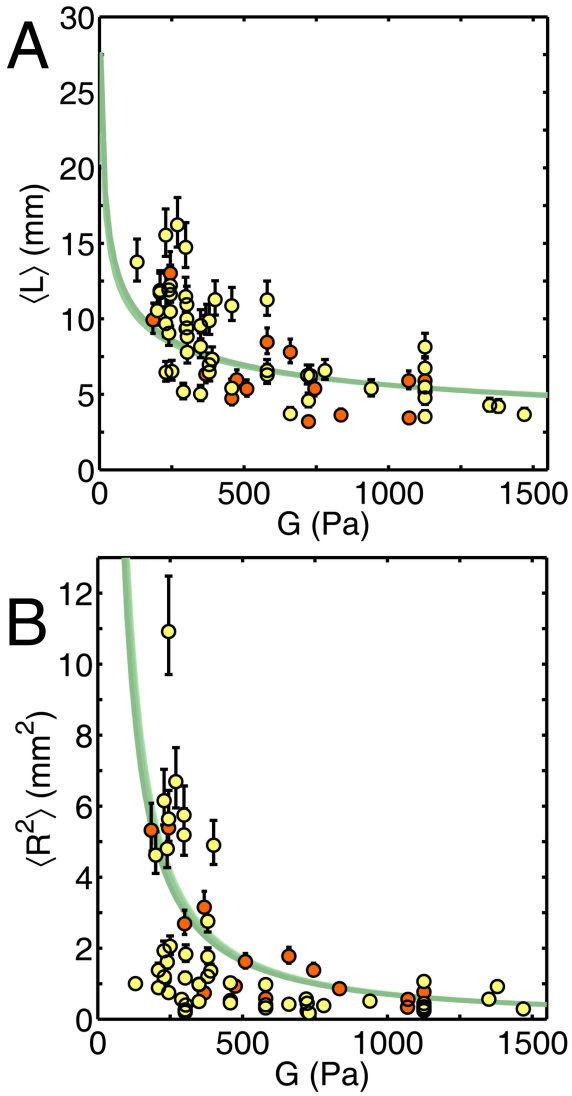

Figure 2.9: Experimental measurements for the (A) longitudinal and (B) transverse length scales of the helical root morphology are plotted against the top gel layer modulus G. When comparing our data to a theoretical model, we found that certain roots were in violation of the assumed small deflection approximation; these data are colored red. The contours were produced by numerical integration of our model equations for fixed EI, T_0, and variable $3M_0/2EI$. The contours shown here are for values in the range of 0.1 to 0.7 radians/mm. Values higher than this produced solutions to the buckled rod equations which did not accurately resemble the experiments.

apparent root radius are in part due to light scattering, movement in-and-out of the imaging plane, and image processing filters used during the 3D reconstruction.

- SI Movie 2 shows the growth of a primary *Medicago* root in a stiff ($G \sim 1250$ Pa) gel. This root obeys the small deflection approximation used in our model and is therefore captured by Eqs.(2-4) in the main text. Variations in the apparent root radius are in part due to light scattering, movement in-and-out of the imaging plane, and image processing filters used during the 3D reconstruction.
- SI Movie 3 shows multiple viewing angles of a primary *Medicago* root in a gel of intermediate stiffness ($G \sim 1000$ Pa). This root obeys the small deflection approximation used in our model and is therefore captured by Eqs.(2-4) in the main text. Variations in the apparent root radius are in part due to light scattering, movement in-and-out of the imaging plane, and image processing filters used during the 3D reconstruction.

REFERENCES

[1] Jinyuan Liu, Laura A Blaylock, Gabriella Endre, Jennifer Cho, Christopher D Town, Kathryn A VandenBosch, and Maria J Harrison. Transcript profiling coupled with spatial expression analyses reveals genes involved in distinct developmental stages of an arbuscular mycorrhizal symbiosis. *The plant cell online*, 15(9):2106–2123, 2003.

[2] L. D. Landau and E. M. Lifshitz. *Itheory of elasticity*. Pergamon, New York, 3rd edition, 1986.

[3] Clifford P Brangwynne, Frederick C MacKintosh, Sanjay Kumar, Nicholas A Geisse, Jennifer Talbot, L Mahadevan, Kevin K Parker, Donald E Ingber, and David A Weitz. Microtubules can bear enhanced compressive loads in living cells because of lateral reinforcement. *The journal of cell biology*, 173(5):733–741, 2006.

[4] Moumita Das, Alex J Levine, and FC MacKintosh. Buckling and force propagation along intracellular microtubules. *Epl (europhysics letters)*, 84(1):18003, 2008.

CHAPTER 3

ANATOMIC VARIATION OF DEPTH-DEPENDENT MECHANICAL PROPERTIES IN NEONATAL BOVINE ARTICULAR CARTILAGE

Jesse L. Silverberg, Sam Dillavou, Lawrence Bonassar, and Itai Cohen, *J. Ortho. Res.* **31**, 686-691 (2013).

3.1 Abstract

Articular cartilage has well known depth-dependent structure and has recently been shown to have similarly non-uniform depth-dependent mechanical properties. Here, we study anatomic variation of the depth-dependent shear modulus and energy dissipation rate in neonatal bovine knees. The regions we specifically focus on are the patellofemoral groove, trochlea, femoral condyle, and tibial plateau. In every sample, we find a highly compliant region within the first 500 μm of tissue measured from the articular surface, where the local shear modulus is reduced by up to two orders of magnitude. Comparing measurements taken from different anatomic sites, we find statistically significant differences localized within the first 50 μm. Histological images reveal these anatomic variations are associated with differences in collagen density and fiber organization.

3.2 Introduction

Knowledge of normal synovial joint functioning, disease progression, and therapeutic treatments are strengthened by our understanding of articular cartilage (AC) mechanical properties. Because tissue engineered constructs do not yet

fully mimic the biomechanical properties of native samples, the study of cartilage mechanics must stem from site-specific and cross-species studies performed with animal and human samples. Indeed, previous work has shown that within a single joint, anatomic variations exist in material properties such as compressive/aggregate modulus, permeability, Poisons ratio, and tissue thickness[1, 2, 3, 4, 5, 6]. While many anatomic variation studies have employed compressive testing[1, 2, 3, 4], comparatively fewer have reported on shear properties[5, 6], resulting in a particularly acute knowledge gap, since shear loading is common during normal physiological conditions.

Studies quantifying AC shear properties generally report the equilibrium[7, 8, 9, 10, 11] or complex[12, 13, 14, 15, 16, 17, 18] shear modulus averaged over the tissue thickness. However, the collagen and proteoglycan networks underlying AC have well known depth-dependent heterogeneity[19]. Recent advances in rheometry techniques have made it possible to measure the depth-dependent shear modulus[10, 11, 16, 17, 18], revealing localized variations analogous to those reported in the compressive properties of cartilage[19, 20, 21, 22, 23]. Notably, it was discovered that the superficial zone of neonatal bovine and adult human AC is 5 to 50 times more compliant under shear than the mechanically homogeneous mid and deep zones. These spatially localized variations in the mechanical properties are masked by bulk measurements, and their recent observation raises fundamental questions, such as how the depth-dependent shear properties, which parallel the depth-dependent structure of AC, vary with anatomic location.

The aim of this study was to measure and compare the depth-dependent shear modulus and energy dissipation rate of neonatal bovine AC harvested

from the patellofemoral groove (PFG), trochlea (TRO), femoral condyles (FC), and tibial plateau (TP) (Figure 3.1). The PFG and TRO experience low in vivo loading, while the FC and TP experience high in vivo loading. Previous work suggests that tissue mechanical properties vary with loading conditions[1, 2, 3, 4, 5, 6] and led us to hypothesize the existence of measureable differences in the shear properties. Moreover, the data gathered from all four regions provide useful biomechanical targets for tissue engineered constructs designed to mimic the properties of native tissue. Indeed, these results contribute to our still growing understanding in the depth-dependent shear properties in articular cartilage.

3.3 Methods

3.3.1 Split-line test

We used split-line testing of the PFG, TRO, FC, and TP in 1-3 day old calf knees (Gold Medal Packing, NY) to identify suitable sites for mechanical testing[24]. Tissue from each region was rinsed with Delbecco's modified phosphate buffered saline (PBS, Life Technologies) before Higgins India Ink (Chartpak Inc., MA) was applied to the articular surface. A rectangular grid pattern of sites was selected and a cylindrical needle 10 mm long and 1 mm wide was then inserted into the cartilage. Excess ink was washed off with PBS leaving behind a pattern of split-lines that were either oriented or symmetric. Denoting the direction normal to the articular surface as the transverse axis, oriented splits were used to identify zones of transverse anisotropy, while symmetric splits identified zones of transverse isotropy. This test was repeated for two entire bovine

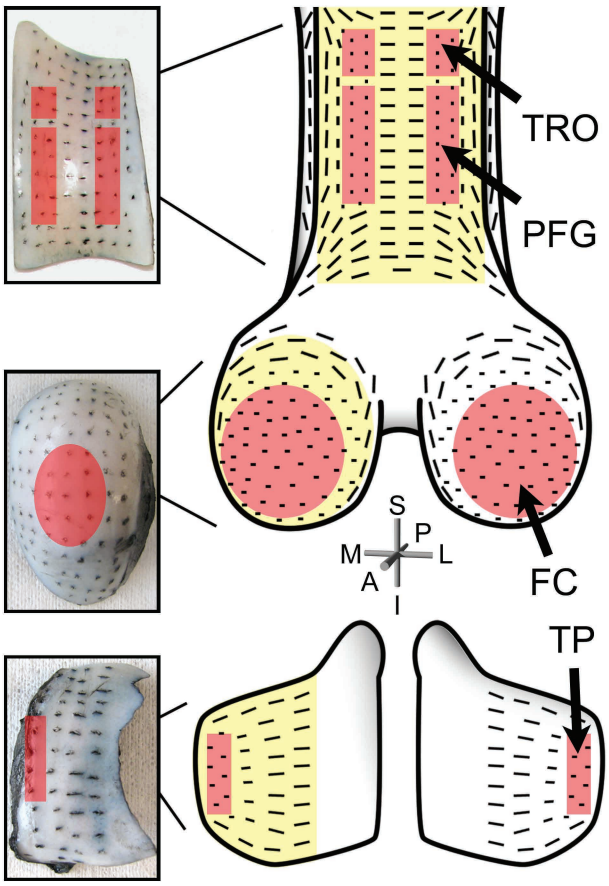

Figure 3.1: Split-line testing reveals the collagen fiber organization at the articular surface of neonatal bovine knee AC. Digital photographs (left) were taken and used to construct a schematic overview (right). Dots and lines indicate whether the tissue was isotropic or anisotropic, respectively. The zones highlighted in yellow correspond to the photographs and the zones in red are the sites where tissue for mechanical testing was harvested from.

knee joints and digital photographs were taken (Figure 3.1). In zones of transverse isotropy, collagen fibers at the articular surface are randomly oriented in the articulating plane, yielding a material symmetry that causes the in-plane mechanical properties to be directionally independent[25]. Samples for shear testing were harvested from these zones to (1) preclude in-plane fiber orientation from introducing an uncontrolled source of sample-to-sample variation, and (2) allow shear in any applied direction to deform AC tissue in a manner similar to shear applied in the direction of normal physiological loading.

3.3.2 Materials

Cylindrical explants 3.5 mm thick and 6 mm in diameter were harvested with scalpel blades and biopsy punches from nine calf knees without the underlying bone tissue. They were then cut longitudinally into semi-cylinders and placed in a solution of PBS and 7 μg/mL 5-dichlorotriazinylaminofluorescein (5-DTAF, Life Technologies), an all-protein stain, for 3 hours. Afterwards, each sample was soaked in PBS for 1 hour to rinse excess dye. A total of 13 samples from each anatomic region studied were mechanically tested within 24 hours of harvesting.

3.3.3 Confocal strain mapping

Fluorescently dyed semi-cylindrical cartilage samples were mounted in a Tissue Deformation Imaging Stage (TDIS, Harrick Scientific, NY) so the long axis was perpendicular to the gripping surfaces[18], allowing uniform shear forces to be

applied on the articular surface (Figure 3.2). To prevent slippage, samples were glued to a plate attached to a load cell, while friction between a platen plate and the articular surface was used to brace the opposing side where shear was applied. Friction was generated on the unglued surface by compressing samples by 8.0 ± 0.5% their initial thickness, and given 1 hour to reach mechanical equilibrium. Once mounted, samples were immersed in PBS and the TDIS was positioned on an inverted Zeiss LSM 510 confocal microscope (Carl Zeiss, Germany) to image tissue deformations on the rectangular face of the semi-cylinder. Automated tracking of the local shear strain was facilitated by a photobleached line along the z axis. We define z to be the longitudinal direction, such that $z = 0$ is the articular surface and it measures depth into the tissue. Sinusoidal shear was applied at the physiologically relevant rate of 1.0 Hz (approximately walking speed) with a peak amplitude of 1% the compressed tissue thickness, consistent with the small strain approximation used in linear elasticity. Movies of tissue deformation recorded at 20 frames per second with a 10x objective were saved for later analysis.

Using Grid Resolution Automated Tissue Elastography[17] to analyze video data of the dynamic deformations, we calculated the complex shear modulus $G^*(z) = |G^*(z)| \exp(i\delta_\tau(z))$ as a function of depth z (Figure 3.3 (A-D)). From our video data, we were also able to calculate the depth-dependent energy dissipation rate per unit volume[18]. For each sample, the total energy dissipated as a function of z was normalized by the total energy dissipated per unit cycle (Figure 3.3 (E-H)). Comparisons of the modulus and energy dissipation among the four regions were performed along with tests for statistical significance (Figure 3.4 (A-D)).

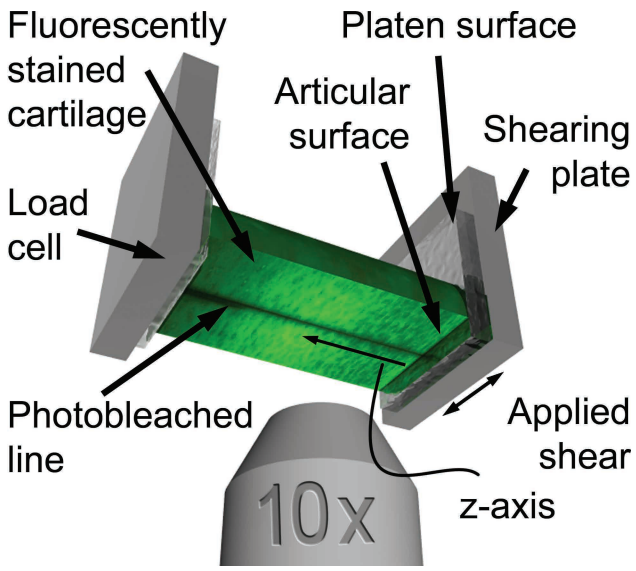

Figure 3.2: This schematic illustrates the basic geometry and operation of confocal strain mapping (see main text). Briefly, a line is photobleached onto the tissue to act as a fiducial marker and facilitate automated tracking of shear strain as a function of depth from the articular surface. Shear is applied by one plate, while load is simultaneously measured at the opposing side and deformations of the photobleached line are imaged with a fast confocal microscope.

3.3.4 Brightfield and polarized light histology

To image collagen content and organization, we fixed six samples from each anatomic region in 10% PBS-buffered formalin. Paraffinized sections 4 μm thick were dewaxed with xylene, rehydrated to water in decreasing concentration ethyl alcohol baths, and stained with Picrosirius red[26]. With a 40x objective, white and monochromatic light was used to observe collagen content, and white polarized light aligned parallel to the articuluar surface was used to determine fiber organization (Figure 3.5 (A-D)). All samples were stained simultaneously and viewed under identical lighting conditions. A semi-quantitative analysis was performed on monochromatic and polarized light histological im-

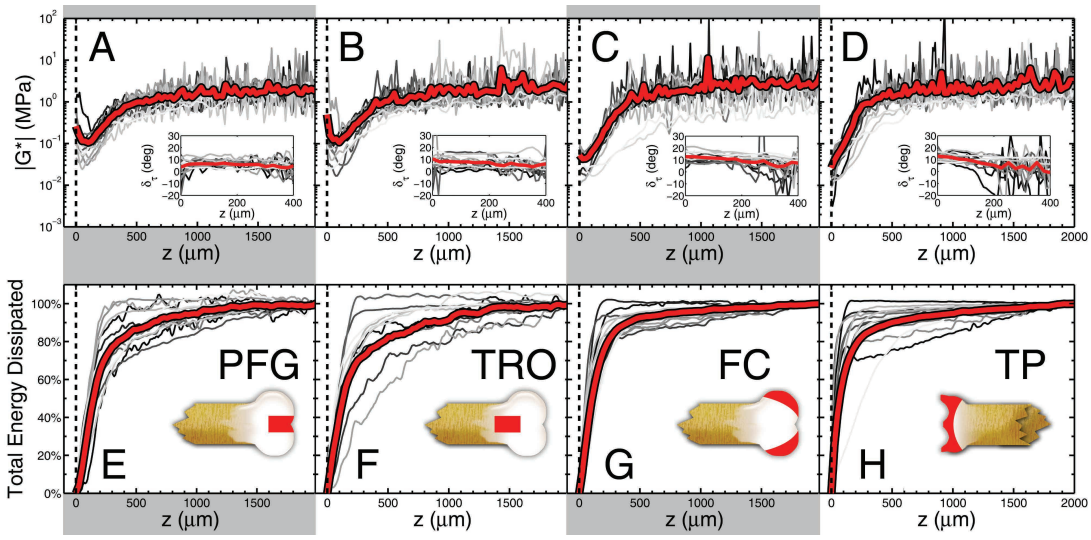

Figure 3.3: Measurements of the depth-dependent shear modulus $|G^*(z)|$ for the (A) PFG, (B) TRO, (C) FC, and (D) TP are plotted on a logarithmic axis as a function of depth. The articular surface is at $z = 0$, gray lines are individual measurements ($n = 13$ samples for each anatomic region), and the red lines are averages. We find the first 500 m of tissue is 10 to 100 times more compliant than the remainder of the tissue. Insets show the phase angle of the complex shear modulus. Measurements of the cumulative energy dissipated as a function of depth for the (E) PFG, (F) TRO, (G) FC, and (H) TP show that the tissue near the articular surface is primarily responsible for viscous losses. Insets schematically illustrate the region from which tissue was harvested.

ages ($n = 6$ for each region) to facilitate comparisons of the depth-dependent pixel intensity between anatomic regions (Figure 3.5 (A-D)). For every sample, the tissue edge exhibited a slight roughness so that the articular surface had small fluctuations in position. To compensate, we used gradient edge detection techniques in MATLAB v7 (The Mathworks Inc., MA) to identify the articular surface allowing us to uniquely define $z = 0$ for each column of pixels (see SI). We then averaged columns of pixel intensity data within each image such that their z position was properly registered, and normalized by the maximum possible pixel intensity value.

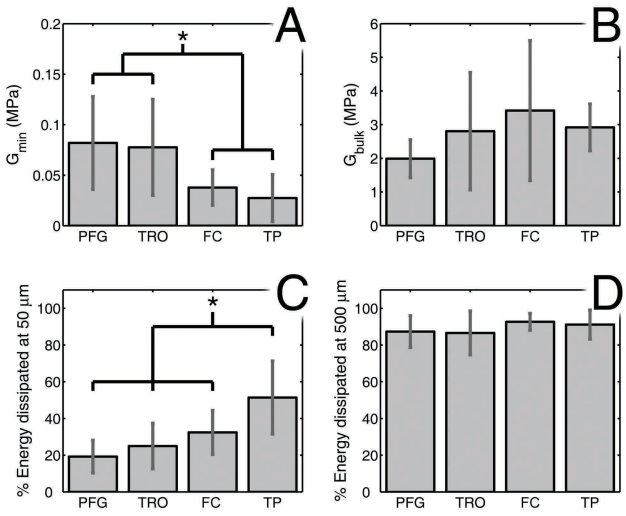

Figure 3.4: From our depth-dependent measurements, we compared (A) G_{min}, the minimum value of $|G^*(z)|$, (B) G_{bulk}, the average value of $|G^*(z)|$ for $z > 1000$ μm, (C) the percent of energy dissipated within the first 50 μm of the articular surface, and (D) the percent of energy dissipated within the first 500 μm from the articular surface. In each case, averages and standard deviations are shown for the four anatomic regions studied ($n = 13$ for each anatomic region). Here, $^* = p < 0.05$, as determined from a balanced 1-way ANOVA.

3.3.5 Statistics

Data was analyzed with a balanced 1-way ANOVA on each group and a post-hoc t-test using Tukey's honestly significant difference criterion to determine statistical significance ($p < 0.05$). All statistical analyses were carried out in MATLAB and expressed as a mean ± SD.

3.4 Results

Split-line testing in all four regions revealed transversely isotropic and anisotropic zones (Figure 3.1). To ensure simple, consistent loading conditions,

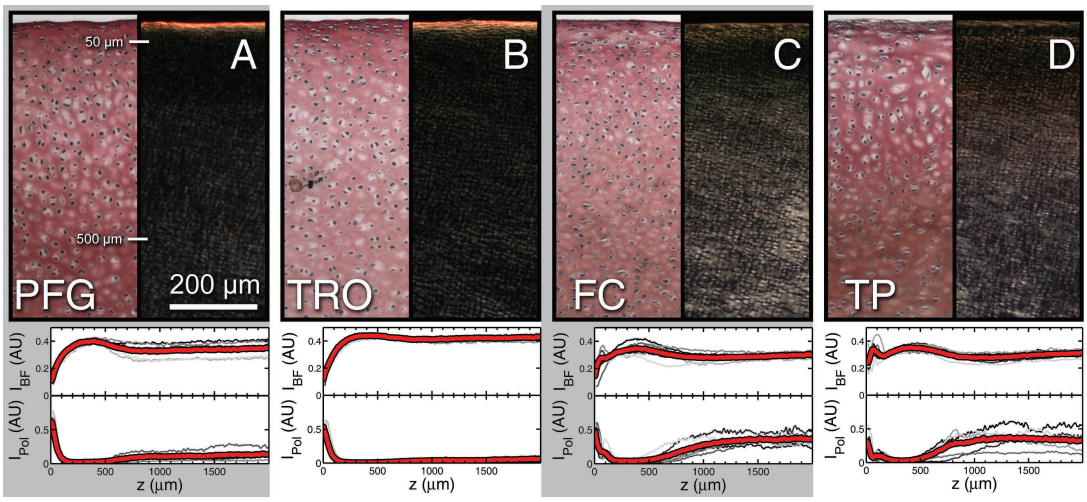

Figure 3.5: From our depth-dependent measurements, we compared (A) G_{min}, the minimum value of $|G^*(z)|$, (B) G_{bulk}, the average value of $|G^*(z)|$ for $z > 1000$ μm, (C) the percent of energy dissipated within the first 50 μm of the articular surface, and (D) the percent of energy dissipated within the first 500 μm from the articular surface. In each case, averages and standard deviations are shown for the four anatomic regions studied ($n = 13$ for each anatomic region). Here, $^* = p < 0.05$, as determined from a balanced 1-way ANOVA.

we used tissue from transversely isotropic zones with the flattest possible articular surface. For the PFG and TRO, samples were harvested from a narrow region where the articular surface was nearly flat. For the FC, we found the tissue surface was rounded with a $2 \sim 3$ cm radius of curvature in the zone of transverse isotropy. Variations in surface height were $< 5\%$, and tissue harvested from this zone was chosen to minimize sample curvature. The TP has narrow zones of transverse isotropy in the most medial and lateral portions; though small in extent, at least two samples were reliably obtainable. These sites are covered by the meniscus in vivo, which we note is more compliant under compression than AC. Having identified transversely isotropic tissue from each anatomical region, we were able to harvest and mechanically test samples without tracking their in-plane orientation.

Our data shows $|G^*(z)|$ varies with depth and location within the joint (Figure 3.3 (A-D)). Specifically, the average depth-dependent shear modulus for the FC is more compliant in the superficial zone than the PFG and TRO. Furthermore, the TP is the most compliant region tested, and within the measurement resolution, fails to exhibit the characteristic upswing in $|G^*(z)|$ near $z = 0$ seen in the other tested regions. For each sample, we extracted the minimum value of $|G^*(z)|$, hereafter referred to as G_{min}, and found that the FC and TP are more compliant than the PFG and TRO (Figure 3.4 (A)). We also calculated G_{bulk}, the average value of $|G^*(z)|$ for $z > 1000$ μm, for each sample and found the four regions statistically indistinguishable (Figure 3.4 (B)).

Measurements of the complex phase angle δ_τ revealed little depth-dependent variation in the PFG and TRO (Figure 3.3 (A,B)), while the FC and TP exhibited a slight but noticeable decline with increasing z (Figure 3.3 (C,D)). Averaged over the first 400 μm of tissue, δ_τ was $5 \pm 1^\circ$ for the PFG, $7 \pm 2^\circ$ for the TRO, $9 \pm 3^\circ$ for the FC, and $7 \pm 4^\circ$ for the TP. For $z > 400$ μm, the phase angle for all four regions was noisy, but tended to remain constant.

All four regions dissipate energy primarily near the articular surface, however, there is notable sample-to-sample variation: The least localized TP or FC can have a similar energy dissipation profile as the most localized PFG or TRO (Figure 3.3 (E-H)). To make quantitative comparisons, we measured the percent of energy dissipated within the first 50 and 500 μm of each sample. We found the TP has the greatest localization of energy dissipation (Figure 3.4 (C)), and all four regions dissipate indistinguishable amounts of energy by 500 μm (Figure 3.4 (D)).

Picrosirius red staining reveals depth-dependent variations similar to our

rheological measurements. Brightfield and monochromatic images (Figure 3.5 (A-D)) show all four regions are more heavily stained where $z < 50$ μm relative to the tissue between 50 and 500 μm, indicating a highly localized collagen-dense band at the articular surface. Moreover, for $z > 500$ μm, we find minimal variation associated with depth. We also find that both the FC and TP exhibit localized bands of high collagen content near $z = 100$ μm not seen in the PFG or TRO.

Using polarized light, we see the PFG and TRO have a band of high birefringence where $z < 50$ μm and a 10-fold intensity reduction where $z > 50$ μm (Figure 3.5 (A,B)). The FC and TP have more subtly modulated depth-dependent properties (Figure 3.5 (C,D)), and in particular, we see a region of low birefringence where $50 < z < 500$ μm, and an overall increase everywhere else. Furthermore, the birefringence of the PFG, TRO, and FC is higher than the TP at the articular surface, whereas the PFG and TRO exhibit noticeably less birefringence than the FC and TP for $z > 500$ μm. As with brightfield imaging, we see negligible depth-dependent variations in all four anatomic sites for $z > 500$ μm.

3.5 Discussion

Studying the depth-dependent complex shear modulus and energy dissipation rate in neonatal bovine articular cartilage revealed spatially localized, statistically significant differences near the articular surface associated with anatomic location. While tissue near the articular surface was consistently the most compliant portion of each sample, anatomic sites experiencing high levels of in vivo loading (FC, TP) were significantly more compliant than sites with low levels of

in vivo loading (PFG, TRO). Furthermore, the TP dissipates more energy closer to the articular surface than the PFG, TRO, or FC. These differences in biomechanical properties associated with anatomical site are independent of regional cartilage thickness and coincide with depth-dependent heterogeneity in the AC collagen network. In the absence of theoretical models accounting for local collagen structure, the experimental data suggests a role for both collagen content and fiber orientation in setting the depth-dependent shear modulus and energy dissipation rate, but with no clear indication of their individual contributions. Similarly, no clear feature accounts for the lack of upswing in the TP shear modulus data near the articular surface, and it may arise from a convolution of collagen fiber orientation and density. While our results indicate potential targets for the development of complex, layered, and realistic engineered tissue constructs for therapeutic implantation[27, 28], additional studies are needed to precisely relate microscopic structural information to macroscopic material parameters.

We find broad agreement when comparing this work to previous studies of sheared bovine AC. For example, using 18 month old bovine PFG, measurements of the complex shear modulus averaged over the entire sample thickness reported $|G^*| = 0.75$ MPa and $\delta_\tau = 11^\circ$ when sheared at 1.0 Hz with a 9% axial compression[14]. Consistent with this earlier work, our depth-averaged measurement is $\langle |G^*(z)| \rangle_{\mathrm{PFG}} \approx 0.6$ MPa. Similarly, a pair of studies examining $2 \sim 8$ year old bovine TP with no axial compression reported the equilibrium shear modulus[8] $G_{\mathrm{eq}} = 0.38$ MPa, and the complex modulus[13] $|G^*| = 0.8$ MPa with a phase angle $\delta_\tau = 9.3^\circ$ when sheared at 100 Hz. Despite differences in age, shear rate, and loading conditions, these values are again comparable to our measurements. Finally, a study using the confocal strain mapping technique employed here sheared neonatal bovine PFG at 0.1 Hz and reported similar results for

$|G^*(z)|$[17].

While our results concern neonatal bovine tissue, quantitatively similar data have been reported in healthy adult human AC. Given differences in tissue age and thickness, this surprising result can be rationalized by noting that tissue maturity causes calcification and remodeling of the deep zone, and would not be expected to leave an age-dependent signature on the articular surface of healthy joints. For example, a pair of studies on human FC and TP tissue sheared under 0 and 15% axial compression[10, 16] found the shear modulus was significantly lower within the first 800 μm when compared to the rest of the tissue. Values for the shear modulus of FC samples were typically $G_{\text{eq}} = 0.2$ MPa near the articular surface and $1 \sim 3$ MPa in the deep zone. Likewise, the TP was $0.02 \sim 0.03$ MPa near the surface whereas the deep zone was also $1 \sim 3$ MPa. While these results quantitatively agree with our findings in bovine AC, they are unable to resolve spatial variations smaller than $100 \sim 250$ μm. In another study of adult human TP using the high resolution confocal strain mapping technique employed here[17], spatial variations in $|G^*(z)|$ were observed at length scales approaching $10 \sim 15$ μm. Specifically, highly localized variations near the articular surface similar to those observed in bovine PFG, TRO, and FC were reported. In order to determine whether this upswing in modulus at the articular surface is a general feature of human AC, a more detailed study controlling for split-line orientation, anatomic location, and tissue degradation due to age or disease would be necessary.

Because the depth-dependent shear properties of human tissue are quantitatively similar to bovine, the anatomic variations reported here may have relevance for tissue transfer procedures such as OATS® (Osteochondral

Allo/Autograft Transfer System). In these therapeutic surgeries, AC focal injuries are repaired by replacing damaged tissue with tissue harvested from a cadaveric source or an unloaded region of the joint[29, 30]. Because long-term success of these therapies depends on matching mechanical properties between donor and graft sites[31], the measurements presented here raise the possibility of a previously unrecognized depth-dependent matching criterion for tissue selection. Although an analogous study with human tissue should be performed first, the ability to quantitatively match depth-dependent shear properties of donor and recipient tissue may be relevant for long-term patient outcomes.

We note some of the limitations of this study. To obtain large numbers of pristine joints, we used young tissue, potentially obscuring effects that may be important in adult animals such as disease and age-dependent remodeling of the collagen network[32]. Indeed, our work leaves unanswered whether these phenomena are accompanied by changes in the depth-dependent mechanical properties. Additionally, the experimental protocol used here to measure the shear modulus takes advantage of the transverse isotropy identified in the split-line tests. For transversely anisotropic tissue, the protocol would have to be modified to track the primary split-line orientation throughout testing.

These results on the depth-dependent shear properties of bovine AC complement the existing literature on bulk shear properties. We identified a localized decrease in shear modulus occurring at the articular surface that distinguishes this tissue from the mid and deep zones. By studying distinct anatomic sites with different in vivo loading conditions, we found that all anatomic variation and nearly 90% of the energy dissipation is confined to the superficial zone. This new experimental data should stimulate further work examining the re-

lationship between microscopic structure and macroscopic function, as well as provide new insights on normal and diseased cartilage functioning.

3.6 Acknowledgments

JLS would like to thank D Griffin, K Novakofski, D Lachowsky, L Bradley, and M Buckley for their insights and assistance. JLS acknowledges support from the National Science Foundation through a Graduate Research Fellowship. This work was supported in part by the NSF through grant DMR-1056662 and the National Institutes of Health through grant R21 AR054867.

REFERENCES

[1] William H Simon. Scale effects in animal joints. i. articular cartilage thickness and compressive stress. *Arthritis & rheumatism*, 13(3):244–255, 1970.

[2] K. A. Athanasiou, M. P. Rosenwasser, J. A. Buckwalter T. I. Malinin, and V. C. Mow. Interspecies comparisons of in situ intrinsic mechanical properties of distal femoral cartilage. *J. orthop. res.*, 9:330–340, 1991.

[3] M. I. Froimson, A. Ratcliffe, T. R. Gardner, and V. C. Mow. Differences in patellofemoral joint cartilage material properties and their significance to the etiology of cartilage surface fibrillation. *Osteoarth. cart.*, 5:377–386, 1997.

[4] J. E. Kurkijarvi, M. J. Nissi, I. Kiviranta, J. S. Jurvelin, and M. T. Nieminen. Delayed gadolinium-enhanced mri of cartilage (dgemric) and t2 characteristics of human knee articular cartilage. *Magn. reson. med.*, 52:41–46, 2004.

[5] J. S. Jurvelin, J. P. A. Arokoski, E. B. Hunziker, and H. J. Helminen. Topographical variation of the elastic properties of articular cartilage in the canine knee. *J. biomech.*, 33:669–675, 2000.

[6] RK Korhonen, M Wong, Jari Arokoski, R Lindgren, HJ Helminen, EB Hunziker, and JS Jurvelin. Importance of the superficial tissue layer for the indentation stiffness of articular cartilage. *Medical engineering & physics*, 24(2):99–108, 2002.

[7] J. R. Parsons and J. Black. The viscoelastic shear behavior of normal rabbit articular cartilage. *J. Biomech.*, 10:21–29, 1977. DOI: 10.1016/0021-9290(77)90026-4.

[8] A. A. Spirt, A. F. Mak, and R. P. Wassell. Nonlinear viscoelastic properties of articular cartilage in shear. *J. Orthop. Res.*, 7:43–49, 1989. DOI: 10.1002/jor.1100070107.

[9] LA Setton, Van C Mow, and DSrt Howell. Mechanical behavior of articular cartilage in shear is altered by transection of the anterior cruciate ligament. *Journal of orthopaedic research*, 13(4):473–482, 1995.

[10] B. L. Wong, W. C. Bae, K. R. Gratz, M. Lotz, and R. L. Sah. Biomechanics of cartilage articulation: Effects on lubrication and degeneration on shear deformation. *Arthritis. Rheum.*, 58:2065–2074, 2008. DOI: 10.1002/art.23548.

[11] M. R. Buckley, J. P. Gleghorn, L. J. Bonassar, and I. Cohen. Mapping the depth dependence of shear properties in articular cartilage. *J. Biomech*, 41:2430–2437, 2008. DOI: 10.1016/j.jbiomech.2008.05.021.

[12] Savio LY Woo, Michael K Kwan, Thay Q Lee, Fred P Field, Jeffrey B Kleiner, and Richard D Coutts. Perichondrial autograft for articular cartilage shear modulus of neocartilage studied in rabbits. *Acta orthopaedica*, 58(5):510–515, 1987.

[13] William H Simon, Arthur Mak, and Adrienne Spirt. The effect of shear fatigue on bovine articular cartilage. *Journal of orthopaedic research*, 8(1):86–93, 1990.

[14] Wenbo Zhu, Van C Mow, Thomas J Koob, and David R Eyre. Viscoelastic shear properties of articular cartilage and the effects of glycosidase treatments. *Journal of orthopaedic research*, 11(6):771–781, 1993.

[15] Mats Stading and Robert Langer. Mechanical shear properties of cell-polymer cartilage constructs. *Tissue engineering*, 5(3):241–250, 1999.

[16] B. L. Wong and R. L. Sah. Mechanical asymmetry during articulation of tibial and femoral cartilages: Local and overall compressive and shear deformation and properties. *J. Biomech.*, 43:1689–1695, 2010. DOI: 10.1016/j.jbiomech.2010.02.035.

[17] M. R. Buckley, A. J. Bergou, J. Fouchard, L. J. Bonassar, and I. Cohen. High-resolution spatial mapping of shear properties in cartilage. *J. Biomech.*, 43:796–800, 2010. DOI: 10.1016/j.jbiomech.2009.10.012.

[18] M. R. Buckley, L. J. Bonassar, and I. Cohen. Localization of viscous behavior and shear energy dissipation in articular cartilage under dynamic shear loading. *J. Biomech. Eng.*, 35:031002–1–9, 2013. DOI: 10.1115/1.4007454.

[19] V. C. Mow, A. Ratcliffe, and A. R. Poole. Cartilage and diarthrodial joints as paradigms for hierarchical materials and structures. *Biomaterials*, 13:67–97, 1992. DOI: 10.1016/0142-9612(92)90001-5.

[20] Robert M Schinagl, Michael K Ting, Jeffrey H Price, and Robert L Sah. Video microscopy to quantitate the inhomogeneous equilibrium strain within articular cartilage during confined compression. *Annals of biomedical engineering*, 24(4):500–512, 1996.

[21] Robert M Schinagl, Donnell Gurskis, Albert C Chen, and Robert L Sah. Depth-dependent confined compression modulus of full-thickness bovine articular cartilage. *Journal of orthopaedic research*, 15(4):499–506, 1997.

[22] Nadeen O Chahine, Christopher CB Wang, Clark T Hung, and Gerard A Ateshian. Anisotropic strain-dependent material properties of bovine articular cartilage in the transitional range from tension to compression. *Journal of biomechanics*, 37(8):1251–1261, 2004.

[23] Janice H Lai and Marc E Levenston. Meniscus and cartilage exhibit distinct intra-tissue strain distributions under unconfined compression. *Osteoarthritis and cartilage*, 18(10):1291–1299, 2010.

[24] Steven Below, Steven P Arnoczky, Julie Dodds, Cynthia Kooima, and Norman Walter. The split-line pattern of the distal femur. *Arthroscopy: the journal of arthroscopic & related surgery*, 18(6):613–617, 2002.

[25] S Cowin and S Doty. *Tissue mechanics*. Springer Science, New York, 1st edition, 2007.

[26] J. Rieppo, J. Hallikainen, J. Jurvelin, I. Kiviranta, H. J. Helminen, and M. M. Hyttinen. Practical considerations in the use of polarized light microscopy in the analysis of the collagen network in articular cartilage. *Microsc. Res. Techniq.*, 71:279–287, 2008. DOI: 10.1002/jemt.20551.

[27] Clark T Hung, Eric G Lima, Robert L Mauck, Erica Taki, Michelle A LeRoux, Helen H Lu, Robert G Stark, X Edward Guo, and Gerard A Ateshian. Anatomically shaped osteochondral constructs for articular cartilage repair. *Journal of biomechanics*, 36(12):1853–1864, 2003.

[28] Clark T Hung, Robert L Mauck, Christopher C-B Wang, Eric G Lima, and Gerard A Ateshian. A paradigm for functional tissue engineering of articular cartilage via applied physiologic deformational loading. *Annals of biomedical engineering*, 32(1):35–49, 2004.

[29] John G Lane, William L Tontz Jr, Scott T Ball, Jennifer B Massie, Albert C Chen, Won C Bae, Michael E Amiel, Robert L Sah, and David Amiel. A morphologic, biochemical, and biomechanical assessment of short-term effects of osteochondral autograft plug transfer in an animal

model. *Arthroscopy: the journal of arthroscopic & related surgery*, 17(8):856–862, 2001.

[30] Kai Mithoefer, Karen Hambly, Stefano Della Villa, Holly Silvers, and Bert R Mandelbaum. Return to sports participation after articular cartilage repair in the knee scientific evidence. *The american journal of sports medicine*, 37(1 suppl):167S–176S, 2009.

[31] Anil S Ranawat, Armando F Vidal, Chris T Chen, Jonathan A Zelken, A Simon Turner, and Riley J Williams III. Material properties of fresh cold-stored allografts for osteochondral defects at 1 year. *Clinical orthopaedics and related research*, 466(8):1826–1836, 2008.

[32] Mark C van Turnhout, Henk Schipper, Bas Engel, Willem Buist, Sander Kranenbarg, and Johan L van Leeuwen. Postnatal development of collagen structure in ovine articular cartilage. *Bmc developmental biology*, 10(1):62, 2010.

3.7 Supplemental Information

3.7.1 Additional data relevant for verification of experimental methods

To track the strain field of the cartilage tissue during deformation, we have used only a single photobleached line instead of the five parallel lines described in previous work[1]. Thus, the experimental technique requires additional verification. In Figure 3.6 below, we have compared the effects of a 1, 2, 3, 4, and 5 line

tracking method. As can be readily seen, additional photobleached lines do not enhance the quality of the data or significantly reduce experimental noise. We therefore conclude that the number of photobleached lines being tracked does not alter our or conclusions.

3.7.2 Extended discussion

Our observations also have subtle implications for theories of cartilage morphogenesis. Previous work hypothesized that anatomic and depth-dependent variations in the collagen network underlying AC arise from in vivo loading patterns[2]. Supporting this hypothesis, studies have shown that the collagen network remodels with age[3, 4]. The results presented here with neonatal bovine tissue show that large depth-dependent variations in mechanical properties can arise without a mechanism for remodeling that depends on normal loading bearing activities. Further investigations on the interactions between the local mechanical properties, loading, and remodeling, could help shed further light on cartilage morphogenesis.

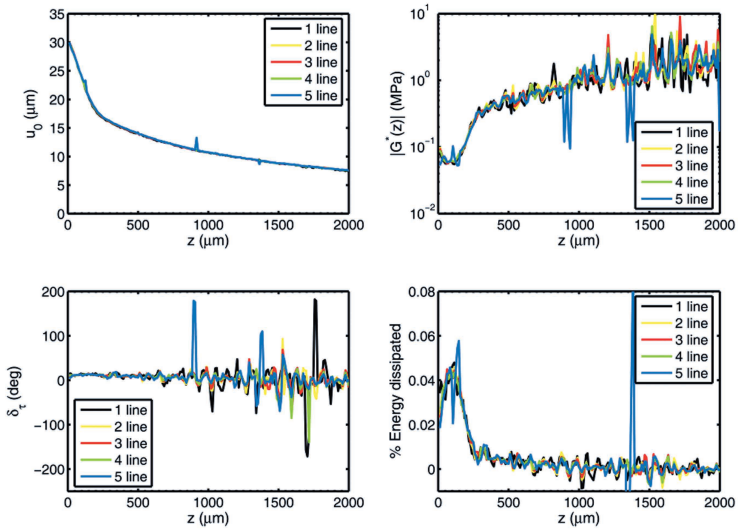

Figure 3.6: Here, we show measurements of a single cartilage sample that has had up to 5 parallel lines photobleached on to it to track tissue deformations. In the top left, we show the shear amplitude displacement u_0 as a function of depth z. The only noticeable differences between these measurements are three spikes in the 5-line measurement arising from the presence of blood vessels that interrupted the fifth photobleached line. In the top right, we plot the depth-dependent shear modulus where we see that these spikes give rise to localized fluctuations. Nevertheless, the overall comparisons between the five measurements are indistinguishable in any way. The same can be said for the depth-dependent phase angle (lower left) and the depth-dependent energy dissipation (lower right). We therefore conclude that the number of photobleached lines being tracked does not significantly alter our measurements.

REFERENCES

[1] M. R. Buckley, A. J. Bergou, J. Fouchard, L. J. Bonassar, and I. Cohen. High-resolution spatial mapping of shear properties in cartilage. *J. Biomech.*, 43:796–800, 2010. DOI: 10.1016/j.jbiomech.2009.10.012.

[2] Dennis R Carter and Marcy Wong. Modelling cartilage mechanobiology. *Philosophical transactions of the royal society of london. series b: biological sciences*, 358(1437):1461–1471, 2003.

[3] J. Rieppo, J. Hallikainen, J. Jurvelin, I. Kiviranta, H. J. Helminen, and M. M. Hyttinen. Practical considerations in the use of polarized light microscopy in the analysis of the collagen network in articular cartilage. *Microsc. Res. Techniq.*, 71:279–287, 2008. DOI: 10.1002/jemt.20551.

[4] Mark C van Turnhout, Henk Schipper, Bas Engel, Willem Buist, Sander Kranenbarg, and Johan L van Leeuwen. Postnatal development of collagen structure in ovine articular cartilage. *Bmc developmental biology*, 10(1):62, 2010.

CHAPTER 4

STRUCTURE-FUNCTION RELATIONS AND RIGIDITY PERCOLATION IN THE SHEAR PROPERTIES OF ARTICULAR CARTILAGE

Jesse L. Silverberg, Aliyah R. Barrett, Moumita Das, Poul B. Petersen, Lawrence J. Bonassar, and Itai Cohen, *under review*.

4.1 Abstract

Among mammalian soft tissues, articular cartilage is particularly interesting as it can endure 60+ years of daily mechanical loading despite having minimal regenerative capacity. This remarkable resilience may be due to the depth-dependent mechanical properties, which have been shown to localize strain and energy dissipation. Based on qualitative observations, it has been proposed that these properties arise from the depth-dependent collagen fiber orientation. Nevertheless, this structure-function relationship has not yet been quantified. Here, we use confocal elastography, quantitative polarized light microscopy, and Fourier transform infrared imaging to make same-sample measurements of the depth-dependent shear modulus, collagen fiber organization, and extracellular matrix concentration in neonatal bovine articular cartilage. We find weak correlations between the shear modulus $|G^*|$ and both the collagen fiber orientation and polarization. We find a much stronger correlation between $|G^*|$ and the concentration of collagen fibers. Interestingly, very small changes in collagen volume fraction v_c lead to orders of magnitude changes in the modulus with $|G^*|$ scaling as $(v_c - v_0)^\xi$. Such dependencies are observed in the rheology of other biopolymer networks whose structure exhibits rigidity percolation phase transitions. Along these lines, we propose that the collagen network is near a

percolation threshold that gives rise to these large mechanical variations and strain-localization at the tissue's surface.

4.2 Introduction

Healthy mammalian long bones are protected by a living tissue known as articular cartilage (AC). Recognized for its role in facilitating normal joint functioning, AC has a unique combination of material properties[1]. For example, it is entirely self-assembled[2, 3] and can endure 60+ years of daily loading despite an inability to regenerate normal tissue when injured[4]. These characteristics are *highly* desirable for tissue engineering[5] and soft robotics[6] applications, however the relevant design principles remain largely unknown. While ongoing studies continue to make progress towards understanding AC's microscopic structure[7, 8, 9, 10, 11], recent advances in experimental techniques have enabled higher resolution measurements of the spatial heterogeneity in AC's mechanical properties. For example, confocal rheology techniques have combined high-resolution optical and force data to quantify depth-dependent variations in the shear properties[12, 13]. With this technique, a spatially localized region was found near the tissue surface with a shear modulus up to 100 times smaller than the typical 1 MPa bulk-averaged value[14, 15, 12, 13, 16, 17, 18]. This region was also found to dissipate $\approx$ 90% of the energy imparted during shear, suggesting a specialized function as a biological shock absorber[18, 19]. The combination of structural data and improved measurements of local mechanical properties opens the door to studies that correlate microscopic structure with mechanical function in AC.

Broadly, healthy AC is a fluid-filled porous medium composed primarily of water (60-85% wet weight), type II collagen (15-22%), and the large aggregating proteoglycan called aggrecan (4-7%)[1]. A significant development in the understanding of AC came when poroelasticity was first used to model its multi-component architecture with a continuum description[20, 21, 22]. This theoretical framework, which remains a cornerstone of the cartilage mechanics literature, enabled the interpretation of bulk-averaged compressive mechanical properties in terms of the underlying biopolymer network and interstitial fluid flow.

Here, we ask: what are the design principles underlying AC's depth-dependent shear properties? One hypothesis attributes the mechanical data to depth-dependent variations in collagen fiber organization[1, 23, 24, 25, 26, 27, 28, 29] (Fig. 4.1). Specifically, in the *tangential*, *mid*, and *deep zones*, collagen fibers are respectively aligned parallel, random, and perpendicular to the articular surface. While the exact details vary with animal, age, and location within the joint, the general schematic is largely conserved and superficially appears to correlate with mechanical data. Using natural biological variation as a means to vary material properties, we test this fiber-reinforced hypothesis with same-sample mechanical, structural, and compositional measurements. For small strains, we surprisingly find the shear modulus *does not* correlate with fiber organization, but rather, these large variations in the shear modulus ($\approx$ 100-fold) *do* correlate with small variations in matrix concentration ($\approx$ 2-fold). Similar behavior has been previously seen in reconstituted biopolymer networks and is a hallmark of a mechanical phase transition known as rigidity percolation[30, 31, 32, 33, 34, 35, 36, 37]. We adapt this class of models to account for the multi-component nature of AC, and show it can reproduce the empirical trends

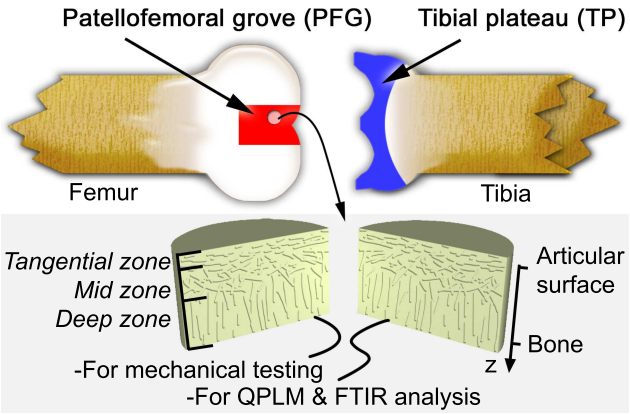

Figure 4.1: Schematic diagram of a bovine knee joint indicating sample harvesting sites. Cylindrical plugs of AC were removed from the joint, halved, and separated out for mechanical testing or biochemical analysis. AC is known to have three zones distinguished by collagen fiber orientation as indicated. The coordinate system is also shown, where the depth-wise direction z is 0 at the surface of the tissue, and increases toward the bone.

observed in our data.

4.3 Experimental Materials and Methods

4.3.1 Sample preparation

1-3 day old neonatal bovine knee joints were acquired from a local abattoir (Gold Medal Packing, Rome, NY). Cylindrical explants 3.5 mm thick and 6 mm in diameter were dissected from the patellofemoral grove (PFG) and tibial plateau (TP). Each sample was cut into two equal semi-cylindrical portions, one half being fixed in 10% PBS-buffered formalin for biochemical analysis, the other stored in phosphate buffered saline (PBS, Life Technologies, Grand Island, NY) for mechanical testing. In total, $n = 8$ samples were collected: 4 PFG sam-

ples and 4 TP samples from 2 knees. In the analysis presented below, we measure multiple distinct quantities from each sample and compare these quantities on a same-sample basis. Thus, for statistical purposes, the data can be considered as independently acquired, despite coming from 2 knees.

4.3.2 Confocal elastography

Prior to shear testing, each semi-cylindrical sample was soaked for 3 h in PBS with 7 mg/ml 5-dichlorotriazinylaminofluorescein (5-DTAF, Life Technologies, Carlsbad, CA), an all-protein stain. Samples were rinsed in PBS for 1 h to remove excess dye, and then loaded into a Tissue Deformation Imaging Stage (TDIS, Harrick Scientific, Pleasantville, NY). In this apparatus, two plates grip a sample, one of which applies shearing strains, while the other measures shearing stresses (see SI Fig. 4.1)[16, 19]. Samples were loaded so displacements were applied to the articular surface, while stress measurements were recorded in the deep zone. Every sample was held with a 7.5 ± 0.5% depth-wise compression along z and given 1 h to come to mechanical equilibrium. This time was chosen to be greater than the poroelastic relaxation time, which for our samples is ≈ 20 min[1]. Friction was sufficiently high at the articular surface to prevent slippage during shear. At the stress measurement plate, a small bit of cyanoacrylate glue was used to enhance contact. Samples were immersed in PBS to maintain tissue hydration during testing.

The TDIS was mounted onto a Zeiss LSM 510 confocal microscope (Carl Zeiss, Germany), where a line was photobleached onto the rectangular surface of the semi-cylinder parallel to the z axis. This line caused no damage to the tis-

sue and was used to facilitate automated computer tracking of the strain with a depth-wise resolution of 10.4 μm. Imaging of 1 Hz oscillatory shear at 1% peak amplitude was carried out with a 10x objective, and movies were acquired at 20 FPS throughout the entire depth of the tissue[16, 19]. All mechanical testing was performed within 24 hours of tissue harvesting, bypassing the necessity for antibiotics or protease inhibitors.

To obtain same-sample depth-dependent comparisons between mechanical and structural properties, measurements of the local compression profile were made before and after compression. Depth-wise measurements of axial compression were acquired by photobleaching a series of lines spaced 23 ± 1 μm apart parallel to the direction of shear. Images were acquired in the uncompressed state, and again in the equilibrated compressed state. Custom MATLAB software quantified the change in line spacing and produced a local depth-dependent axial strain $\epsilon_{zz}(z)$ that was used to facilitate comparisons between $|G^*(z)|$ (compressed) and QPLM/FTIR-I (uncompressed) data.

4.3.3 Quantitative polarized light microscopy (QPLM)

Half of each cylindrical explant was designated for shear testing, while the other half was fixed in formalin, embedded in paraffin wax, and sectioned into 4 μm thick slices. Sections for QPLM were placed on glass slides, dewaxed in 3 xylene baths for 2 minutes each, rehydrated in 3 baths of ethyl alcohol (100%, 95% and 70% ethanol, appropriately diluted with DI water) for 2 minutes each, and dyed with Picrosirius red for 1 h. Sections were then dunked 3 times each in two acetic water baths (5 mL glacial acetic acid to 1 L DI water), soaked for 2 min

each in 3 baths of ethyl alcohol (70%, 95%, and 100%), and laid out to dry in a fume hood. This histochemical staining is useful as it selectively binds to fibrillar collagen, enhancing tissue birefringence[38]. Staining was carried out on all samples simultaneously to ensure dye uniformity.

Once prepared, samples were placed on a brightfield microscope with a 4x objective and two independently rotating linear polarizers set 90° apart (Bruker, Billerica, MA). Incident light was polarized, passed through the sample, then passed through a second polarizer, producing a map of the local birefringence. By rotating the polarizers through an angle θ from 0° to 90° with respect to the tissue sample and recording images every 6°, we were able quantify the local light intensity variations. Fitting each pixel intensity $I(\theta)$ to the function $A_0 + A_1 \cos^2(2\theta - \phi)$, we measured the local polarization index, PI = $A_1/(A_1 + A_0)$, and the local fiber orientation ϕ, which corresponds to the direction that maximizes $I(\theta)$[23, 24]. Light intensity was adjusted to prevent pixel saturation, and all samples were imaged under identical lighting conditions. In our measurements, $\phi = 90°$ is parallel to the articular surface, while $\phi = 0° \equiv 180°$ is perpendicular.

4.3.4 Fourier transform infrared imaging (FTIR-I)

Sections 4 μm thick from each tissue sample were placed on 2 mm thick mid-IR transparent BaF_2 disks that were 25 mm in diameter (Spectral Systems, Hopewell Junction, NY). Though the sectioning plane was fixed, the section cutting direction was randomized to prevent systematic biases in section thickness due to cutting. Sections were dewaxed and rehydrated as described above.

Samples were loaded into a Bruker Hyperion 2000 FTIR-I (Bruker, Billerica,

MA) in transmission mode set to acquire data on wavenumbers between 600 and 4000 cm^{-1} with a resolution of 4 cm^{-1}. A 15x objective was used with a slit aperture configured to acquire spectra over a rectangular region 25×200 μm^2, where the long dimension was parallel to the articular surface. 15 background-corrected scans were repeated at a given measurement point and averaged to generate a single IR spectra. The acquisition window was translated along the tissue sample's z direction by a computer controlled stage to acquire measurements at 80 points spaced 25 μm apart.

Beer's law states that IR absorbance is proportional to molecular concentration, and as a corollary, two mixed species of molecules have additive contributions. Across all samples and spectra, we found the maximum IR absorbance did not exceed 0.3, demonstrating that the samples were thin enough to prevent deviations from Beer's law via molecular shadowing. At physiological concentrations, the spatial proximity of each molecule is sufficiently large that intermolecular interactions do not cause significant deviations from pure-compound spectra acquired at lower concentrations. While such interactions in dehydrated tissue sections may be stronger, our analysis is sufficiently coarse that it is insensitive to these subtle effects (see SI).

The two primary solid-matrix contributions to AC come from type II collagen and aggrecan. Hence, we used previously published pure-compound spectra where both compounds were extracted from bovine AC femoral condyles[39]. Each AC spectra was fit to a linear combination of the type II collagen spectrum, aggrecan spectrum, and a linear baseline over the spectral window from 900 to 1725 cm^{-1} (see SI)[40, 41]. This procedure has four fitting parameters for a spectra consisting of 147 data points: one multiplicative co-

efficient for each pure-compound spectra, and two coefficients for the baseline. The inclusion of a linear baseline correction accounts for instrument-specific deviations and drift[42]. The pure-compound fitting coefficients, which are proportional to the molecular concentration, were scaled to wet volume fractions by a multiplicative prefactor chosen to reproduce literature values for the bulk averages of 0.35 for collagen and 0.15 for aggrecan[43, 44, 45, 46]. Because AC contains Type-IX collagen, Type-XI collagen, elastin, small non-aggregating proteoglycans, and other matrix macromolecules only in trace amounts, their IR signatures, which are proportional to concentration, are negligible and were not included in the spectral fits.

4.4 Experimental results and discussion

4.4.1 Depth-dependent shear properties of AC

To study spatially localized variations in the shear properties of AC, the PFG ($n = 4$) and TP ($n = 4$) of neonatal bovine knee joints (Fig. 4.1) were selected as sites of interest because (i) they are the most distinct in terms of their local shear properties, (ii) offer two decades in variation of the shear modulus, and (iii) are transversely isotropic, which greatly simplifies the handling of tissue specimens due to in-plane orientational symmetry[18]. Defining the tissue's articulating surface to be $z = 0$, where increasing z moves toward the bone (Fig. 4.1), we treat the depth-dependent complex shear modulus $G^*(z)$ as a macroscopic tissue property. For small amplitude oscillatory shear, $G^*(z)$ is primarily elastic[18] (i.e., $\tan^{-1}[\text{Im } G^*/\text{Re } G^*] \lesssim 10°$). Plotting $|G^*(z)|$ for all 8 samples we observed a

compliant region near the articular surface where $0 \leq z \leq 100$ μm (Fig. 4.2, gray highlight). The numerical value of $|G^*(z)|$ in this region was typically 10 times less than the region where $z > 400$ μm for PFG samples, and 100 times less for TP samples.

To ensure no-slip contact during shear testing, samples were initially compressed 7.5±0.5% prior to mechanical testing and allowed to come to mechanical equilibrium. Structural measurements, however, were performed on uncompressed samples. To relate these data we use the measured local axial strain field, $\epsilon_{zz}(z)$. The compression data showed deviations from uniformity that were well fit by $\epsilon_{zz}(z) = \epsilon_0 - \epsilon_1 \exp(-z/\ell)$ where $\epsilon_0 = 0.075$ was the target strain, while $\epsilon_1 = 0.028$, $\ell = 680$ μm for PFG, and $\epsilon_1 = 0.038$, $\ell = 350$ μm for TP[1]. Though an overall small correction, this scaling of z was used to adjust QPLM/FTIR-I measurements so data at a given depth could be directly compared to $|G^*(z)|$. For each sample, this led to 80 measurements along the z axis, with an average spacing of 22 ± 2 μm, though specific spacing values varied according to $\epsilon_{zz}(z)$.

4.4.2 Depth-dependent collagen fiber organization

QPLM enabled measurements of structural variation with a resolution of 29 μm^2/pixel in the shear plane. These birefringence data produced spatial maps of two order parameters that quantify the degree of collagen fiber alignment and their preferred orientation[23, 24] (Fig. 4.3(A, B) inset). The polarization index (PI) takes values from 0 to 1, where PI = 0 corresponds to isotropically distributed fiber orientations, and PI = 1 corresponds to perfectly aligned fibers. The fiber orientation angle ϕ takes values from 0° to 180°, as the fiber direction

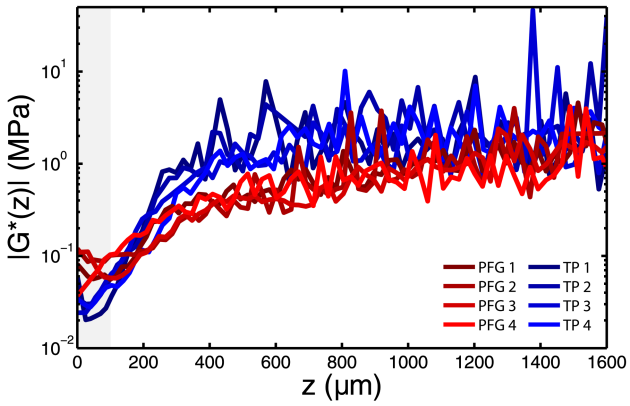

Figure 4.2: The measured shear modulus for all 8 samples is plotted on a log scale as a function of depth. Red curves are from the patellofemoral grove (PFG), while blue curves are from the tibial plateau (TP). The surface region highlighted in gray is found to be 10 to 100 times more compliant than the tissue at greater depths, and when compared to fiber organization data, corresponds to AC's tangential zone.

is symmetric with respect to rotations through 180°.

Averaging along the shear direction produced plots of the depth-dependent parameters $\langle \mathrm{PI}(z) \rangle$ and $\langle \phi(z) \rangle$ (Fig. 4.3(A, B)). Consistent with the known depth-dependent variations in collagen fiber organization, we found that fibers in the tangential zone where $z < 100\ \mu$m were more ordered and were aligned more parallel to the surface in comparison to fibers deeper in the tissue ($z > 100\ \mu$m). Though schematics of the depth-dependent collagen fiber network (Fig. 4.1) have similarities to the profile of $|G^*(z)|$, these data reveal the depth-dependent fiber organization is *qualitatively uncorrelated* with the shear modulus (gray shaded region in Fig. 4.2 and 4.3). Specifically, the QPLM data exhibit wide variations in the tangential zone, while the shear modulus data is essentially flat. To quantitatively test for structure-function correlations, we plot both order parameters against $|G^*(z)|$ (Fig. 4.3(C, D)). Linear regression analysis comparing $\log |G^*(z)|$ to $\langle \mathrm{PI}(z) \rangle$ ($R = 0.28$, $p < 0.01$) and $\langle \phi(z) \rangle$ ($R = 0.20$, $p < 0.01$)

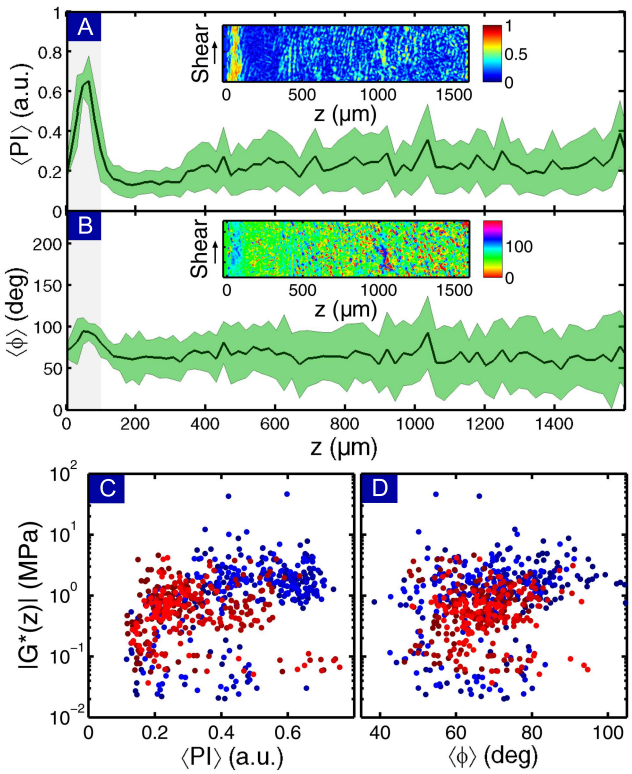

Figure 4.3: Example of (A) $\langle \mathrm{PI}(z) \rangle$ and (B) $\langle \phi(z) \rangle$ for sample PFG 1 illustrating typical depth-dependent structural variations. Green shaded bands correspond to ±1 standard deviation from the mean. Insets show 2D maps of each order parameter prior to being averaged along the shear direction. Gray shaded region highlights the tangential zone for comparison with the shear modulus data. We also note, $\phi = 0°$ runs parallel to the z axis, while $\phi = 90°$ runs parallel to the articular surface. Comparing (C) $\langle \mathrm{PI}(z) \rangle$ and (D) $\langle \phi(z) \rangle$ to $|G^*(z)|$ for all 8 samples reveals weak correlations. Red and blue coloring is coordinated to match Fig. 4.2.

confirmed the depth-dependent collagen fiber organization weakly varies with the depth-dependent shear modulus.

4.4.3 Depth-dependent matrix density

To quantify matrix constituents, we used FTIR-I to generate spatially resolved IR spectral maps that were decomposed into the sum of spectra from pure type II collagen and pure aggrecan (Fig. 4.4(A))[26, 27, 28, 29, 47, 48, 49]. The pure compound spectra were converted to the depth-dependent wet aggrecan volume fraction $v_a(z)$, and the depth-dependent wet collagen volume fraction $v_c(z)$ (Materials and Methods). These data show a decrease in matrix concentration near the articular surface where $z < 100$ μm, and an essentially constant concentration for $z > 400$ μm (Fig. 4.4(B) and SI). Visually comparing to depth-dependent mechanical data, we see qualitative correlations suggesting potential structure-function relationships (Fig. 4.2 and Fig. 4.4(B)). To quantitatively test these observations, we compare same-sample measurements of both $v_a(z)$ and $v_c(z)$ with $\log|G^*(z)|$ (Fig. 4.4(C, D)). Linear regression analysis confirms a high degree of correlation in both cases ($R = 0.82$, $p < 0.01$ for $v_a(z)$ and $R = 0.79$, $p < 0.01$ for $v_c(z)$). The aggrecan matrix alone is insufficient to account for the depth-dependent mechanics, as previous rheological studies of aggrecan gels at shear rates comparable to those used here have reported shear moduli in the $0.1 - 100$ Pa range[50]. Collagen fibers, however, are known to have Young's moduli in the GPa range, making it likely that their contribution dominates the overall AC shear mechanics. The apparent correlation between $v_a(z)$ and $|G^*(z)|$ can then be interpreted as a bi-product of the empirically linear relationship between $v_a(z)$ and $v_c(z)$, i.e., $v_a = (0.205 \pm 0.006)v_c + (0.035 \pm 0.002)$ ($R^2 = 0.87$; see Fig. 4.4(C) inset). The wider biophysical context therefore suggests the correlation between $v_c(z)$ and $|G^*(z)|$ may be causal, and hence collagen volume fraction drives AC's small-amplitude shear properties.

A remarkable feature of this data is the small (2-fold) change in collagen volume fraction coinciding with a very large (100-fold) change in shear modulus. From the view of theoretical mechanics[51, 52], simple composites and continuum approximations for entropic spring networks follow $|G^*(v_c)| \sim v_c$. Conversely, work on reconstituted biopolymer networks has found a critical scaling relation where the functional form for the modulus follows a power-law relation that depends on a threshold volume fraction v_0 below which the network loses integrity[30, 31, 32, 33, 34, 35, 36, 37]. Here, we take an agnostic approach and fit the data to the functional form $|G^*(v_c)| \sim (v_c - v_0)^\xi$, where $|G^*(v_c < v_0)| = 0$, and v_0 is varied from 0.0 to 0.2 (Fig. 4.4(D), gray lines; see SI). For $0 \leq v_0 \leq 0.15$ we find the fits for ξ have essentially indistinguishable residuals ($R^2 \approx 0.69$), with power-law exponents ranging from $\xi = 4.5 \pm 0.1$ when $v_0 = 0$, to $\xi = 2.4 \pm 0.1$ when $v_0 = 0.15$ (errors correspond to 95% confidence interval). While these fits minimize residuals for a given v_0, they tend to miss qualitative features such as the "knee" at $v_c \approx 0.3$. Choosing $v_0 = 0.16$ and $\xi = 1.7$ yields a curve that better captures these qualitative trends in the data indicating the functional form is sufficiently robust to capture such features (Fig. 4.4(D), black line, $R^2 = 0.68$). We find that for $v_0 = 0$ corresponding to a pure power-law, the exponent is too large to be consistent with a simple continuum model. An alternative explanation is that v_0 is finite and that the system is described by a critical scaling function similar to those found in reconstituted biopolymer networks. In this interpretation, for small strains, the subset of collagen fibers that transmit stresses behaves like a network of elastic fibers near the rigidity percolation phase transition. To further explore the empirical structure-function relation and the implications of these fits, we adapt a percolating fiber model for AC to study the volume fraction dependence of the shear modulus.

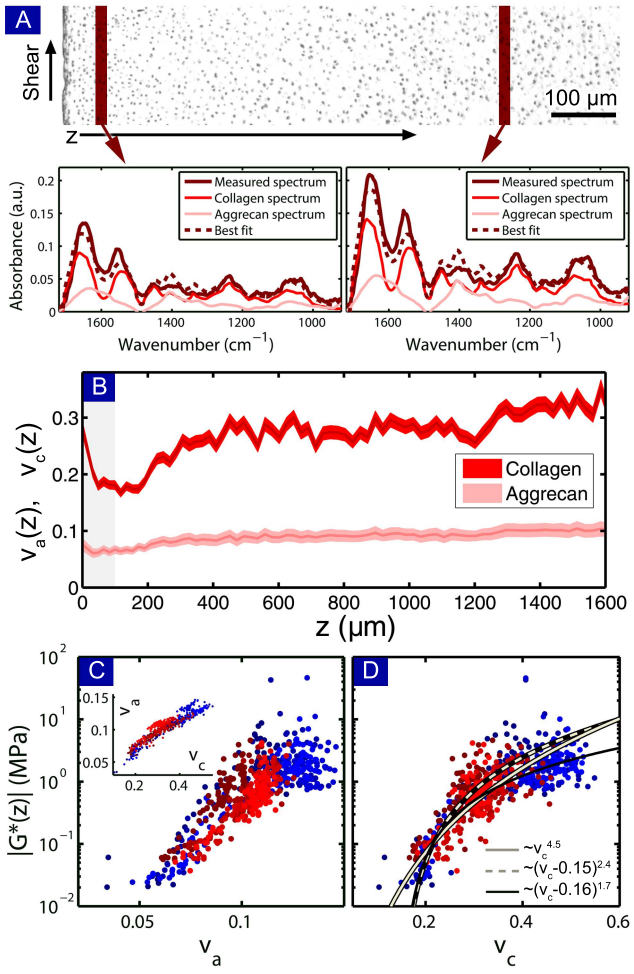

Figure 4.4: (A) An AC micrograph of sample PFG 1 illustrating two regions where FTIR-I measurements were performed. The two example spectra have been decomposed to a linear combination of a pure type II collagen spectrum and pure aggrecan spectrum. (B) Plotting the wet volume fraction of aggrecan $v_a(z)$ and type II collagen $v_c(z)$ reveals depth-dependent variations reminiscent of those in the shear modulus, as can be seen by directly comparing the gray shaded region. Plotting $|G^*(z)|$ against (C) $v_a(z)$ and (D) $v_c(z)$ for all same-sample measurements reveals a correlation between matrix density and mechanical function. Inset in (C) shows a linear relationship between v_a and v_c. Gray lines in (D) show best fits to the critical scaling function with the two extreme values of the threshold volume fraction, $v_0 = 0.0$ (solid) and $v_0 = 0.15$ (dashed). The solid black line fit captures qualitative trends in the data automated fitting routines may miss. Red and blue coloring in (C) and (D) is coordinated to match Fig. 4.2.

4.5 Rigidity Percolation Model

We consider a biopolymer rheology model that is known to produce large variations in the shear modulus with small variations in fiber content[30, 53, 54, 31, 55, 32, 33, 34, 35, 36, 37]. This scaling arises from a second-order mechanical phase transition known as *rigidity percolation*, and with some minor modifications, the generic model can be made to reflect the basic character of AC. The model makes the following assumptions:

(i) The cross-linked collagen network is approximated by a kagome lattice[35, 36, 37] (Fig. 4.5(A)), where every node is a freely rotating cross-link[56], every continuous series of colinear bonds constitute a fiber, and disorder is introduced by randomly removing bonds between nodes with probability $1 - p$, where $0 \leq p \leq 1$. The removal of bonds produces a broad distribution of fiber lengths, consistent with qualitative observations of AC. The fiber cross-linking occurs at lattice nodes homogeneously spaced by a minimum distance ℓ_c, but is assumed to have a concentration proportional to fiber density. Though the cross-linker distribution was not quantified here, these assumptions are consistent with previous work[57, 58, 59]. The kagome lattice was chosen over square and triangular lattices because its mechanical properties are independent of orientation, and each node connects only two fibers as is known to be the case for collagen cross-links.

(ii) Collagen fibers are modeled as linearly elastic rods with constant stretching modulus α and bending modulus κ. This simplification treats simulated fibers as having uniform radii[60], whereas real collagen fibers are known to vary in thickness[1, 57].

(iii) The hydrated aggrecan matrix is modeled as a simple elastic medium with shear modulus μ in parallel with the fiber network at the macroscale that also elastically resists transverse displacement of individual fibers at the microscale. This assumption neglects viscous effects on the grounds that $|G^*(z)|$ is predominantly elastic, and the poroelastic relaxation time (20 min) is much longer then the period of shear (1 s). It also neglects poroelastic fluid-flow effects and depth-dependencies in water content, consistent with the fact that small amplitude shear preserves volume, and hence does not induce fluid flows.

(iv) As an explicitly simplified model, all other compositional and structural elements in AC are neglected. This assumption is consistent with the lack of correlation between $|G^*(z)|$ and QPLM measurements (Fig. 4.3(C, D)), as well as data showing additional AC matrix proteins are only present in trace amounts[1, 57].

Simulations of the reinforced percolating fiber model utilized Fortran 90 and MATLAB to determine the linear response under 1% shear at zero temperature. For each set of parameters, 10 kagome networks containing $\sim 10^5$ nodes were randomly generated with a fraction of bonds $1 - p$ missing and the results averaged. Defining $\hat{\mathbf{r}}_{ij}$ to be the unit vector along bond ij, $\mathbf{u}_i$ as the displacement of the i^{th} lattice site, and $\mathbf{u}_{ij} = \mathbf{u}_i - \mathbf{u}_j$ as the displacement field, the deformation energy given by[30, 53, 54, 31, 32, 33, 61, 34, 35, 36, 37]

$$E = \frac{\alpha}{2} \sum_{\langle ij \rangle} p_{ij} \left(\mathbf{u}_{ij} \cdot \hat{\mathbf{r}}_{ij} \right)^2 + \frac{\kappa}{2} \sum_{\langle ijk \rangle} p_{ij} p_{jk} \left[\left(\mathbf{u}_{ji} + \mathbf{u}_{jk} \right) \times \hat{\mathbf{r}}_{ji} \right]^2 + \frac{\mu}{2} \sum_{\langle ij \rangle} p_{ij} \left[\mathbf{u}_{ij}^2 - \left(\mathbf{u}_{ij} \cdot \hat{\mathbf{r}}_{ij} \right)^2 \right] \tag{4.1}$$

was minimized for the macroscopic shear strain applied on the boundary. Here, p_{ij} is 1 if bond ij is occupied and 0 otherwise, $\sum_{\langle ij \rangle}$ represents sum over all bonds, and $\sum_{\langle ijk \rangle}$ represents the sum over pairs of colinear bonds sharing a node. The first term is the cost of bond extension or compression, and is proportional to

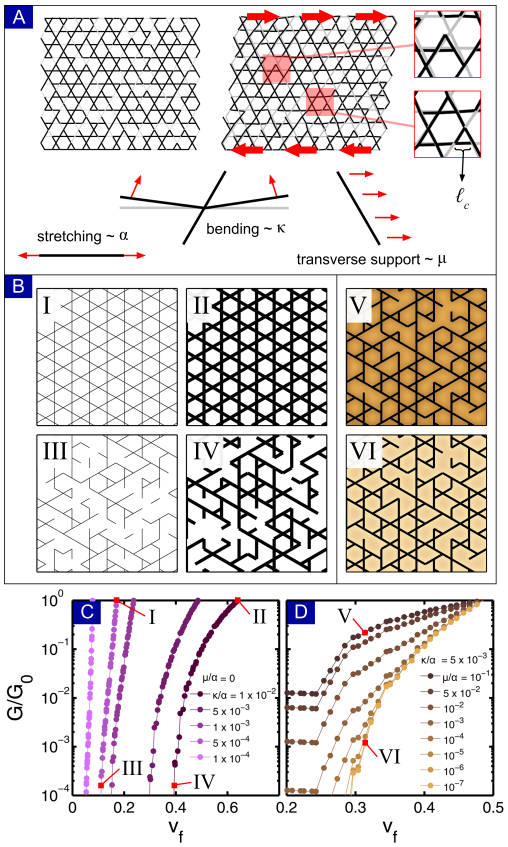

Figure 4.5: (A) A section of kagome lattice before and after shear illustrates local affine and non-affine deformations. Continuous black lines constitute fibers while light gray lines are missing bonds. Zooming in on the sheared lattice, we find affine deformations where light and dark colored bonds overlap, and non-affine deformations where they do not. Schematic diagrams illustrate the various energetic contributions included in the model described by Eq.(4.1). (B) In the absence of a reinforcing medium ($\mu/\alpha = 0$), four distinct regimes of the model corresponding to the four points labeled I - IV in (C) are schematically illustrated. In the presence of a reinforcing medium, such as points V and VI in (D), the strength of μ/α can be schematically illustrated by shading the background. (C) Exploring the model's dependence on the fiber bending-to-stretching ratio κ/α in the absence of a supporting medium ($\mu/\alpha = 0$) reveals a rigidity percolation phase transition as a function of v_f. (D) In the presence of a supporting medium ($\mu/\alpha > 0$), the phase transition is broadened, and $G(v_f)$ becomes dominated at low v_f by the modulus of the reinforcing medium. All modulus curves are normalized by $G_0 = G[v_f(p = 1)]$.

the fiber stretching modulus α. In terms of the Young's modulus Y, radius r, and cross-linking length l_c, we have $\alpha \sim Yr^2/\ell_c$. The second term arises from bending about the node connecting colinear bonds ij and jk, and is proportional to the scaled bending rigidity $\kappa \sim Yr^4/\ell_c^3$. The third term represents elastic deformations of the reinforcing medium in the direction perpendicular to $\hat{\mathbf{r}}_{ij}$, which is proportional to the effective gel modulus experienced by a 1D fiber $\mu \sim \mu_0 \ell_c/2\pi$ where μ_0 is the gel shear modulus[54, 62].

In simulations, the shear modulus $G(v_f)$ was measured as a function of fiber volume fraction $v_f = 8p(\kappa/\alpha)^{1/2}[1 - 2(\kappa/\alpha)^{1/2}]$, where $\kappa/\alpha \sim (r/\ell_c)^2$, and p is the fraction of occupied bonds. This expression is found by calculating the dependence of v_f on r for a unit cell. In each simulation run, p is systematically varied, the curve $G(v_f)$ is determined, and the results normalized by $G_0 = G[v_f(p = 1)] \sim \alpha/\ell_c$. As a simplification for quoting numeric values in the simulation results, we non-dimensionalize and rescale all lengths by setting $\ell_c \equiv 1$.

4.5.1 Simulations of network mechanics

We first simulated isotropic fiber networks without any reinforcing medium, i.e., a bare collagen network without aggrecan or depth-wise variations. Here, percolation is purely a function of the network geometry and is controlled by p. Consistent with simple rigidity percolation on kagome lattices, we find that for $p \leq p_0 \approx 0.6$ too many bonds were missing to maintain a spanning connected network. The elastic properties of the fibers in the network are governed by the fiber bending-to-stretching ratio κ/α, where physiological evidence suggests

$10^{-4} \leq \kappa/\alpha \leq 10^{-2}$[1]. Therefore, we plot the dimensionless modulus G/G_0 versus v_f for this range of κ/α (Fig. 4.5(B,C)).

The network mechanics are controlled by the balance of fiber stretching and bending. In all cases, response to shear is predominately bending dominated near the percolation transition. At larger volume fractions, the behavior depends on the specific value of κ/α (Fig. 4.5(C)). In the stiff limit where $\kappa/\alpha \sim 10^{-2}$, deformations are largely uniform at all length scales greater than ℓ_c. Here, $G(v_f)$ changes relatively slowly with v_f and is governed by stretching elasticity. When $\kappa/\alpha \sim 10^{-4}$, the filaments are floppier, deformations are non-affine[63], and the macroscopic mechanics are set by the spatially localized interplay between stretching and bending. Correspondingly, we find that the curves for G/G_0 are relatively steeper in this limit.

To the bare fiber network, we added a reinforcing medium characterized by elastic modulus μ, and investigated the parameter range $10^{-7} \leq \mu/\alpha \leq 10^{-1}$ (Fig. 4.5(B,D)). The lower bound is an estimate based on rheology experiments of pure aggrecan gels[50], while the upper bound is a coarse approximation for the effective modulus when it contains fragmented non-percolating fibers, i.e., it acts as fiber-reinforced composite. The underlying assumption for this bound is the shear modulus of the supporting medium is dominated by the rheology of the non-percolating fibers, and hence can be related to the stretching modulus α by setting μ_0 to the maximum possible value G_0. At the microscale, the reinforcing medium interacts with the fiber network by elastically resisting transverse deformations. At the macroscale, global deformations of the fiber network occur in parallel to the reinforcing gel, such that the macroscopic modulus is the sum of two contributions: $G(v_f) = G_{\text{fiber}}(v_f, \mu/\alpha) + \mu(1 - v_f)$. The first term is the

supported fiber network, which explicitly depends on μ, while the second is the gel shear modulus multiplied by its volume fraction $1 - v_f$.

In simulations, we found the reinforcing medium can significantly enhance $G(v_f)$ by suppressing non-affine deformations of the fiber network, especially near the percolation transition (Fig. 4.5(D)). Below the percolation transition, the modulus is dominated by the properties of the reinforcing medium. Collectively, the reinforcing medium sets a lower bound for the shear modulus while still allowing for orders of magnitude variation in $G(v_f)$ above the percolation threshold (Fig. 4.5(D)). Though these results were obtained with fixed $\kappa/\alpha = 5 \times 10^{-3}$, qualitatively similar trends were found at other values tested.

We interpret the model results to indicate that mechanical reinforcement of AC by aggrecan enhances the shear modulus and stiffens a bare collagen network. Optimizing the fit to experimental data with $\kappa/\alpha = 4{\times}10^{-3}$ and $\mu/\alpha = 10^{-1}$, we are able to qualitatively reproduce the empirical structure-function relationship between shear modulus and collagen volume fraction (Fig. 4.6(A), $R^2 = 0.59$). Redimensionalizing model parameters, setting $G_0 = 1$ MPa, and $r = 1$ μm[1], we can solve for the fiber's Young modulus $Y \sim 1$ GPa, the fiber cross-linking length $\ell_c \sim 10$ μm, and the reinforcing medium shear modulus $\mu_0 \sim 100$ kPa. These values for Y and ℓ_c are consistent with experiments that have measured the modulus[64], and TEM studies that have imaged individual collagen fibers[58]. The value for μ_0 indicates the modulus of the supporting medium is much higher than that of pure aggrecan gels, suggesting it is strongly reinforced with non-percolating fibers.

To illustrate how the simulation relates back to depth-dependent mechanical measurements, we replaced the isotropic random lattices with lattices that

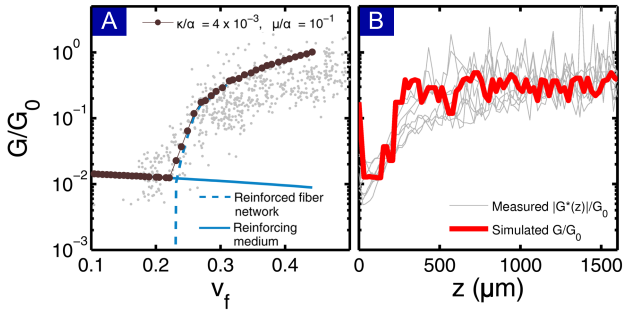

Figure 4.6: (A) For specific model parameters, a comparison between experiment (light gray points) and simulation (dark gray points) show reasonable agreement. The shear modulus is decomposed into contributions from the reinforced fiber network ($G_{\text{fiber}}(v_f, \mu/\alpha)$, dashed blue) and the reinforcing medium ($\mu(1 - v_f)$, solid blue). For low v_f, the fiber network does not percolate across the system and the reinforcing medium dominates. At a critical connectivity threshold, the fiber network forms a spanning cluster and stresses can be transmitted across the system. This effect rapidly dominates with increasing v_f, but becomes less sensitive at higher volume fractions. (B) The spatially homogeneous v_f is replaced with experimentally measured $v_c(z)$ from PFG 1 to generate a depth-dependent $G(z)$ profile (red), which when superimposed on experimental data (light gray lines) show qualitatively similar behavior.

have depth-wise variations. Spatial heterogeneity was introduced using the experimentally measured $v_c(z)$ from sample PFG 1 in place of the otherwise uniform v_f (see SI), and we constructed a G/G_0 versus z curve (Fig. 4.6(B) red line, $R^2 = 0.58$). As expected, this reproduced all of the salient features associated with the experimental measurements of the depth-dependent shear modulus.

4.6 Conclusions

In the present work, we distilled neonatal bovine AC microstructure into three basic elements: collagen fiber alignment, collagen content, and aggrecan con-

tent. Our empirical observations demonstrate that fiber alignment cannot fully account for this tissue's small amplitude shear properties. Moreover, we find that very small differences in the collagen content correlate with large changes in the shear modulus. As illustrated with the rigidity percolation model, this sensitivity can be explained by treating the collagen fibers as a percolating network that is near its rigidity threshold. As a design-principle, this shift of emphasis away from fiber alignment is conceptually important because it elevates the role of network connectivity, which tends to be lost in continuum elasticity. This has highly suggestive implications for tissue engineering, as it indicates that increasing network cross-linking and fiber rigidity may be more crucial then increasing collagen density when trying to fabricate materials that mimic AC's material properties.

Beyond the small strain measurements described here, large strain experiments present further challenges to understanding AC, where, for example, strain stiffening has been previously reported[13, 65, 61, 66]. Within the context of the percolating fiber network model, this behavior can arise from buckled fibers that experience no tension at small strain, and hence act as non-percolating elements. At large strain, these buckled fibers can straighten out, mediate stresses, and contribute to the mechanical response. This point is important, as it is not included in the proposed model and changes the interpretation of the rigidity percolation threshold as being strain-dependent. From this perspective, simulations which cross below the percolation threshold are still percolating from the connectivity point of view, but non-percolating in the sense that they do not mediate stresses. Experimental measurements of the relative fiber motion looking for bending, stretching, or sliding behavior would provide significant insights on this question. Clearly, progress exploring such

ideas requires more detailed simulations coupled with higher-resolution confocal elastography studies that further investigate the microscopic details of AC shear mechanics.

4.7 Acknowledgments

The authors thank P. Carubia for assistance with FTIR-I as well as L. Bartell, K. Novakofski, M. Delco, D. Griffin, H. Holmes, L. Fortier, E. Donnelly, N. Pleshko, the Cohen Lab, and the Bonassar Lab for useful insights and discussions. This work was supported by the National Science Foundation (NSF) under award number DMR-1056662, and the National Institutes of Health under award R21-AR062677. J.L.S. was supported by the NSF through a Graduate Research Fellowship. A.R.B. and P.B.P. were supported by the NSF through award number CHE-1151079. M.D. was partially supported by an internal RIT College of Science D-RIG grant. This work made use of the Cornell Center for Materials Research Facilities supported by the NSF under Award Number DMR-1120296.

REFERENCES

[1] V. C. Mow, A. Ratcliffe, and A. R. Poole. Cartilage and diarthrodial joints as paradigms for hierarchical materials and structures. *Biomaterials*, 13:67–97, 1992. DOI: 10.1016/0142-9612(92)90001-5.

[2] K. E. Kadler, D. F. Holmes, J. A. Trotter, and J. A. Chapman. Collagen fibril formation. *Biochem. j.*, 316:1–11, 1996.

[3] D. R. Eyre and J.-J. Wu. Collagen cross-links. *Top. Curr. Chem.*, 247:207–229, 2005. DOI: 10.1007/b103828.

[4] S. W. O'Driscoll. The healing and regeneration of articular cartilage. *J. Bone Joint Surg. Am.*, 80:1795–1812, 1998.

[5] D. J. Huey, J. C. Hu, and K. A. Athanasiou. Unlike bone, cartilage regeneration remains elusive. *Science*, 338:917–921, 2012. DOI: 10.1126/science.1222454.

[6] D. Trivedia, C. D. Rahna, W. M. Kierb, and I. D. Walkerc. Soft robotics: Biological inspiration, state of the art, and future research. *Appl. Bion. Biomech.*, 5:99–117, 2008. DOI: 10.1080/11762320802557865.

[7] P. Julkunen, P. Kiviranta, W. Wilson, J. S. Jurvelin, and R. K. Korhonen. Characterization of articular cartilage by combining microscopic analysis with a fibril-reinforced finite-element model. *J. biomech.*, 40:1862–1870, 2007. DOI: 10.1016/j.jbiomech.2006.07.026.

[8] P. Julkunen, W. Wilson, J. S. Jurvelin, J. Rieppo, C.-J. Qu, M. J. Lammi, and R. K. Korhonen. Stress relaxation of human patellar articular cartilage in unconfined compression: prediction of mechanical response by tissue composition and structure. *J. Biomech.*, 44:1978–1986, 2008. DOI: 10.1016/j.jbiomech.2008.03.026.

[9] L. Rieppo, S. Saarakkala, J. S. Jurvelin, and J. Rieppo. Prediction of compressive stiffness of articular cartilage using Fourier transform infrared spectroscopy. *J. Biomech.*, 44:1269–1275, 2013. DOI: 10.1016/j.jbiomech.2013.02.022.

[10] L. P. Rasanen, M. E. Mononen, M. T. Nieminen, E. Lammentausta, J. S. Jurvelin, R. K. Korhonen, and OAI-Investigators. Implementation of subject-specific collagen architecture of cartilage into a 2D computational model of a knee joint – Data from the Osteoarthritis Initiative (OAI). *J. Orthop. Res.*, 31:10–22, 2013. DOI: 10.1002/jor.22175.

[11] K. S. Halonen, M. E. Mononen, J. S. Jurvelin, J. Toyras, and R. K. Korhonen. Importance of depth-wise distribution of collagen and proteoglycans in articular cartilage – A 3D finite element study of stresses and strains in human knee joint. *J. biomech.*, 46:1184–1192, 2013. DOI: 10.1016/j.jbiomech.2012.12.025.

[12] B. L. Wong, W. C. Bae, K. R. Gratz, M. Lotz, and R. L. Sah. Biomechanics of cartilage articulation: Effects on lubrication and degeneration on shear deformation. *Arthritis. Rheum.*, 58:2065–2074, 2008. DOI: 10.1002/art.23548.

[13] M. R. Buckley, J. P. Gleghorn, L. J. Bonassar, and I. Cohen. Mapping the depth dependence of shear properties in articular cartilage. *J. Biomech*, 41:2430–2437, 2008. DOI: 10.1016/j.jbiomech.2008.05.021.

[14] J. R. Parsons and J. Black. The viscoelastic shear behavior of normal rabbit articular cartilage. *J. Biomech.*, 10:21–29, 1977. DOI: 10.1016/0021-9290(77)90026-4.

[15] A. A. Spirt, A. F. Mak, and R. P. Wassell. Nonlinear viscoelastic properties of articular cartilage in shear. *J. Orthop. Res.*, 7:43–49, 1989. DOI: 10.1002/jor.1100070107.

[16] M. R. Buckley, A. J. Bergou, J. Fouchard, L. J. Bonassar, and I. Cohen. High-resolution spatial mapping of shear properties in cartilage. *J. Biomech.*, 43:796–800, 2010. DOI: 10.1016/j.jbiomech.2009.10.012.

[17] B. L. Wong and R. L. Sah. Mechanical asymmetry during articulation of tibial and femoral cartilages: Local and overall compressive and shear deformation and properties. *J. Biomech.*, 43:1689–1695, 2010. DOI: 10.1016/j.jbiomech.2010.02.035.

[18] J. L. Silverberg, S. Dillavou, L. J. Bonassar, and I. Cohen. Anatomic variation of depth-dependent mechanical properties in neonatal bovine articular cartilage. *J. Orthop. Res.*, 31:686–691, 2013. DOI: 10.1002/jor.22303.

[19] M. R. Buckley, L. J. Bonassar, and I. Cohen. Localization of viscous behavior and shear energy dissipation in articular cartilage under dynamic shear loading. *J. Biomech. Eng.*, 35:031002–1–9, 2013. DOI: 10.1115/1.4007454.

[20] V. C. Mow, S. C. Kuei, W. M. Lai, and C. G. Armstrong. Biphasic creep and stress relaxation of articular cartilage in compression: Theory and experiments. *J. Biomech. Eng.*, 102:73–84, 1980. DOI: 10.1115/1.3138202.

[21] V. C. Mow, M. H. Holmes, and W. M. Lai. Fluid transport and mechanical properties of articular cartilage: A review. *J. Biomech.*, 17:377–394, 1984. DOI: 10.1016/0021-9290(84)90031-9.

[22] W. M. Lai, J. S. Hou, and V. C. Mow. A triphasic theory for the swelling and deformation behaviors of articular cartilage. *J. Biomech. Eng.*, 113:245–258, 1991. DOI: 10.1115/1.2894880.

[23] P. Julkunen, J. Iivarinen, P. A. Brama, J. Arokoski, J. S. Jurvelin, and H. J. Helminen. Maturation of collagen fibril network structure in tibial and femoral cartilage of rabbits. *Osteoarthr. Cartilage*, 18:406–415, 2010. DOI: 10.1016/j.joca.2009.11.007.

[24] J. Rieppo, J. Hallikainen, J. Jurvelin, I. Kiviranta, H. J. Helminen, and M. M. Hyttinen. Practical considerations in the use of polarized light microscopy in the analysis of the collagen network in articular cartilage. *Microsc. Res. Techniq.*, 71:279–287, 2008. DOI: 10.1002/jemt.20551.

[25] J. Rieppo, M. M. Hyttinen, E. Halmesmaki, H. Ruotsalainen, A. Vasara, I. Kiviranta, J. S. Jurvelin, and H. J. Helminen. Changes in spatial collagen content and collagen network architecture in porcine articular cartilage during growth and maturation. *Osteoarthr. Cartilage*, 17:448–455, 2009. DOI: 10.1016/j.joca.2008.09.004.

[26] N. P. Camacho, P. West, P. A. Torzilli, and R. Mendelsohn. FTIR microscopic imaging of collagen and proteoglycan in bovine cartilage. *Biopolymers*, 62:1–8, 2000.

[27] X. Bi, G. Li, S. B. Doty, and N. P. Camacho. A novel method for determination of collagen orientation in cartilage by Fourier transform infrared imaging spectroscopy FT-IRIS. *Osteoarthr. Cartilage*, 13:1050–1058, 2005. DOI: 10.1016/j.joca.2005.07.008.

[28] X. Bi, X. Yang, M. P. G. Bostrom, and N. P. Camacho. Fourier transform infrared imaging spectroscopy investigation in the pathogenesis and repair

of cartilage. *Biochim. Biophys. Acta*, 1758:934–941, 2006. DOI: 10.1016/j.bbamem.2006.05.014.

[29] Y. Xia, N. Ramakrishnan, and A. Bidthanapally. The depth-dependent anisotropy of articular cartilage by Fourier-transform infrared imaging (FTIR). *Osteoarthr. Cartilage*, 15:780–788, 2007. DOI: 10.1016/j.joca.2007.01.007.

[30] D. A. Head, A. J. Levine, and F. C. MacKintosh. Distinct regimes of elastic response and deformation modes of cross-linked cytoskeletal and semi-flexible polymer networks. *Phys. Rev. e*, 68:061907–1–14, 2003. DOI: 10.1103/PhysRevE.68.061907.

[31] J. Wilhelm and E. Frey. Elasticity of stiff polymer networks. *Phys. rev. lett.*, 68:061907–1, 2003. DOI: 10.1103/PhysRevE.68.061907.

[32] C. P. Broedersz, X. Mao, T. C. Lubensky, and F. C. MacKintosh. Criticality and isostaticity in fibre networks. *Nature phys.*, 7:983–988, 2011. DOI: 10.1038/nphys2127.

[33] R. C. Picu. Mechanics of random fiber networks - a review. *Soft matter*, 7:6768–6785, 2011. DOI: 10.1039/C1SM05022B.

[34] M. Das, D. A. Quint, and J. M. Schwarz. Redundancy and cooperativity in the mechanics of compositely crosslinked filamentous networks. *PLoS ONE*, 7:e35939–1–11, 2012. DOI: 10.1371/journal.pone.0035939.

[35] A. Souslov, A. J. Liu, and T. C. Lubensky. Elasticity and response in nearly isostatic periodic lattices. *Phys. rev. lett.*, 103:205503–1, 2009. DOI: 10.1103/PhysRevLett.103.205503.

[36] K. Sun, A. Souslov, X. Mao, and T. C. Lubensky. Surface phonons, elastic response, and conformal invariance in twisted kagome lattices. *Proc. natl. acad. sci.*, 109:12369–12374, 2012. DOI: 10.1073/pnas.1119941109.

[37] X. Mao, O. Stenull, and T. C. Lubensky. Elasticity of a filamentous kagome lattice. *Phys. rev. e*, 87:42602–1, 2013. DOI: 10.1103/PhysRevE.87.042602.

[38] L. C. U. Junqueira, G. Bignolas, and R. R. Brentani. Picrosirius staining plus polarization microscopy, a specific method for collagen detection in tissue sections. *Histochem. J.*, 11:447–455, 1979. DOI: 10.1080/11762320802557865.

[39] L. Rieppo, S. Saarakkala, T. Narhi, J. Holopainen, M. Lammi, H. J. Helminen, J. S. Jurvelin, and J. Rieppo. Quantitative analysis of spatial proteoglycan content in articular cartilage with Fourier transform infrared imaging spectroscopy: Critical evaluation of analysis methods and specificity of the parameters. *Microsc. Res. Techniq.*, 73:503–512, 2010. DOI: 10.1002/jemt.20789.

[40] J. Yin and Y. Xia. Macromolecular concentrations in bovine nasal cartilage by Fourier transform infrared imaging and principle component regression. *Appl. Spectrosc.*, 64:1199–1208, 2010. DOI: 10.1366/000370210793335124.

[41] L. Rieppo, J. Rieppo, J. S. Jurvelin, and S. Saarakkala. Fourier transform infrared spectroscopic imaging and multivariate regression for prediction of proteoglycan content of articular cartilage. *PLoS ONE*, 7:1–8, 2012. DOI: 10.1371/journal.pone.0023244.

[42] Brian Smith. *Fundamentals of fourier transform infrared spectroscopy*. CRC Press, Boca Raton, 1st edition, 2006.

[43] A. K. Williamson, A. C. Chen, and R. L. Sah. Compressive properties and function-composition relationships of developing bovine articular cartilage. *J. Orthop. Res.*, 19:1113–1121, 2001. DOI: 10.1016/S0736-0266(01)00052-3.

[44] H. E. Panula, M. Hyttinen, J. P. A. Arokoski, T. K. Langsjo, A. Pelttari, I. Kiviranta, and H. J. Helminen. Articular cartilage superficial zone collagen biregringence reduced and cartilage thickness increased before surface fibrillation in experimental osteoarthritis. *Ann. Rheum. Dis.*, 57:237–245, 1998. DOI: 10.1136/ard.57.4.237.

[45] T. K. Langsjo, M. Hyttinen, A. Pelttari, K. Kiraly, J. Arokoski, and H. J. Helminen. Electron microscopic stereological study of collagen fibrils in bovine articular cartilage. *J. Annat.*, 195:281–293, 1999. DOI: 10.1046/j.1469-7580.1999.19520281.x.

[46] N. K. Simha, M. Fedewa, P. H. Leo, J. L. Lewis, and T. Oegema. A composites theory predicts the dependence of stiffness on cartilage culture tissues on collagen volume fraction. *J. biomech.*, 32:503–509, 1999. DOI: 10.1016/S0021-9290(98)00185-7.

[47] J. Yin, Y. Xia, and M. Lu. Concentration profiles of collagen and proteoglycan in articular cartilage by Fourier transform infrared imaging and principal component regression. *Spectrochim Acta A-M*, 88:90–96, 2012. DOI: 10.1016/j.saa.2011.12.002.

[48] Y. Xia, D. Mittelstaedt, N. Ramakrishnan, M. Szarko, and A. Bidthanapally. Depth-dependent anisotropies of amides and sugar in perpendic-

ular and parallel sections of articular cartilage by Fourier transform infrared imaging. *Microsc. Res. Techniq.*, 74:122–132, 2011. DOI: 10.1002/jemt.20881.

[49] Y. Xia, H. Alhadlaq, N. Ramakrishnan, A. Bidthanapally, F. Badar, and M. Lu. Molecular and morphological adaptations in compressed articular cartilage by polarized light microscopy and Fourier-transform infrared imaging. *J. Struct. Biol.*, 164:88–95, 2008. DOI: 10.1016/j.jsb.2008.06.009.

[50] V. C. Mow, A. F. Mak, W. M. Lai, L. C. Rosenberg, and L.-H. Tang. Viscoelastic properties of proteoglycan subunits and aggregates in varying solution concentrations. *J. Biomech.*, 17:325–338, 1984. DOI: 10.1016/0021-9290(84)90027-7.

[51] S Cowin and S Doty. *Tissue mechanics*. Springer Science, New York, 1st edition, 2007.

[52] David Boal. *Mechanics of the cell*. Cambridge University Press, New York, 2nd edition, 2012.

[53] M. Das, F. C. Mackintosh, and A. J. Levine. Effective medium theory of semiflexible filamentous networks. *Phys. rev. lett.*, 99:038101–1, 2007.

[54] Moumita Das, Alex J Levine, and FC MacKintosh. Buckling and force propagation along intracellular microtubules. *Epl (europhysics letters)*, 84(1):18003, 2008.

[55] A. R. Missel, M. Bai, W. S. Klug, and A. J. Levine. Affine-nonaffine transitions in networks of nematically ordered semiflexible polymers. *Phys. rev. e*, 82:041907–1, 2010.

[56] J.-J. Wu, P. E. Woods, and D. R. Eyre. Identification of cross-linking sites in bovine cartilate type ix collagen reveals an antiparallel type ii-type ix molecular relationship and type ix to type ix bonding. *J. bio. chem.*, 267:23007–23014, 1992.

[57] D. Eyre. Collagen of articular cartilage. *Arthritis. res.*, 4:30–35, 2002. DOI: 10.1186/ar380.

[58] A. R. Poole, I. Pidoux, A. Reiner, and L. Rosenberg. An immunoelectron microscope study of the organization of proteoglycan monomer, link protein, and collagen in the matrix of articular cartilage. *J. cell bio.*, 93:921–937, 1982.

[59] Ruud A. Bank, M. T. Bayliss, Floris P. J. G. Lafeber, Alice Maroudas, and Johan M. Tekoppele. Ageing and zonal variation in post-translational modification of collagen in normal human articular cartilage. *Biochem. j.*, 330:345–351, 1998.

[60] L. D. Landau and E. M. Lifshitz. *Landau and lifshitz course of theoretical physics volume 7: theory of elasticity*. Butterworth Heinemann, New Delhi, 3rd edition, 1986.

[61] A. Stein, D. A. Vader, D. A. Weitz, and L. M. Sander. The micromechanics of three-dimensional collagen-I gels. *Complexity*, 16:22–28, 2011.

[62] J. L. Silverberg, R. D. Noar, M. S. Packer, M. J. Harrison, C. L. Henley, I. Cohen, and S. J. Gerbode. 3d imaging and mechanical modeling of helical buckling in medicago truncatula plant roots. *Proc. natl. acad. sci.*, 109:16794–16799, 2012. DOI: 10.1073/pnas.1209287109.

[63] C. Heussinger and E. Frey. Floppy modes and nonaffine deformations in random fiber networks. *Phys. rev. lett.*, 97:105501–1, 2006.

[64] V. K. Yadavalli, D. V. Svintradze, and R. M. Pidaparti. Nanoscale measurements of the assembly of collagen to fibrils. *Int. j. biol. macromol.*, 46:458–464, 2010.

[65] Richard C. Arevalo, Jeffrey S. Urbach, and Daniel L. Blair. Size-dependent rheology of Type-I collage networks. *Biophys. j.*, 99:L65–67, 2010. DOI: 10.1016/j.bpj.2010.08.008.

[66] M. Sheinman, C. P. Broedersz, and F. C. MacKintosh. Nonlinear effective-medium theory of disordered spring networks. *Phys. rev. e*, 85:021801–1, 2012.

4.8 Supplemental Information

4.8.1 Nomenclature

For convenience, we include here a nomenclature of important terms and symbols used in the main text.

Terms

- AC - Articular Cartilage
- TDIS - Tissue Deformation Imaging Stage
- QPLM - Quantitative Polarized Light Microscopy
- FTIR-I - Fourier Transform Infrared Imaging
- PFG - Patellafemoral Groove

- TP - Tibial Plateau

Symbols

- z - The coordinate describing depth into an AC sample where $z = 0$ is the articular surface and increasing z moves toward the bone.
- $|G^*(z)|$ - The magnitude of the depth-dependent complex shear modulus.
- $\langle \mathrm{PI}(z) \rangle$ - The transversely averaged depth-dependent polarization index where $\langle \mathrm{PI}(z) \rangle = 0$ corresponds to a perfectly isotropic distribution of collagen fibers and $\langle \mathrm{PI}(z) \rangle = 1$ corresponds to perfectly aligned collagen fibers.
- $\langle \phi(z) \rangle$ - The transversely averaged depth-dependent fiber orientation where $\langle \phi(z) \rangle = 0^\circ \equiv 180^\circ$ is perpendicular to the articular surface and $\langle \phi(z) \rangle = 90^\circ$ is parallel to the articular surface.
- $v_a(z)$ - The depth-dependent aggrecan wet volume fraction.
- $v_c(z)$ - The depth-dependent collagen wet volume fraction.
- v_f - The fiber volume fraction used in the rigidity percolation model. Note: This quantity is spatially homogeneous and should be distinguished from $v_c(z)$, which is used to describe experimental data. In the main text and in Fig. 4.14 below, we show that $v_c(z)$ can be used in place of v_f to generate spatially heterogeneous depth-dependent lattices.
- p - The fraction of occupied bonds in the rigidity percolation model.
- ℓ_c - The bond length in the rigidity percolation model.
- α - The stretching modulus of fibers in the rigidity percolation simulation.
- κ - The bending modulus of fibers in the rigidity percolation simulation.

- μ - The shear modulus of the reinforcing medium in the rigidity percolation simulation.

4.8.2 Articular cartilage structure and extended comments on the compressive properties

A large body of literature exists on articular cartilage (AC) biochemistry and biomechanics. Here, we briefly summarize relevant portions of this literature, which though non-essential for our main arguments, provides a more detailed background for non-experts in this field. Much of the content provided here can be found in a more detailed review[1].

The macroscopic mechanical properties of articular cartilage (AC) emerge from an multi-scale structural hierarchy with characteristic length scales set by tropocollagen molecules (length $\approx$ 300 nm), collagen fibrils (1 – 10 μm), collagen fibers (0.1 – 1 mm), and bulk tissue (1 – 10 mm). The orientation of collagen fibers are known to vary across the thickness of the tissue and can be broadly categorized into zones. While the specifics of this organization vary with animal, age, and location within the joint, the general schematic (Fig. 1, main text) is largely conserved. In addition to the collagen network, there also exists an interpenetrating proteoglycan network that consists of aggrecan molecules linked together through a backbone of hylauronic acid. This gel-like material carries a net negative electric charge and attracts water molecules into the collagen network. In turn, an osmotic pressure, which at physiological conditions ranges from 0.1 to 0.2 MPa, is generated that swells the collagen network, placing it in tension and providing a means to rigidify the otherwise floppy collagen

network. Though the proteogycan network structure and content vary with age and disease, its physical interactions with the collagen network can be both electrostatic and mechanical. In the former, negative charge groups on the aggrecan interact with positive charge groups on collagen fibrils providing cohesion without forming covalent bonds. In the latter, there is evidence of frictional interactions between the collagen and proteoglycan networks.

Under externally applied axial tension, the mechanical properties are dominated by the collagen network, while under compression, the mechanics are dominated by the resistance of fluid flow through the porous collagen network. This particular feature is unique because many polymer systems couple the osmotic and tensile properties to the same microstructure. Indeed, these compressive properties of AC are well studied, and have been examined as function of depth, direction, collagen density, and fiber orientation[1, 2, 3, 4, 5, 6, 7, 8, 9, 10, 11, 12, 13, 14, 15]. Among this work, it has been observed the depth-dependent confined compression modulus of adult bovine PFG is a factor of 10 to 20 more compliant near the articular surface relative to the deep zone[13]. This point is important to note, as studies of random elastic networks have shown that a vanishing shear modulus, which arises due to reduced network connectivity, is associated with a vanishing bulk modulus[16]. Thus, evidence for this generic prediction of rigidity percolation is already present in the literature on AC's compressive properties, providing further support for the microscopic interpretation of the depth-dependent shear modulus put forth in the main text.

4.8.3 Experiment Schematics

In this work we employed three different experimental techniques to quantify mechanical and structural aspects of articular cartilage (AC) with high spatial resolution. As described in the main text, confocal elastography was used to study shear mechanical properties, QPLM was used to study collagen fiber organization, and FTIR-I was used to study matrix density. Here, we supplement descriptions of these techniques provided in the main text with schematic diagrams (Fig. 4.7).

4.8.4 Additional QPLM data

In the main text, we show the depth-dependent profile of the polarization index $\langle \mathrm{PI}(z) \rangle$ and fiber orientation $\langle \phi(z) \rangle$, along with error bars indicating ±1 standard deviation arising from the average along the transverse direction. To provide a sense of sample-to-sample variation, we show here the depth-dependent measurements for all 8 samples (Fig. 4.8). Generally, we find in the tangential zone ($z < 100$ μm) that all samples have a high degree of collagen fiber alignment with $\langle \mathrm{PI} \rangle \gtrsim 0.5$ and $\langle \phi \rangle \approx 80°$, indicating the fibers are nearly parallel to the articular surface. For 100 μm $< z <$ 400 μm, the fiber alignment is much more random with $\langle \mathrm{PI} \rangle \approx 0.3 \pm 0.1$ and the average orientation $\langle \phi \rangle$ showing an overall decrease relative to the tangential zone. For $z >$ 400 μm, there are notable regional differences in $\langle \mathrm{PI} \rangle$, though all samples show a tendency to increase to some mid-range value. For the average fiber orientation in this region, the mean value tends to be centered on $\langle \phi \rangle \approx 70°$, however, as shown in Fig. 4.3(B) in the main text, the standard deviation of $\langle \phi \rangle$ in this region is much higher than the

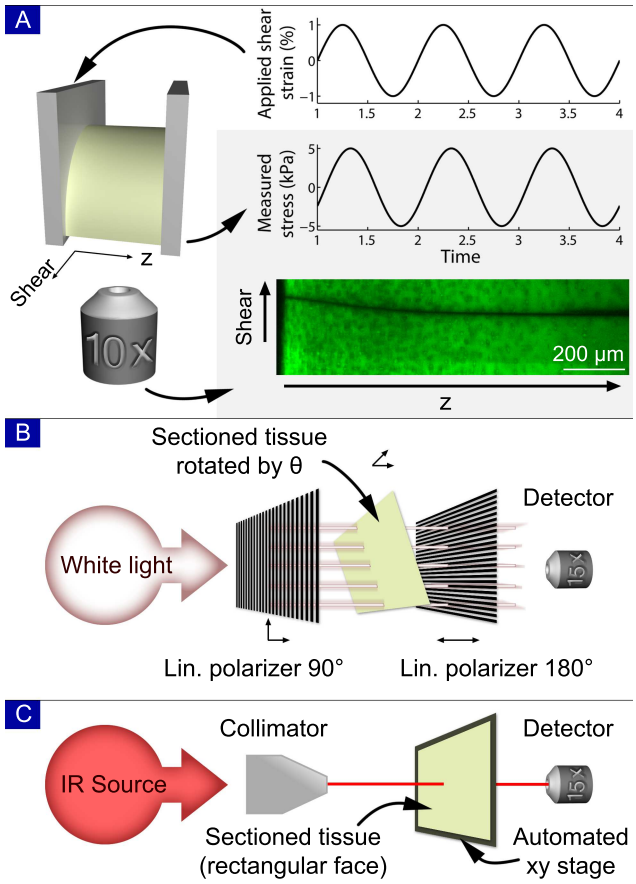

Figure 4.7: Schematic diagrams of the experimental methods used in this study including (A) confocal elastography, (B) quantitative polarized light microscopy, and (C) Fourier transform infrared imaging. Details are provided in the main text.

region where $z < 100\,\mu$m. Thus, when interpreting the mean fiber orientation, it must be realized that this data does not necessarily imply that the fibers are all aligned parallel to the articular surface. Rather, each depth-dependent measurement of $\langle\phi\rangle$ must be interpreted in context of the corresponding measurement of $\langle$PI$\rangle$ to get a per-sample interpretation of how broadly distributed the collagen fiber orientation is about its mean angle.

In adult articular cartilage, the tangential, mid, and deep zones are generally identifiable by the mean fiber orientation (see Fig. 1 in main text). However, in

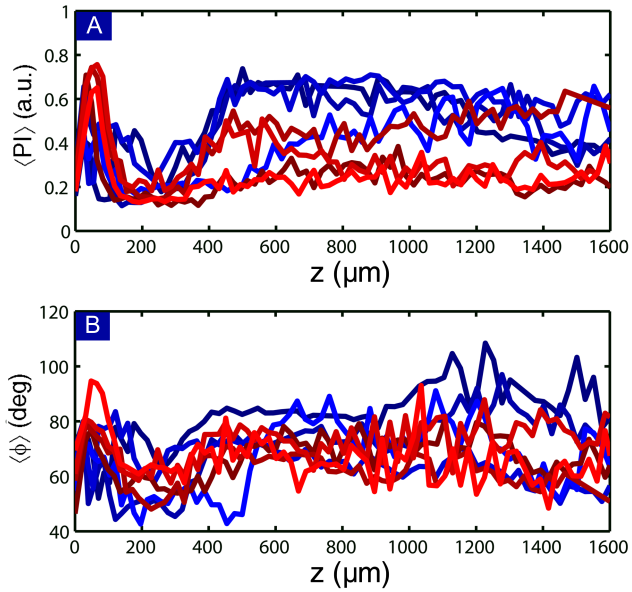

Figure 4.8: Data for every sample's (A) $\langle \mathrm{PI}(z) \rangle$ and (B) $\langle \phi(z) \rangle$ illustrating sample-to-sample variation. The region where $z < 100$ μm corresponds to the tangential zone. Red and blue coloring is coordinated to match Fig. 4.8 in the main text.

immature tissue, this pattern of fiber alignment hasn't fully developed. Thus, in our samples, we only observe a clear tangential zone ($z < 100$ μm), with no clear distinction between the mid and deep zones. This is consistent with earlier QPLM studies on immature porcine AC that observed age-dependent differences in the collagen fiber architecture[17].

4.8.5 Depth-dependent matrix data

FTIR-I data was used to generate depth-dependent measurements of the collagen $v_c(z)$ and aggrecan $v_a(z)$ matrix volume fractions. In this analysis, the total AC spectra for each sample at each depth were decomposed into a linear combination of pure compound spectra and a baseline. Essentially, we have:

$$\text{AC spectra} = c_1\times(\text{Pure type II collagen spectra}) + c_2\times(\text{Pure aggrecan spectra}) + [c_3\times(\text{wavenumber}) + c_4].$$

Here, $c_1 \propto v_c$ and $c_2 \propto v_a$, while c_3 and c_4 are coefficients that determine the baseline associated with instrument-specific deviations and drift. This approach, which is similar to a 2 component principle component analysis, minimizes the difference between the left and right hand sides by varying the 4 coefficients. The best fit values and their 95% confidence intervals are then used to determine matrix volume fractions. Though coarse in many respects, this approach to FTIR-I data analysis is sufficient for our purposes. Indeed, there are a variety of methods available for FTIR-I data analysis that are more sensitive, though it remains an open question as to what approach is best[18, 19, 20, 21, 22, 23, 24, 25, 26, 27].

Here, we show a general and more coarse quantitative data analysis that reproduces the reported correlations, indicating our main result from the FTIR-I measurements – that the shear modulus is strongly correlated with the matrix density – remains valid independent of the specific method used to determine collagen and aggrecan volume fractions. In this approach, we integrate the full IR spectra from 910 to 1726 cm^{-1} at each depth to determine the total amount of absorbance in the region of interest. According to Beer's law[28], this integrated absorbance serves as a measure proportional to solid matrix density. Plotting against the shear modulus in the same manner discussed in the main text again reveals a strong correlation (Fig. 4.9; $R = 0.85,\ p < 0.01$), and shows a 2-fold variation in matrix density is accompanied by a 100-fold variation in shear modulus. This method of analysis does not distinguish between collagen and aggrecan contributions, nor is it scaled to match experimentally measured

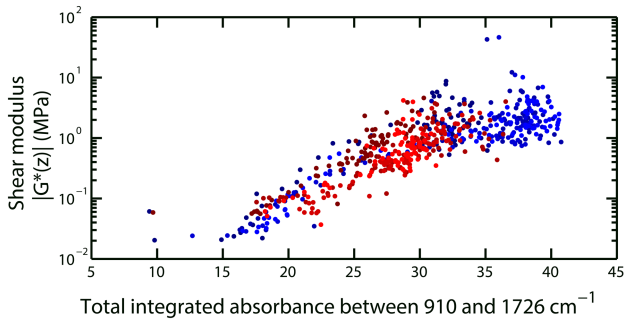

Figure 4.9: Plotting same-sample measurements of the depth-dependent shear modulus against the total integrated absorbance from FTIR measurements reveals a strong correlation between $|G^*(z)|$ and matrix density. Red and blue coloring is coordinated to match Fig. 4.2 in the main text.

volume fraction values. However, our argument in the main text that collagen fibers, and not the aggrecan matrix, are the most likely source for AC's depth-dependent shear properties remains valid.

In the main text only one specific depth-dependent FTIR measurement was shown. Here, we present all measurements (Fig. 4.10(A)). One possible source for spatial variations in matrix volume fraction are artifacts arising from sample preparation; if tissue samples were sectioned in a manner that caused spatial variations in thickness, we would find an enhanced absorbance and consequently a spatial variation in the matrix concentration. Since the in-plane sample orientation was random during the sectioning process, all sectioning cuts were made from different directions. Thus, we can check for this possible artifact by exmaining the ratio of $v_a(z)/v_c(z)$ (Fig. 4.8(B)). For each sample, we find a consistient depth-dependent profile where the surface region ($z < 200$ μm) has an overall increase relative to deeper tissue. This trend can be made more explicit by normalizing the ratio $v_a(z)/v_c(z)$ by each contour's average value for $z > 600$ μm (Fig. 4.8(C)). If sectioning artifacts were present, we would expect

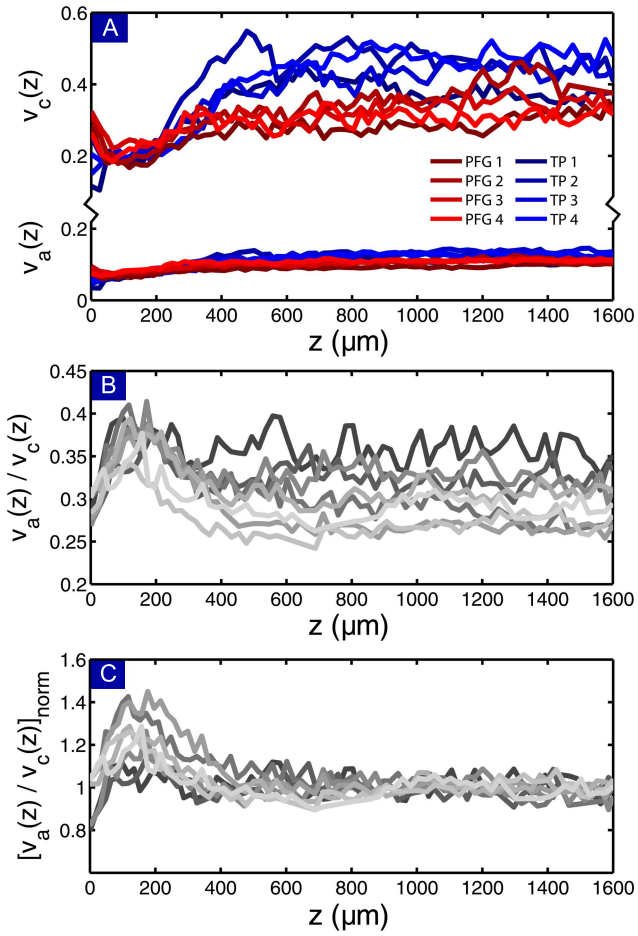

Figure 4.10: (A) We show the depth-dependent aggrecan and collagen volume fractions $v_a(z)$ and $v_c(z)$ for all 8 samples. Note the break in the vertical scale. Red and blue coloring is coordinated to match Fig. 2 in the main text. (B) The ratio of $v_a(z)/v_c(z)$ is plotted as a function of depth to investigate the possibility that depth-dependent variations in matrix volume fraction arise from sample preparation artifacts. (C) Normalizing each $v_a(z)/v_c(z)$ curve by its average value for $z > 600$ μm collapses the curves on to a single master curve that, within noise, is consistent across all samples. This indicates sectioning artifacts are not present in the system.

random deviations from the overall trend, however, within noise, we observe a consistent behavior for all samples indicating variations in tissue thickness do not drive the depth-dependent variations in $v_a(z)$ and $v_(z)$.

4.8.6 Phenomenological fits

From a phenomenological continuum mechanics perspective, we quantified the relation between matrix concentration and shear modulus by fitting $v_a(z)$ and $v_c(z)$ to $|G^*(z)|$ with the expressions $A_a[v_a(z)]^{p_a}$ and $A_c[v_c(z)]^{p_c}$. In Fig. 4.11 we show an example best fit for sample PFG 1, as well as the aggregate results for all 8 samples. Consistent with the power-law nature of these expressions and scatter in the data, the exponents p_a and p_c were found to have relatively small 95% confidence intervals, while the coefficients A_a and A_c did not. Averaging the exponents, we find $\bar{p}_a = 5.6 \pm 0.5$ and $\bar{p}_c = 4.6 \pm 0.8$, both of which are anomalously larger than the typical constitutive relationships used to describe homogeneous media. Note that this method is distinct from what was described in the main text where fitting between shear modulus and collagen volume fraction was performed on all 8 samples aggregated together, whereas this is on a per-sample basis.

4.8.7 Residual analysis of fits

With MATLAB's standard fitting algorithms there is a requirement that the fitting function evaluated over the full domain produces real numbers. However, scatter in experimental data produces data points at v_c lower then values of v_0 that we would reasonably fit for. Consequently, the algorithm evaluates negative numbers raised to non-integer exponents, causing terminal errors. We addressed this issue by inverting the fitting function from $|G^*| = A(v_c - v_0)^{\xi}$ to $v_c = v_0 + (|G^*|/A)^{1/\xi}$, which solved these problems problems. Though a subtle shift in what is typically a straight-forward procedure, this step is necessary in

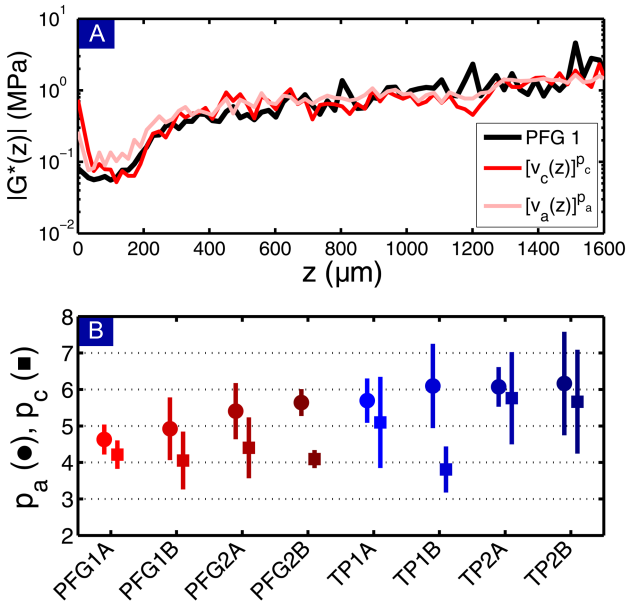

Figure 4.11: (A) Phenomenologically fitting $v_a(z)$ and $v_c(z)$ to $|G^*(z)|$ via a power law results in reasonable agreement between the different data sets, as illustrated here with sample PFG 1. (B) Across all 8 samples, the power law exponents p_a and p_c are found to fall within a limited range, suggesting an anomalously large scaling between the matrix concentration and shear modulus. Red and blue coloring is coordinated to match Fig. 2 in the main text.

order to make use of all available data and not just the points where $v_c > v_0$.

As described in the main text, we found an expression of the form $|G^*| \sim (v_c - v_0)^\xi$ had fits of nearly indistinguishable quality over a range of v_0 from 0.0 to 0.15. In Fig. 4.12 we show the full results of the residual analysis. We find there is a weak maximum at $v_0 \approx 0.07$ but that given the context of how weakly R^2 varies with v_c, this "best fit" can't be used to justify the exponent $\xi = 3.4$ over any other exponent in the range of 2.4 to 4.5.

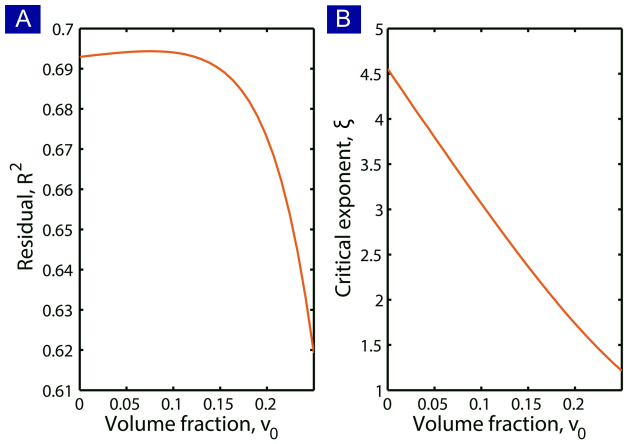

Figure 4.12: (A) The fitting residual R^2 is a measure of how much data variance can be attributed to a particular functional form. For the scaling function used here, we found a range of values for v_0 gave comparable results. (B) The critical exponent ξ associated with a given v_0 varied strongly over a factor of 3.

4.8.8 Loading-condition dependence of model

Because mechanical response depends on loading conditions, we explored the depth-wise compression and shear amplitude dependence of the reinforced fiber network. At 0%, 1%, and 7% compression with a fixed 1% shear amplitude, we found a decrease in the modulus with increasing compression (Fig. 4.13(A)). This behavior is consistent with previous experiments[29], and arises from a shear strain induced relaxation of fiber bending caused by the applied compression. Applying 1%, 4%, and 7% simple shear with 0% compression, we found $G(v_f)$ is insensitive to shear amplitude (Fig. 4.13(B)). This is because the energy density in the linear elastic approximation scales as the strain squared, while $G(v_f)$ in the same approximation scales as the energy density divided by strain squared[30]. Experiments however, show a shear stiffening response as the shear amplitude increases[29]. Evidently, higher-order terms must be included in the energy expression to account for all the loading condition depen-

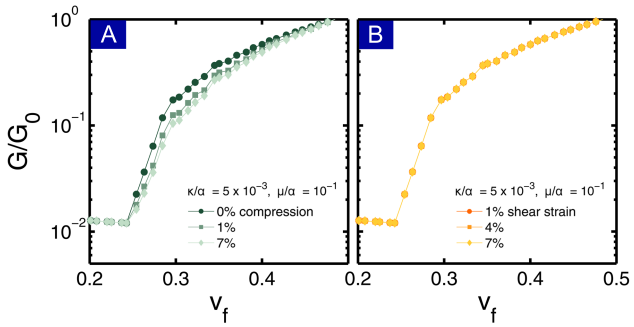

Figure 4.13: To understand the percolating fiber networks loading-condition dependence, we varied (A) the axial compression at fixed shear strain, and (B) the shear strain amplitude at fixed compression. The model exhibits a compression-induced softening in the shear modulus, but is independent of the strain amplitude.

dent behavior.

4.8.9 Spatially heterogeneous lattices

As described in the main text, we used experimentally measured collagen volume fraction data to explore the implications of spatially heterogeneous random kagome lattices. Here, we show an example of what one of these depth-dependent structures looks like (Fig. 4.14).

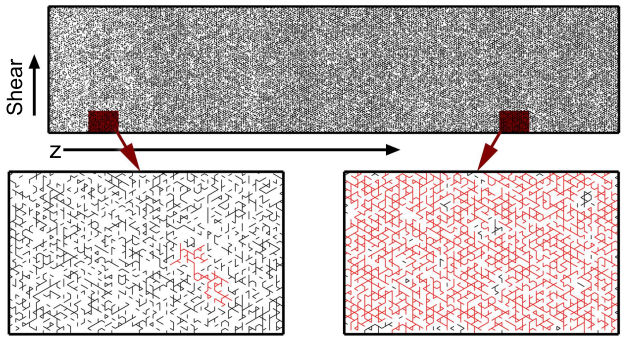

Figure 4.14: Using wet volume fraction data from sample PFG 1, we generated a kagome lattice that is random and isotropic along the direction of shear, but has a varying density of bonds along the z axis. Zoomed insets show the region near the articular surface is below the percolation threshold, while the region at greater z is more well connected.

REFERENCES

[1] V. C. Mow, A. Ratcliffe, and A. R. Poole. Cartilage and diarthrodial joints as paradigms for hierarchical materials and structures. *Biomaterials*, 13:67–97, 1992. DOI: 10.1016/0142-9612(92)90001-5.

[2] S Cowin and S Doty. *Tissue mechanics*. Springer Science, New York, 1st edition, 2007.

[3] P. Julkunen, P. Kiviranta, W. Wilson, J. S. Jurvelin, and R. K. Korhonen. Characterization of articular cartilage by combining microscopic analysis with a fibril-reinforced finite-element model. *J. biomech.*, 40:1862–1870, 2007. DOI: 10.1016/j.jbiomech.2006.07.026.

[4] P. Julkunen, W. Wilson, J. S. Jurvelin, J. Rieppo, C.-J. Qu, M. J. Lammi, and R. K. Korhonen. Stress relaxation of human patellar articular cartilage in unconfined compression: prediction of mechanical response by tissue composition and structure. *J. Biomech.*, 44:1978–1986, 2008. DOI: 10.1016/j.jbiomech.2008.03.026.

[5] L. Rieppo, S. Saarakkala, J. S. Jurvelin, and J. Rieppo. Prediction of compressive stiffness of articular cartilage using Fourier transform infrared spectroscopy. *J. Biomech.*, 44:1269–1275, 2013. DOI: 10.1016/j.jbiomech.2013.02.022.

[6] L. P. Rasanen, M. E. Mononen, M. T. Nieminen, E. Lammentausta, J. S. Jurvelin, R. K. Korhonen, and OAI-Investigators. Implementation of subject-specific collagen architecture of cartilage into a 2D computational model of a knee joint – Data from the Osteoarthritis Initiative (OAI). *J. Orthop. Res.*, 31:10–22, 2013. DOI: 10.1002/jor.22175.

[7] K. S. Halonen, M. E. Mononen, J. S. Jurvelin, J. Toyras, and R. K. Korhonen. Importance of depth-wise distribution of collagen and proteoglycans in articular cartilage – A 3D finite element study of stresses and strains in human knee joint. *J. biomech.*, 46:1184–1192, 2013. DOI: 10.1016/j.jbiomech.2012.12.025.

[8] V. C. Mow, S. C. Kuei, W. M. Lai, and C. G. Armstrong. Biphasic creep and stress relaxation of articular cartilage in compression: Theory and experiments. *J. Biomech. Eng.*, 102:73–84, 1980. DOI: 10.1115/1.3138202.

[9] V. C. Mow, M. H. Holmes, and W. M. Lai. Fluid transport and mechanical properties of articular cartilage: A review. *J. Biomech.*, 17:377–394, 1984. DOI: 10.1016/0021-9290(84)90031-9.

[10] W. M. Lai, J. S. Hou, and V. C. Mow. A triphasic theory for the swelling and deformation behaviors of articular cartilage. *J. Biomech. Eng.*, 113:245–258, 1991. DOI: 10.1115/1.2894880.

[11] A. K. Williamson, A. C. Chen, and R. L. Sah. Compressive properties and function-composition relationships of developing bovine articular cartilage. *J. Orthop. Res.*, 19:1113–1121, 2001. DOI: 10.1016/S0736-0266(01)00052-3.

[12] Robert M Schinagl, Michael K Ting, Jeffrey H Price, and Robert L Sah. Video microscopy to quantitate the inhomogeneous equilibrium strain within articular cartilage during confined compression. *Annals of biomedical engineering*, 24(4):500–512, 1996.

[13] Robert M Schinagl, Donnell Gurskis, Albert C Chen, and Robert L Sah. Depth-dependent confined compression modulus of full-thickness bovine articular cartilage. *Journal of orthopaedic research*, 15(4):499–506, 1997.

[14] Nadeen O Chahine, Christopher CB Wang, Clark T Hung, and Gerard A Ateshian. Anisotropic strain-dependent material properties of bovine articular cartilage in the transitional range from tension to compression. *Journal of biomechanics*, 37(8):1251–1261, 2004.

[15] Janice H Lai and Marc E Levenston. Meniscus and cartilage exhibit distinct intra-tissue strain distributions under unconfined compression. *Osteoarthritis and cartilage*, 18(10):1291–1299, 2010.

[16] W. G. Ellenbroek, Z. Zeravcic, W. van Saarloos, and M. van Hecke. Non-affine response: jammed packings vs. spring networks. *Epl*, 87:34004–1, 2009. DOI: 10.1209/0295-5075/87/34004.

[17] J. Rieppo, J. Hallikainen, J. Jurvelin, I. Kiviranta, H. J. Helminen, and M. M. Hyttinen. Practical considerations in the use of polarized light microscopy in the analysis of the collagen network in articular cartilage. *Microsc. Res. Techniq.*, 71:279–287, 2008. DOI: 10.1002/jemt.20551.

[18] L. Rieppo, J. Rieppo, J. S. Jurvelin, and S. Saarakkala. Fourier transform infrared spectroscopic imaging and multivariate regression for prediction of proteoglycan content of articular cartilage. *PLoS ONE*, 7:1–8, 2012. DOI: 10.1371/journal.pone.0023244.

[19] N. P. Camacho, P. West, P. A. Torzilli, and R. Mendelsohn. FTIR microscopic imaging of collagen and proteoglycan in bovine cartilage. *Biopolymers*, 62:1–8, 2000.

[20] X. Bi, G. Li, S. B. Doty, and N. P. Camacho. A novel method for determination of collagen orientation in cartilage by Fourier transform infrared imaging spectroscopy FT-IRIS. *Osteoarthr. Cartilage*, 13:1050–1058, 2005. DOI: 10.1016/j.joca.2005.07.008.

[21] X. Bi, X. Yang, M. P. G. Bostrom, and N. P. Camacho. Fourier transform infrared imaging spectroscopy investigation in the pathogenesis and repair of cartilage. *Biochim. Biophys. Acta*, 1758:934–941, 2006. DOI: 10.1016/j.bbamem.2006.05.014.

[22] Y. Xia, N. Ramakrishnan, and A. Bidthanapally. The depth-dependent anisotropy of articular cartilage by Fourier-transform infrared imaging (FTIR). *Osteoarthr. Cartilage*, 15:780–788, 2007. DOI: 10.1016/j.joca.2007.01.007.

[23] L. Rieppo, S. Saarakkala, T. Narhi, J. Holopainen, M. Lammi, H. J. Helminen, J. S. Jurvelin, and J. Rieppo. Quantitative analysis of spatial proteoglycan content in articular cartilage with Fourier transform infrared imaging spectroscopy: Critical evaluation of analysis methods and specificity of the parameters. *Microsc. Res. Techniq.*, 73:503–512, 2010. DOI: 10.1002/jemt.20789.

[24] J. Yin and Y. Xia. Macromolecular concentrations in bovine nasal cartilage by Fourier transform infrared imaging and principle component regression. *Appl. Spectrosc.*, 64:1199–1208, 2010. DOI: 10.1366/000370210793335124.

[25] J. Yin, Y. Xia, and M. Lu. Concentration profiles of collagen and proteoglycan in articular cartilage by Fourier transform infrared imaging and principal component regression. *Spectrochim Acta A-M*, 88:90–96, 2012. DOI: 10.1016/j.saa.2011.12.002.

[26] Y. Xia, D. Mittelstaedt, N. Ramakrishnan, M. Szarko, and A. Bidthanapally. Depth-dependent anisotropies of amides and sugar in perpendicular and parallel sections of articular cartilage by Fourier transform in-

frared imaging. *Microsc. Res. Techniq.*, 74:122–132, 2011. DOI: 10.1002/jemt.20881.

[27] Y. Xia, H. Alhadlaq, N. Ramakrishnan, A. Bidthanapally, F. Badar, and M. Lu. Molecular and morphological adaptations in compressed articular cartilage by polarized light microscopy and Fourier-transform infrared imaging. *J. Struct. Biol.*, 164:88–95, 2008. DOI: 10.1016/j.jsb.2008.06.009.

[28] Brian Smith. *Fundamentals of fourier transform infrared spectroscopy*. CRC Press, Boca Raton, 1st edition, 2006.

[29] M. R. Buckley, A. J. Bergou, J. Fouchard, L. J. Bonassar, and I. Cohen. High-resolution spatial mapping of shear properties in cartilage. *J. Biomech.*, 43:796–800, 2010. DOI: 10.1016/j.jbiomech.2009.10.012.

[30] D. A. Head, A. J. Levine, and F. C. MacKintosh. Deformation of cross-linked semiflexible polymer networks. *Phys. rev. lett.*, 91:108102–1, 2003. DOI: 10.1103/PhysRevLett.91.108102.

CHAPTER 5

USING ORIGAMI DESIGN PRINCIPLES TO FOLD REPROGRAMMABLE MECHANICAL METAMATERIALS

Jesse L. Silverberg, Arthur A. Evans, Lauren McLeod, Chris D. Santangelo, Thomas Hull, and Itai Cohen, *under review*.

5.1 Abstract

While typically recognized for its aesthetic value, the origami art form is currently being explored as a framework for mechanical metamaterial design. In such origami-inspired structures, the bulk elastic properties are controlled by the underlying pattern of creases and the angles at which they are folded. By exploiting the possibility of multiple stable folding configurations, we show how a tessellated pattern known as the Miura-ori can have its compressive moduli rationally and reversibly tuned by orders of magnitude. This variability is achieved by switching individual unit cells between bistable states, introducing defects in the otherwise regular lattice topology. Furthermore, we find defects can interact, giving rise to emergent crystallographic structures such as lattice vacancies, dislocations, and grain boundaries. Each of these structures comes from a specific spatial pattern of reversible folds, highlighting the unique connection origami-inspired design makes between mechanical metamaterials and programmable matter.

5.2 Main Text

Owing to their exotic and tunable material properties, metamaterials are quickly emerging at the frontier of scientific and technological innovation[1, 2, 3, 4, 5]. The key insight driving these systems enters at the design stage, where an arrangement of smaller units is used to engineer bulk properties. Once fabricated, structural modifications are generally difficult, making it rare to find metamaterials that can be reconfigured beyond the original design. Origami-inspired mechanical metamaterials offer enhanced flexibility in performance because their properties are coupled to a dynamically alterable folding pattern[6, 7, 8, 9, 10, 11, 12, 13, 14, 15, 16]. Hence, multiple stable configurations can manifest from a single structure, ultimately leading to *programmable metamaterials*. In this work, we show that the transformational ability of a unit cell in origami-based metamaterials leads to a range of mechanical properties, and moreover, interactions of these programmable elements exhibit emergent properties equivalent to crystallographic defects in atomic systems.

We study the Miura-ori tessellated folding pattern, which has recently been proposed as an origami metamaterial (Fig. 5.1(A-C), SI Movie 1)[14, 15]. Historically, this design was invented to efficiently pack solar panels for space missions[17], but the morphology also naturally occurs in leaves[18], embryonic intestine[19, 20], and generally arises under biaxial compression of thin sheets tethered to a surface. The geometry of an ideal Miura-ori is a herringbone pattern that emerges from a series of convex mountain and concave valley creases (Fig. 5.1(C)). When three mountains and one valley, or three valleys and one mountain intersect, a vertex is formed. Four adjacent vertices bound equal area facets arranged with inversion symmetry (Fig. 5.1(B)). This fold pattern defines

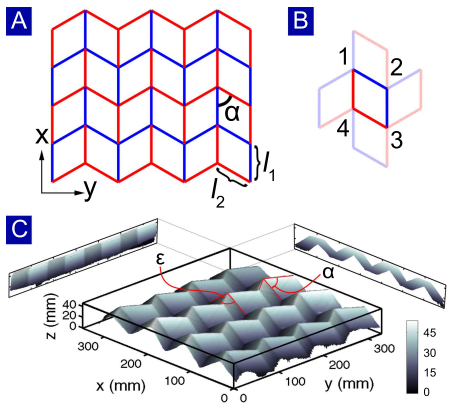

Figure 5.1: (A) The crease pattern for a Miura-ori on a flat sheet is depicted with alternating mountain (red) and valley (blue) folds whose geometry is set by the facet lengths ℓ_1, ℓ_2 and the angle between folds α. (B) Each facet is bounded by 4 vertices labeled 1 through 4. (C) A 3D image of a 4×4 Miura-ori with two in-plane projections at equilibrium illustrates the folded structure. Color bar gives height in mm.

a lattice characterized by two static lengths ℓ_1, ℓ_2, and one static angle α. To quantify folding, a vertex angle ε is required (Fig. 5.1(C)); when $\varepsilon = 180^\circ - 2\alpha$ the structure is contracted into a folded state, and when $\varepsilon = 180^\circ$ the structure is an extended flat sheet.

If folded from material with infinite stretching modulus, a Miura-ori tessellation would have only one degree of freedom described by ε[14]. However, when folded from real materials, the Miura-ori exhibits additional degrees of freedom as evidenced by soft bending modes[14, 15]. As an extreme example, the Miura-ori supports highly localized heterogeneity introduced post-folding by applying force to a vertex in the normal direction, and popping it into a distinctly different state (Fig. 5.2(A-D), SI Movie 2). This pop-through defect (PTD) acts to change the lattice topology by suppressing one fold and bending adjacent facets through an angle ϕ, as illustrated by a mean curvature map of the surface (Fig. 5.2(A-D), SI) [21]. Thus, unlike conventional lattice defects, PTDs

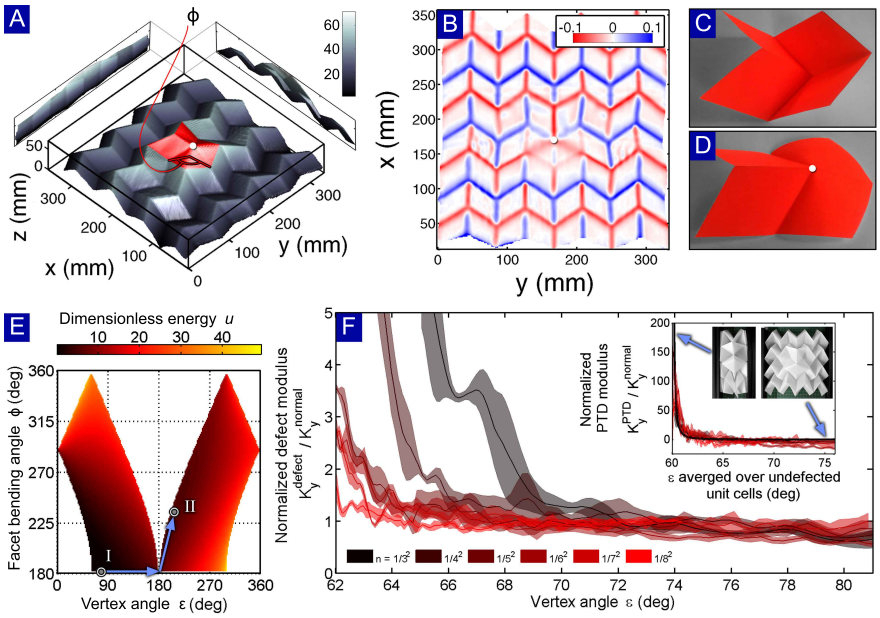

Figure 5.2: (A) A 3D image of a 4×4 Miura-ori with a centrally located pop-through defect (PTD, red facets). Color bar gives height in mm. (B) Spatial map of the mean curvature shows changes in the crease network due to the PTD centered on the white circle. Naive counting of creases at each vertex shows a PTD generates a lattice with four disclinations. Color bar is in units of mm^{-1}. (C) Photograph of a single vertex shows it is stable independent of the connected lattice, (D) as is an isolated PTD. (E) Energy diagram of a single vertex shows two energy minima corresponding to two mechanically stable states: I) a standard vertex, and II) a PTD. Arrows show the most direct pathway to form a PTD from a defect-free vertex without stretching. White background is geometrically-forbidden. (F) Normalized compressive modulus of a lattice with a PTD as a function of compression illustrates the sensitivity to defect density n. (Inset) These data follow a scaling collapse.

can be reversibly removed because these deformations are elastic.

To determine the robustness of PTDs to mechanical perturbations, we theoretically model a single unit cell with one mountain and three valley folds in mechanical equilibrium (e.g. Fig. 5.2(C)). To account for experimentally observed facet bending, two additional symmetrically-placed creases are included whose

folding angles ϕ are equal and have equilibrium values of 180° [14, 15]. We assume a Hookean energy expression for all creases and calculate the dimensionless energy u as a function of the folding configuration (Fig. 5.2(E), SI). We observe the energy landscape has two distinct regions, each with their own local minimum (Fig. 5.2(E) points I and II), that are connected at a single point corresponding to a fully unfolded unit cell (Fig. 5.2(E), $\phi = \varepsilon = 180°$). For materials with finite stretching modulus, this connecting point widens along the ϕ axis and allows for otherwise forbidden stretching-enabled transitions. Because the stretching modulus is proportional to sheet thickness[22], the energy required to transition between states is a tunable design feature. Thus, while PTDs are introduced reversibly, their stability to mechanical perturbations is tuned by the underlying material properties.

The mechanical consequences of a PTD were determined by folding structures with s^2 unit cells where s was varied from 3 to 8 and α was fixed at 60°. A centrally located defect was introduced and the compressive modulus $K_y^{\text{defect}}(\varepsilon)$ was measured as a function of defect density $n = 1/s^2$ (SI). Normalizing these data by the modulus of a defect-free lattice (SI), $K_y^{\text{normal}}(\varepsilon)$, revealed a divergence in stiffness as a function of compression limited only by tearing of the sheet (Fig. 5.2(F)). This divergence results from a violation of Maekawa's theorem, which requires the number of mountain folds minus the number of valley folds emanating from every vertex to be ±2 for a structure to fold flat (Fig. 5.2(B))[23]. By linking enhanced mechanical stiffness to violations of a canonical paper-folding theorem, this data experimentally demonstrates how geometric constraints in origami-based design can dominate bulk material properties. Nevertheless, such constraints are still malleable; the value of ε where K_y^{defect} increases is shifted simply by varying n. Thus, PTDs make attractive elements for meta-

material design because the onset and strength of K_y^{defect} are rationally tunable, and moreover, these "mechanical pixels" can be activated on-demand to vary the bulk compressive properties.

To understand both the density- and compression-dependence of a Miura-ori with a PTD, we analytically calculated the intrinsic PTD compressive modulus, K_y^{PTD}. This was found by noting the stress a PTD exerts is proportional to its extension relative to the neighboring undefected unit cells (SI). At low defect densities, the compressive modulus of a lattice with a PTD can be expressed in a dipole expansion, $K_y^{\text{defect}} = K_y^{\text{normal}} + nK_y^{\text{PTD}}$, where K_y^{PTD} is a function of ε averaged over the non-defected unit cells. This calculation suggests a data collapse with a one-parameter fit to the theory that simply sets the scale of K_y^{PTD}. Indeed, we find such a collapse (Fig. 5.2(F) inset) and excellent agreement with the analytic expression (Fig. 5.2(F) inset, black line), demonstrating the contribution of PTDs to the modulus at low densities is linearly additive. This mechanical response is useful for design purposes because it offers great simplicity in predicting the compressive modulus of a Miura-ori with PTDs.

With increasing density, PTD interactions become important, particularly when pairs of defects are on adjacent vertices. There are 4 unique defect pairs: $1-2$, $1-3$, $1-4$, and $2-4$, with the other combinations degenerate by symmetry (Fig. 5.1(B); Fig. 5.3(A-D)). Folding 4×4 lattices with $\alpha = 60°$, we measured $K_y^{\text{defect}}(\varepsilon)$ in the presence of the four unique defect pair configurations. Normalizing by the defect-free modulus, we found the $1-2$, $1-3$, and $1-4$ defect pair moduli diverge as the compression increases (Fig. 5.3(E), SI Movie 3). Compared to a lattice with a single defect at comparable density, the enhanced stiffness tends to occur at higher compressions where ε is approximately $5°$ smaller. Inspecting

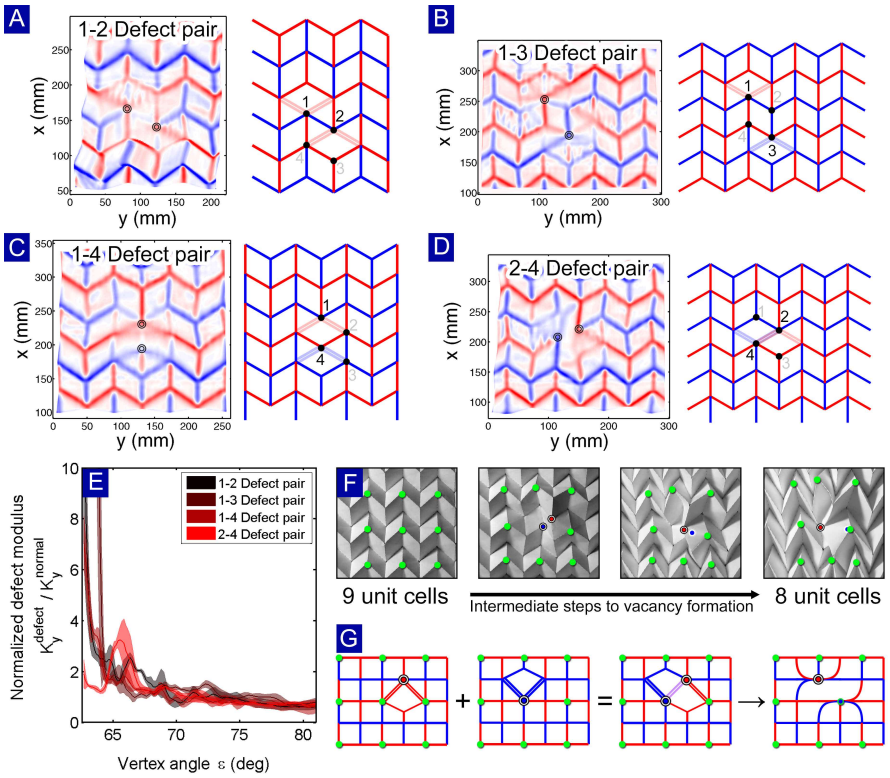

Figure 5.3: Mean curvature maps of a (A) 1-2, (B) 1-3, (C) 1-4, and (D) 2-4 defect pair configuration. Color maps saturate at ±1 mm^{-1}. In each case, the schematic diagram shows defect placement (dots) and facet bending (double lines). (E) Normalized compressive modulus of a lattice with each defect pair configuration shows 3 combinations lead to divergent stiffness, while the 2-4 configuration does not. (F) Labeling 9 unit cells with green dots and examining their location as ε decreases demonstrates how the 2-4 defect configuration (red and blue dots) leads to a lattice vacancy. (G) Schematic diagrams based on previous panel show how and where the 2-4 defect interacts, as well as the resultant crease reassignment that arises from the vacancy.

lattices during compression revealed the difference occurs because these defect-pairs encourage a weak buckling instability normal to the compression plane, lowering the effective value of ε where the modulus diverges.

Surprisingly, the 2 – 4 configuration has qualitatively different compressive behavior: the modulus first *increases* during compression similar to other defect-

pair configurations, but then *decreases*, and finally reduces to a near defect-free value at the highest compressions (Fig. 5.3(E)). Effectively, the respective mechanical signatures of the 2 – 4 defect pair annihilate during compression. To illustrate the associated folding sequence, we mark the centers of a 3×3 sublattice (Fig. 5.3(F) green dots), as well as the location of each defect (Fig. 5.3(F) red and blue dots). During compression, facets near the defect sites are increasingly bent as ε decreases, leading to the enhanced stiffness. This enhancement progresses until the 4 defect site folds under the 2 defect site and all 4 creases on the facet flip. The defect sites then collapse onto, and overlap with, nearby vertices (Fig. 5.3(F)) so that the center lattice site is tucked underneath the adjacent unit cell (SI Movie 4). Visually inspecting the 2 – 4 defect pair reveals a remarkable consequence: this defect configuration generates a *lattice vacancy* analogous to those seen in crystallographic systems.

To understand why the 2 – 4 defect pair is special, we compute the mean curvature from 3D scans (Fig. 5.3(A-D)). Comparing the four cases, we see the 2 – 4 pair is distinguished by overlapping bending facets of equal magnitude but opposite sign, as quantified by the zero mean curvature on the central facet. This cancellation is possible due to the symmetry of the 2 – 4 placement and the reversibility of a PTD's deformation of a Miura-ori lattice, which ultimately yields the lattice vacancy[24]. When fully compressed, the defect-modified crease pattern is compatible with Maekawa's theorem for flat-foldability (Fig. 5.3(G)), and hence the compressive modulus is restored to a nearly defect-free value.

Recognizing the 2-4 defect pair as a lattice vacancy immediately suggests the Miura-ori supports other types of crystallographic defects[22]. For example, a column of vacancies form an edge dislocation (Fig. 5.4(A)), and several

adjacent edge dislocations form a grain boundary (Fig. 5.4(B)). In both cases, these reconfigurations of the lattice are flat-foldable. Similarly, arrangements of non-interacting PTDs can generate non-flat-foldable grain boundaries: a column of the PTDs popped in the same direction creates a hinge-like boundary that induces a net curvature in the overall structure (Fig. 5.4(C,D)), while a series of PTDs in alternating directions resists deformations and remains planar (Fig. 5.4(E,F)). Collectively, these observations suggest each PTD carries a charge-like quantity, that when summed over the lattice, determines the macroscopic curvature of the Miura-ori.

Rationally introducing patterns of defects as design elements swiftly generates a vast library of origami-inspired mechanical metamaterials. The ability to place these features without permanently altering the crease pattern is a key advantage that allows one to dynamically reprogram elastic properties. Thus, by linking metamaterials with programmable matter[25], origami design principles are uniquely positioned to make exceptional contributions to the next generation of materials.

5.3 Acknowledgments

The authors thank R. J. Lang, B. Johnson, B. Parker, and M. Schneider for artistic inspiration, as well as R. Hayward, N. Bende, J. Na, M. Byun, and the Cohen lab for useful discussions. We also thank F. Parish for assistance with the laser cutter, as well as X. Cheng, N. Lin, and B. Leahy for their design and construction efforts on the 3D laser scanner hardware. This work was funded by the National Science Foundation through award EFRI ODISSEI-1240441 and the GRFP, which

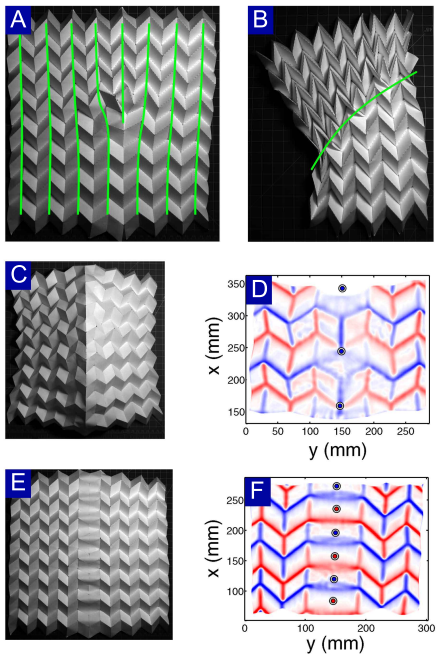

Figure 5.4: (A) Introducing PTDs to generate a column of lattice vacancies produces an edge dislocation. (B) Columns of side-by-side edge dislocations generate a grain boundary. (C) A column of PTDs with the same orientation results in a hinge-like boundary that runs vertically through the structure. (D) Mean curvature map illustrates the net curvature of the non-flat-foldable structure from the previous panel, as indicated by the excess of mountain creases. (E) A column of PTDs with alternating orientation results in a rigid boundary. (F) Mean curvature map illustrates the zero net curvature of the non-flat-foldable structure from the previous panel, as indicated by the equal number of mountain and valley creases. Because PTDs can be reversibly introduced and removed, a single lattice is capable of being reprogrammed into any configuration shown here.

funded J.L.S..

REFERENCES

[1] Martin Wegener. Metamaterials beyond optics. *Science*, 342:939–940, 2013.

[2] Yongmin Liu and Xiang Zhang. Metamaterials: a new frontier of science and technology. *Chem. soc. rev.*, 40:2494–2507, 2011.

[3] Jae-Hwang Lee, Jonathan P. Singer, and Edwin L. Thomas. Micro-/nanostructured mechanical metamaterials. *Adv. mater.*, 24:4782–4810, 2012.

[4] A. Q. Liu, W. M. Zhu, D. P Tsai, and N. I. Zheludev. Micromachined tunable metamaterials: a review. *J. opt.*, 14:114009–1, 2012.

[5] Muamer Kadic, Tiemo Buckmann, Robert Schittny, and Martin Wegener. Metamaterials beyond electromagnetism. *Rep. prog. phys.*, 76:126501–1, 2013.

[6] Charlotte Py, Paul Reverdy, Lionel Doppler, Jose Bico, Benoit Roman, and Charles N. Baroud. Capillary origami: spontaneous wrapping of a droplet with an elastic sheet. *Phys. rev. lett.*, 98:156103–1, 2007. DOI: 10.1103/PhysRevLett.98.156103.

[7] Alessandro Papa and Sergio Pellegrino. Systematically creased thin-film membrane structures. *J. space rockets*, 45:10–18, 2008. DOI: 10.2514/1.18285.

[8] Noy Bassik, George M. Sten, and David H. Gracias. Microassembly based on hands free origami with bidirectional curvature. *Appl. phys. lett.*, 95:091901–1, 2009. DOI: 10.1063/1.3212896.

[9] Jungwook Kim, James A. Hanna, Myunghwan Byun, Christian D. Santangelo, and Ryan C. Hayward. Designing responsive buckled surfaces by halftone gel lithography. *Science*, 335:1201–1205, 2012. DOI: 10.1126/science.1215309.

[10] Jungwook Kim, James A. Hanna, Ryan C. Hayward, and Christian D. Santangelo. Thermally responsive rolling of thing gel strips with discrete variations in swelling. *Soft matter*, 8:2375–2381, 2012. DOI: 10.1039/c2sm06681e.

[11] Marcelo A. Dias, Levi H. Dudte, L. Mahadevan, and Christian D. Santangelo. Geometric mechanics of curved crease origami. *Phys. rev. lett.*, 109:114301–1, 2012. DOI: 10.1103/PhysRevLett.109.114301.

[12] Marcelo A. Dias and Christian D. Santangelo. The shape and mechanics of curved-fold origami structures. *Epl*, 100:54005–p1, 2012. DOI: 10.1209/0295-5075/100/54005.

[13] Jennie Ryu, Matteo D'Amato, Xiaodong Cui, Kevin N. Long, H. Jerry Qi, and Martin L. Dunn. Photo-origami: bending and folding polymers with light. *Appl. phys. lett.*, 100:161908–1, 2012. DOI: 10.1063/1.3700719.

[14] Mark Schenk and Simon D. Guest. Geometry of miura-folded metamaterials. *Proc. natl. acad. sci.*, 110:3276–3281, 2013. DOI: 10.1073/pnas.1217998110.

[15] Z. Y. Wei, Z. V. Guo, L. Dudte, H. Y. Liang, and L. Mahadevan. Geometric mechanics of periodic pleated origami. *Phys. rev. lett.*, 110:215501–1, 2013. DOI: 10.1103/PhysRevLett.110.215501.

[16] Mustapha Jamal, Sachin S. Kadam, Rui Xiao, Faraz Jivan, Tzia-Ming Onn, Rohan Fernandes, Thao D. Nguyen, and David H. Gracias. Bio-

origami hydrogel scaffolds composed of photocrosslinked peg bilayers. *Adv. healthcare mater.*, 2:1142–1150, 2013. DOI: 10.1002/adhm.201200458.

[17] Koryo Miura. Method of packaging and deployment of large membranes in space. *Inst. space astronaut. sci. rep.*, 618:1–9, 1985.

[18] L. Mahadevan and S. Rica. Self-organized origami. *Science*, 307:1740, 2005. DOI: 10.1126/science.1105169.

[19] Martine Ben Amar and Fei Jia. Anisotropic growth shapes intestinal tissues during embryogenesis. *Proc. natl. acad. sci.*, 110:10525–10530, 2013. DOI: 10.1073/pnas.1217391110.

[20] Amy E. Shyer, Tuomas Tallinen, Nandan L. Nerurkar, Zhiyan Wei, Eun Seok Gil, David L. Kaplan, Clifford J. Tabin, and L. Mahadevan. Villification: how the gut gets its villi. *Science*, 342:212–218, 2013.

[21] Timothy D. Gatzke and Cindy M. Grimm. Estimating curvature on triangular meshes. *Int. j. shape model.*, 12:1–28, 2006. DOI: 10.1142/S0218654306000810.

[22] L. D. Landau and E. M. Lifshitz. *Landau and lifshitz course of theoretical physics volume 7: theory of elasticity*. Butterworth Heinemann, New Delhi, 3rd edition, 1986.

[23] Marshall Bern and Barry Hayes. The complexity of flat origami. *Proceedings of the symposium on discrete algorithms*, 7:175–183, 1996.

[24] P. M. Chaikin and T. C. Lubensky. *Principles of condensed matter physics*. Cambridge University Press, United Kingdom, 1st edition, 2000.

[25] Tommaso Toffoli and Norman Margolus. Programmable matter: concepts and realization. *Physica d*, 47:263–272, 1991.

5.4 Supplemental Information

5.4.1 Materials and methods

Sample fabrication

To generate origami samples for mechanical testing, we first performed experiments with hand-folded sheets. While easy to generate, these samples have the disadvantage of including additional "pre-creases" that are not used in the final structure, but nonetheless are necessary to guide crease placement. The presence of pre-creases is problematic as they add additional degrees of freedom to the lattice. Thus, we employed a laser-cutter to pattern only the essential creases into a sheet. Patterns of continuous lines (e.g., similar to Fig. 5.1(A) in main text) were first designed in Adobe Illustrator with a specified ℓ_1, ℓ_2, and α, and then converted to a generic vector format for cutting. At the lowest power settings, the laser scored sheets, creating a joint that is easily folded into a crease. However, scores easily tear and exhibit anisotropic bending properties. Thus, we replaced the continuous line patterns with dash-and-gap perforations. These samples had isotropic creases that exhibited indistinguishable folding stiffness whether mountain or valley.

Geometries were chosen so that $\ell_1 = \ell_2 \equiv \ell = 25.4$ mm. The angle α was varied from 35° to 65° in 5° increments. The number of unit cells was varied according to the experiment. Laser power was set to 45% max output, with a dwell time of 45%. We also varied the material to study 9 to 65 lb paper, 45 to 120 lb cardstock, and 0.001 to 0.003 mm thick mylar. For mechanical testing, we found 24 lb paper was both representative and easiest to work with. For

example, the mechanical behavior reported in the main text concerning PTDs and their interactions was qualitatively consistent across materials, though the compressive moduli magnitude K_y depended on the material used.

Laser scanner

To study the 3 dimensional (3D) structure of the Miura-ori, we constructed a custom laser scanner. This apparatus consisted of a laser sheet light source and digital camera that were mounted a fixed distance apart, but able to translate vertically along a guided rail track. The laser/camera mount was driven by a digitally controlled electric motor and set to translate at a fixed rate. For each scan, an origami structure was oriented in front of the apparatus to prevent and/or minimize self-shadowing. The laser/camera was then translated vertically, and video was acquired from the camera at 7.5 frames per second in an otherwise unlit room. Experimenting with various materials, we found opaque mylar provided high-quality reconstructions due to the light scattering properties of its surface. 24 lbs paper, which was used for mechanical testing, was significantly more reflective and generated numerous imaging artifacts that were not easily corrected for. Nevertheless, comparing Mylar and paper scan data revealed mutually consistent 3D structure.

Optical aberrations from a camera's lens produces distortion of 2D images. To correct for this, camera calibration software written for MATLAB (Camera Calibration Toolbox, J.-Y. Bouguet) was used in conjunction with a 3×4 ft^2 checkerboard pattern to generate a lens-specific correction factor. These correction factors were applied to the raw camera data, prior to the 3D reconstruction in MATLAB. To generate 3D topographic maps, our custom code tracks the re-

flected laser sheet light and uses the known apparatus geometry to calculate surface topography in a given plane. Translating the laser/camera plane then provides a 3D map of the origami surface with a voxel resolution of 0.4×0.4×0.96 mm^3.

With the surface digitized and reconstructed, we were able to locally measure the curvature[1] using a polynomial approximation method[2]. In this approach, a local patch of the measured surface approximately $\ell/10 \times \ell/10$ in size was selected. These dimensions were chosen as they were found to smooth noise associated with the discreteness of the surface, while optimizing spatial resolution. The patch was then fit to a polynomial of the form $z^2 = (x/a)^2 + (y/b)^2$, where the coordinate system for the fit coincides with the center of the patch. From the the best-fit values of a and b, the patch-averaged mean and Gaussian curvature were calculated and assigned to the patch center. This procedure was iterated as the patch center point was rastered over the entire xy surface at pixel resolution. Spatial maps of the Gaussian curvature were found to be indistinguishable from noise, while maps of the mean curvature had well-pronounced effects consistent with visual inspection of the original lattice.

Compression Stage

A custom built compression stage was developed to measure the mechanical properties of origami structures. This consisted of two smoothly polished aluminum compression plates, one mounted to a Haydon-Kerk linear translation stage (PCM4826X-K IDEA stepper motor), and the other to a Loadstar force measurement sensor (3 kg RSP1 load cell with DI-1000U interface). In a typical experiment, the compression plate separation and load cell force data was

simultaneously recorded by a single custom MATLAB program. Smooth lucite panels were mounted underneath the compression plates to provide a low-friction surface for the origami structures to move on during compression. To further reduce friction, one side of the lattice was slightly elevated with a small piece of adhesive tape that simultaneously served to reduce contact area with the lucite panels, while also leaving the folded structure able to freely deform during compression.

To determine the origami lattice compressive modulus, a compression routine was developed that operated in the following manner. Initially, the plate separation was set to a value slightly larger ($\approx 5\%$) than the width of the origami lattice (Fig. 5.5, point 1). The compression cycle began, and the lattice was compressed 6.35 mm, during which the load and plate separation were recorded. The system paused for two seconds at the maximum compression (Fig. 5.5, point 2), reversed direction, and returned the plates to their initial separation. During decompression, the compression plate lost contact with the origami lattice (Fig. 5.5, point 3). After one compression cycle, we found the origami lattice width was reduced compared to its original state (Fig. 5.5, compare points 1 and 4), indicating plastic deformation of the mountain and valley creases. The load-unload cycle was repeated 8 times. When the load-displacement curves were superimposed, we found the first cycle was noticeably different from the remaining cycles, while the rest were nearly indistinguishable (Fig. 5.5, red lines show runs 2 through 8). We then averaged the load-displacement data for runs 3 through 8 producing a single load-displacement curve associated with the compression amplitude (Fig. 5.5, black lines). The compression amplitude was then increased by 6.35 mm, and the 8 load-unload cycles were repeated, producing an averaged load-displacement curve for the new amplitude (Fig. 5.5, points 4,

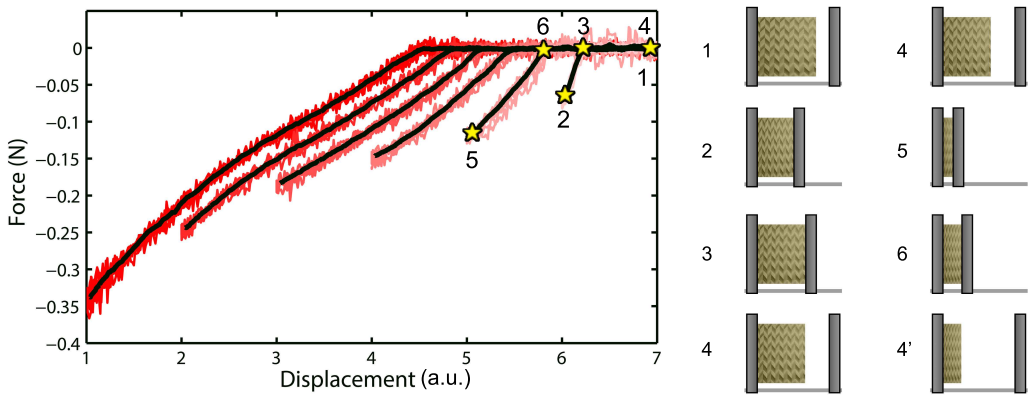

Figure 5.5: Schematic illustration of the loading protocol used to measure the compressive modulus of origami structures. This force-displacement data is a subset of the complete data sets showing only 6 displacement amplitudes and 7 of the 8 compression cycles. See text for description.

5, 6). This process was iterated until the lattice was compressed to a width of 12.7 mm, yielding load-displacement curves with amplitudes evenly spaced by 6.35 mm.

In the main text, it was preferable to express the Miura-ori configuration in terms of the vertex angle ε in order to have a single-valued representation of the energy diagram for PTDs. However, pre-existing theory[3], which did not consider the existence of PTDs, has been expressed in terms of a dihedral angles θ (Fig. 5.5(A)). Thus, to make comparisons to existing theory for non-defected lattices we express our results in terms of θ, which relates to ε by

$$\sin\left(\frac{\varepsilon}{2}\right) = \frac{\cos(\alpha)}{\left[1 - \sin^2(\alpha)\sin^2(\theta/2)\right]^{1/2}}. \tag{5.1}$$

To determine the compressive modulus, we first transformed the plate separation data to the lattice averaged dihedral angle θ. For a given instantaneous compression, this was found by dividing the Miura-ori width by the number

of unit cells across, and calculating θ for the corresponding width of an ideal unit cell[3]. Differentiating each curve to find $K_y(\theta)$, we found the modulus at a given θ was largely insensitive to the equilibrium θ_0 as well as the maximum compression amplitude. This finding was fortuitous, as it allowed us to simply average the values of $K_y(\theta)$ across compression amplitudes for a given θ. Small-amplitude measurements of the modulus were extracted from data where the Miura-ori's compression was less than 6.35 mm.

5.4.2 Compressive modulus

To experimentally determine the range of mechanical properties exhibited by the Miura-ori available for metamaterial design, samples were fabricated and tested in our compression apparatus. Under loading, the equilibrium value of the dihedral angle, θ_0, varies due to plastic deformation at the crease. Thus, to measure the mechanical properties of the Miura-ori, we systematically vary θ_0 and make small amplitude measurements of the uniaxial compressive modulus $K_y(\theta)$ (Fig. 5.6 dots). This measurement was repeated for samples fabricated with each value of α (Fig. 5.6 different colors). Data sets were then fit to a theoretical model based on the properties of a single Miura-ori unit cell where Hookean elasticity was assumed for each crease[3] (Fig. 5.6 solid lines). We found excellent agreement for $\alpha \geq 45^\circ$, and slightly larger deviations in the remaining two samples. From the fits, we extracted the elastic spring constant characterizing a crease in the origami structure k_0, and compared this value to a measurement made on a sheet with only a single fold (Fig. 5.6 inset; solid line). We found the fitted and measured values of k_0 agree to better than a factor of 2. Such deviations from the theoretical prediction may arise from heterogeneous

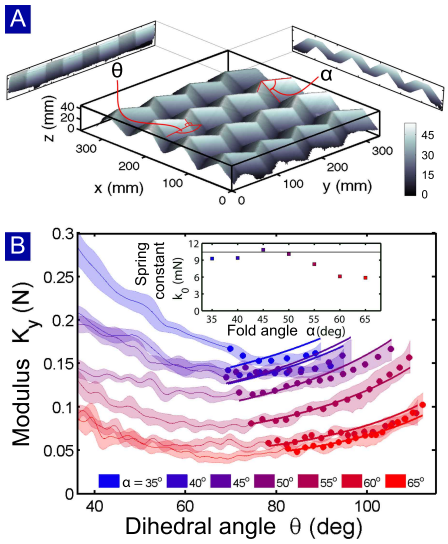

Figure 5.6: (A) A 3D image of a 4×4 Miura-ori with two in-plane projections at equilibrium illustrates the folded structure. Color bar gives height in mm. (B)Small strain measurements of the compressive modulus $K_y(\theta)$ (dots) are compared to theoretical fits (thick lines) for various angles α (colors). Measurements extend beyond the small strain limit (thin lines), and colored bands indicate error estimates. (Inset) From the theoretical fits, we extract the elastic spring constant of a single crease k_0 for each α (points) and compare to a measurement made on a single crease (black line).

deformations that occur in lattices made with more than 1 unit cell, as well as facet bending, which was not accounted for in the single-unit-cell theory. Extending these measurements beyond the validity of the small strain theory, we measured $K_y(\theta)$ over a larger range of compression (Fig. 5.6 shaded bands). For our samples, these data show a factor of ≈ 2 difference between the least and most compliant portions of the modulus for fixed α, and a factor of ≈ 3 between samples with different α.

5.4.3 Poisson's ratio

Miura-ori structures with α varied from 35° to 65° were marked with colored dots on the vertices and compressed using the same set-up as that for the force measurements. 1080p videos of the compression were filmed from overhead using a digital camera at 7.5 fps (Canon Powershot). The colored markings were tracked using custom software written in MATLAB, and the lengths L, widths W, and dihedral angle θ of all the unit cells except those along the border were calculated by measuring the distances between pairs of valley vertices within a unit cell. L, W, and θ were sampled every three frames, and a moving average was computed to produce a smooth measurement of $L(W)$. dL/dW at each frame was defined as the derivative of the quadratic function centered at that frame fit to the values $L(W)$ for 13 frames. The Poisson's ratio ν was then calculated using

$$\nu = -\frac{W}{L}\frac{dL}{dW} \tag{5.2}$$

and compared to a theoretical prediction[3]:

$$\nu = 1 - \left[\frac{1}{\sin(\alpha)\sin(\theta/2)}\right]. \tag{5.3}$$

The comparison between experiment and theory (Fig. 5.7) shows excellent agreement within measurement errors, and confirmed the wide range of negative Poisson ratio possible within the Miura-ori.

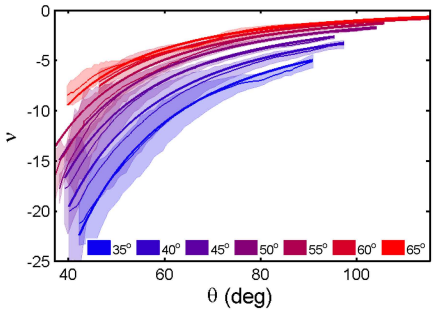

Figure 5.7: The experimentally measured Poisson ratio ν as a function of compression is shown in thin lines with error estimates as shaded bands. Thick lines are parameter-free theoretical predictions, which agree favorably with the data. Colored bands correspond to values of α.

5.4.4 Details of theoretical calculations

Spherical geometry

Traditional Miura-ori vertices consist of four creases (Fig. 5.8(A)). To include the experimentally observed facet bending that occurs during formation of a PTD, we require two additional creases whose equilibrium angle is π. In general, equilibrium crease angles are determined by the plastic deformation induced during folding; however, they are also related by geometric constraints. Assuming symmetric deformations of the unit cell, we choose ε and ϕ to specify the other fold angles (Fig. 5.8(B)). Spherical trigonometry then leads to the following intermediate relationships that determine the angles η, B_+, B_-, A_+, A_-:

$$\cos\eta = \sin^2\frac{\alpha}{2} + \cos^2\frac{\alpha}{2}\cos\phi, \tag{5.4}$$

$$\cos B_+ = \tan\frac{\alpha}{2}\sqrt{\frac{1-\cos\eta}{1+\cos\eta}}, \tag{5.5}$$

$$\cos B_- = \frac{\cos\varepsilon - \cos\alpha\cos\eta}{\sin\alpha\sin\eta}, \tag{5.6}$$

$$\cos A_+ = \cos B_+, \tag{5.7}$$

$$\cos A_- = \frac{\cos\alpha - \cos\varepsilon\cos\eta}{\sin\varepsilon\sin\eta}, \tag{5.8}$$

$$\cos\frac{\theta_-}{2} = \frac{\cos\eta - \cos\varepsilon\cos\alpha}{\sin\varepsilon\sin\alpha} \tag{5.9}$$

With these relations, we find the fold angles obey:

$$\theta_+ = A_+ + A_-, \tag{5.10}$$

$$\theta_- = 2\cos^{-1}\left[\frac{\cos\eta - \cos\varepsilon\cos\alpha}{\sin\varepsilon\sin\alpha}\right], \tag{5.11}$$

$$\beta = B_+ + B_-. \tag{5.12}$$

Energetics

The energy of a Miura-ori vertex can be calculated if we assume that each fold behaves as a linear torsional spring with a preferred rest angle. If all the folds have the same spring constant k_0 then the dimensionless energy is

$$\frac{U}{k_0\ell} = \frac{1}{2}(\theta_+ - \theta_0)^2 + \frac{1}{2}(\theta_- + \theta_0 - 2\pi)^2 + (\beta - \beta_0)^2 + (\phi - \pi)^2. \tag{5.13}$$

Here we have assumed that the ground state has θ_0 and β_0 at commensurate values such that there is a non-frustrated state where all the fold angles are at their preferred angle. If we plot the energy as a function of ε, and ϕ (Fig. 2(E), main text) we see there is a region of disconnection as ε passes through π, and above $\varepsilon = \pi$ there is a local minimum where $\phi > \pi$; this is the pop-through defect (PTD).

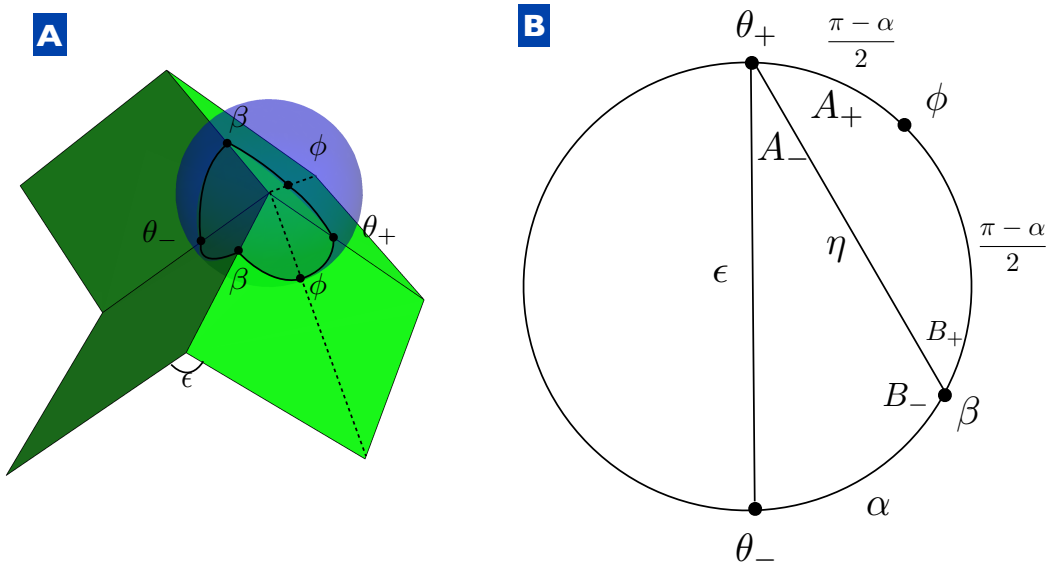

Figure 5.8: (A) A bounding sphere centered on a Miura-ori vertex illustrates the crease and fold angles. (B) The spherical polygon made by unfolding the region bounded by the sphere in (A) schematizes the relationship between the crease and fold angles. In this representation, ε and η are angles in the folded structure that can be most clearly seen by connecting their endpoints in (A). By symmetry only the angles on half of the vertex are shown.

Scaling collapse of K_y^{PTD}

We now derive an expression for the compressive modulus of a pop-through defect (PTD) embedded in a Miura-ori lattice. Our notation follows that of Wei et. al. [3].

A Miura-ori unit cell has dimensions L_x and L_y given by

$$\begin{aligned} L_x &= 2\ell\zeta, \\ L_y &= 2\ell\xi, \qquad \text{where} \\ \xi &= \sin(\alpha)\sin(\theta/2), \qquad \zeta = \cos(\alpha)(1-\xi^2)^{-1/2}, \end{aligned} \tag{5.14}$$

α is the folding angle, and all facet edges are of length ℓ. For a wide range of

parameters, L_y of a normal unit cell is approximately equal to that of a PTD. The same however, does not apply in the x direction where the equilibrium size of a PTD L_x^{PTD} is larger than that of a normal unit cell L_x^{normal}. This induces a strain on the PTD to accommodate the boundary conditions imposed by the lattice. The mechanical response to external loading is therefore proportional to $L_x^{\text{PTD}} - L_x^{\text{normal}}$.

We may write the total response as a linear superposition of the bulk force response and the effect of the PTD, as long as the defect density n is small enough that the defects do not interact. The inhomogeneous effect of the PTD can be written as a multipole expansion of the point force response, which we approximate using the homogeneous unit cell result. Since there is no net force on the defect the leading order correction is a dipole term. Given a uniform compression along the y direction on a lattice with PTDs as in our experiments, we can write the total force response in a multipole expansion:

$$f_y^{\text{defect}} = f_y^{\text{normal}} + nP\frac{df_x}{d\zeta}. \tag{5.15}$$

The zeroth order term is simply the response of a normal lattice f_y^{normal} to loading on the y direction. Because the PTD exerts no net force on the lattice, the first order correction in Eq.(5.15) is a dipole term $\sim df_x/d\zeta$ of strength P, where f_x is the force response along the x direction arising from strain of the $L_x^{\text{PTD}} - L_x^{\text{normal}}$. With the definition of the compressive modulus $K_y = df_y/d\varepsilon$, we differentiate both sides of Eq.(5.15) to find

$$\begin{aligned} \frac{d}{d\varepsilon}f_y^{\text{defect}} &= \frac{d}{d\varepsilon}f_y^{\text{normal}} + nP\frac{d}{d\varepsilon}\left(\frac{df_x}{d\zeta}\right), \\ K_y^{\text{defect}} &= K_y^{\text{normal}} + nP\frac{d}{d\varepsilon}\left(\frac{df_x/d\varepsilon}{d\zeta/d\varepsilon}\right). \end{aligned} \tag{5.16}$$

Rearranging this expression to match the scaling collapse form described in the

main text, we have

$$\frac{1}{n}\left(\frac{K_y^{\text{defect}}}{K_y^{\text{normal}}}-1\right)=\frac{P}{K_y^{\text{normal}}}\frac{d}{d\varepsilon}\left(\frac{df_x/d\varepsilon}{d\zeta/d\varepsilon}\right)=\frac{K_y^{\text{PTD}}}{K_y^{\text{normal}}}. \tag{5.17}$$

Here, $P = (3 \pm 1) \times 10^{-3}$ is a fitting parameter for the strength of the dipole and an analytic expression for $f_x(\varepsilon)$ is available elsewhere [3] assuming Hookean elasticity for each crease in the unit cell. We note that because the force response along the x direction arises from the strain $L_x^{\text{PTD}} - L_x^{\text{normal}}$, the right hand side is evaluated at the dihedral angle ε^* of the normal unit cells.

REFERENCES

[1] Eitan Grinspun, Mathieu Desbrun, Konrad Polthier, Peter Schroder, and Ari Stern. Discrete differential geometry: an applied introduction. *Acm siggraph course*, 2006.

[2] Timothy D. Gatzke and Cindy M. Grimm. Estimating curvature on triangular meshes. *Int. j. shape model.*, 12:1–28, 2006. DOI: 10.1142/S0218654306000810.

[3] Z. Y. Wei, Z. V. Guo, L. Dudte, H. Y. Liang, and L. Mahadevan. Geometric mechanics of periodic pleated origami. *Phys. rev. lett.*, 110:215501–1, 2013. DOI: 10.1103/PhysRevLett.110.215501.

CHAPTER 6

SQUARE TWIST ORIGAMI AND FIRST ORDER PHASE TRANSITIONS

Jesse L. Silverberg, Arthur A. Evans, Lauren McLeod, Chris D. Santangelo, Thomas Hull, and Itai Cohen, *in preparation*.

6.1 Abstract

Widely known as the art of paper folding, origami also offers a framework to design mechanical metamaterials where bulk elastic properties are tuned by the underlying folding geometry. Here we study the interplay between geometry and mechanics for a tessellatable pattern known as the square twist. When folded from heavy paper, this structure exhibits mechanical bistability whose transition between folded and unfolded states is first order. Moreover, we find a critical point within the experimental phase space, below which exists a "super-critical" phase where the structure is neither folded nor unfolded. With a simple mathematical model, we are able to attribute the observed phenomena to the interplay of the crease and sheet bending energy scales, suggesting an overall design principle for rationally tuning the phase diagram of a square twist.

6.2 Main Text

In many physical problems, simplified geometries are used to model the mechanical response of a material system[1]. As geometries become more complex or more realistic results are desired, numerical methods are generally employed to find detailed responses to external loading. With the rising interest in me-

chanical metamaterials however, geometry has begun to take a more prominent role in analysis and has found equal footing in determining material properties as the underlying constitutive law[2, 3, 4, 5, 6, 7, 8, 9, 10, 11, 12, 13, 14, 15, 16, 17]. One of the most extreme examples comes from tessellated origami-inspired structures, where the underlying folding geometry is used to tune the compressive modulus by orders of magnitude, achieve negative Poisson ratio, and even produce reversibly foldable lattice vacancies[15, 16, 18]. While all these unusual mechanical properties have been identified and studied in a single folding pattern known as the Miura-ori, little is known about any of the other foldable tessellations.

Here, we investigate the mechanical properties of a single unit from the square twist origami tessellation (Fig. 6.1(A,B)). Defined by the edge length L and plane angle ϕ, this pattern consists of an alternating arrangement of 5 square and 4 rhombus facets. The square twist can then be described by the location of 16 points corresponding to the corners of each facet. While these points have a total of $16 \times 3 = 48$ degrees of freedom (DOF), the crease geometry imposes several constraints. 24 DOF are removed by keeping the edge lengths L constant, $2 \times 9 = 18$ DOF are removed by keeping diagonal distances on each facet constant, and 6 DOF can be removed by eliminating global translations and rotations. All together, this leaves $48 - 24 - 18 - 6 = 0$ DOF, indicating that a purely geometric description based on the arrangement of creases has no continuous solutions.

Solving for discrete solutions to the geometric constraints gives two answers, both of which are flat: one is fully *unfolded*, the other is fully *folded*. Quantifying the configuration by the Euclidean distance δ between two points on opposites

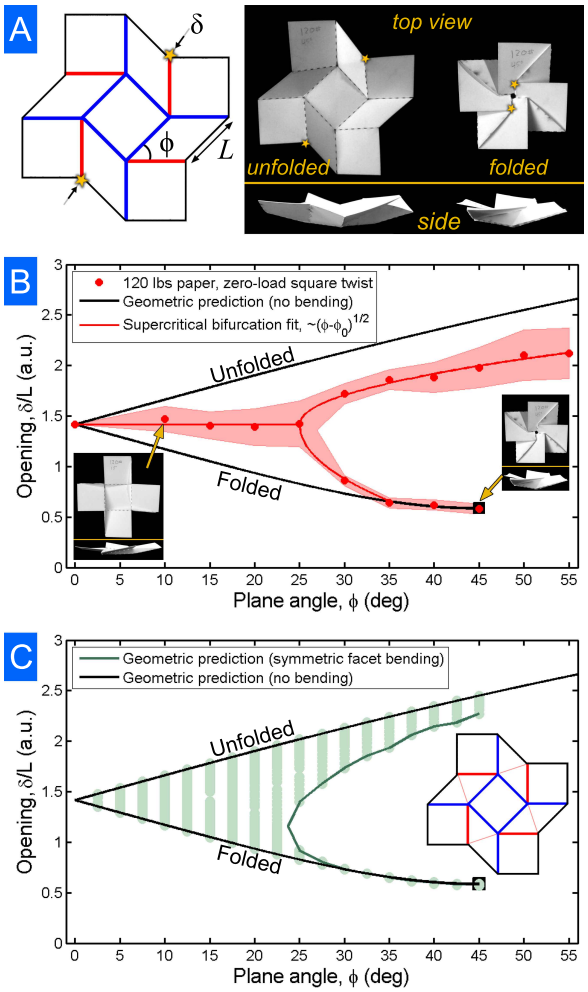

Figure 6.1: (A) The square twist folding pattern is shown here where the edges are in black, mountain creases are in red and valley creases are in blue. The geometry is defined by the length L and the plane angle ϕ. The Euclidean distance between the two yellow stars is δ and quantifies the configuration between the folded and unfolded configurations. Photographs of a square twist with $\phi = 45°$ illustrate out-of-plane deformations as well as the position of the points that define δ when unfolded and folded. (B) Geometric predictions of δ/L assuming rigid facets compared to experimental measurements as a function of ϕ show significant disagreement. Insets show example folded structures. (C) Geometric predictions assuming symmetrically bending facet angles predict a phase diagram that is in much stronger agreement with experiments. Inset shows modified crease pattern where the thin red lines are the locations of facet bending.

sides (Fig. 6.1(A)), a triginometric analysis shows $\delta/L = \sqrt{6 \pm 4(\sin\phi \mp \cos\phi)}$. Here the upper signs correspond to the unfolded solution (Fig. 6.1(B), upper branch), and the lower signs to the folded solution (Fig. 6.1(B), lower branch). Though both satisfy the crease pattern constraints, the DOF argument indicates these configurations are inaccessible from one another, and hence the squre twist is *unfoldable*. Evidently, a description based solely on crease geometry is incomplete, as square twists are readily foldable despite the prediction otherwise (Fig. 6.1(A)).

To understand how square twists made from real materials are able to fold, we used a laser cutter to fabricate these structures from 120 lbs paper. To do so, the outer perimeter was cut with a continuous line while the creases were made by cutting perforated lines and folded by hand to be mountain (out of plane) or valley (into plane). For these samples, we set $L = 2.54$ cm and varied ϕ from 10° to 45° in increments of 5°. The lower bound is the limit of what can be reasonably folded from this material. The upper bound is set by self-intersection, which prevents the structure from folding flat for $\phi > 45^\circ$. Carefully observing each square twist during the folding process revealed that the facets, which are implicitly assumed rigid in the model based on crease pattern geometry, bend by a finite amount. The most pronounced bending occurs on the short diagonals of the four rhombi, and readily exhibited $\approx 10^\circ$ deflections during the folding sequence, with higher deflections possible depending on how the structure was handled.

To test the prediction for δ/L, we folded each sample flat, then performed the measurement with a caliper ruler in the absence of external loads. We then unfolded each sample, flattened it on a table, and performed the measurement

again, similarly without external loads (Fig. 6.1(B), red data points). These measurements revealed a critical plane angle $\phi_c = (25 \pm 2.5)^\circ$ that separated qualitatively different behaviors. For $\phi \leq \phi_c$, the distinction between folded and unfolded was ambiguous with a continuum range of δ/L accessible. For $\phi > \phi_c$, we found the square twist had two clearly distinct values of δ/L. As ϕ increased toward 45°, the measured δ/L corresponding to the folded configuration rapidly approached the prediction based on a rigid facet crease geometry. For the same range of ϕ, we found the corresponding unfolded configuration to be systematically lower than the prediction, though this is largely due to out-of-plane deformations induced by creases (Fig. 6.1(A), side view). Fitting each branch of the data to a function of the form $\sim (\phi - \phi_c)^{1/2}$, we find trends characteristic of a supercritical pitchfork bifurcation.

Based on these results, we extend the rigid facet geometric model to permit bending on the 4 rhombi short diagonals, effectively splitting them into two rigid isosceles triangles (Fig. 6.1(C) inset). Imposing 4-fold rotational symmetry, we find a total of $4 - 3 = 1$ DOF is added to the system. Using MATLAB, we sweep through ϕ from 0° to 45° in steps of 2.5° and solve for δ/L as a function of the rhombus facet bending angle ψ_{rhomb}. We take a maximum deflection of ψ_{rhomb} to be 10° and plot the solutions in the $(\delta/L, \phi)$ phase diagram (Fig. 6.1(C)). Similar to experimental observations, we find a bifurcation at $\phi_c = (23 \pm 2)^\circ$, a continuum of solutions between folded/unfolded configurations for $\phi < \phi_c$, and distinct folded/unfolded configurations for $\phi > \phi_c$. Like the experimental data, the lower branch rapidly converges to the rigid facet prediction. Similarly, the upper branch correctly predicts a range of values for δ/L, however, these values overshoot the experimental data. Again, these discrepancies are due to out-of-plane deformations induced by creases in the unfolded sheet. In spite

of these relatively minor differences, we conclude the extra DOF introduced by facet bending is a major factor that enables both the ϕ-dependent bifurcation and foldability of the square twist.

Having examined the square twist's load-free equilibrium states, we ask how the structure transitions from folded to unfolded configurations under uniaxial tension. Attaching opposite ends of a square twist to a linear translation stage and load cell, we performed a series of displacement-controlled measurements of the force F as a function of extension Δx and plane angle ϕ (Fig. 6.2(A); see SI). In these experiments, we found a critical plane angle $\phi_c = 30°$ that was slightly larger than the load-free experiments. For $\phi \leq \phi_c$ the force generally increased monotonically with extension. Conversely, when $\phi > \phi_c$, the force initially increased with extension, but then decreased to a minimum value, before increasing again at a much lower rate. From visual inspection, we saw the sharpest decrease in force was accompanied by a rapid and sudden opening of the square twist. We quantified this by video recording the experiments with a Cannon Powershot camera filming at 7.5 fps, and with standard image analysis techniques, measured δ as a function of the normalized extension $\Delta x/L$. This data confirmed the rapid opening of the square twist correlates with a similarly rapid decrease in the measured load F (Fig. 6.2(A,B)). When viewed from the perspective of phase transitions, this data suggest the jump between folded and unfolded configurations is a first order phase transition with ϕ_c being a critical point in the phase diagram.

To quantitatively explore the analogy to phase transitions, we integrate the force-extension curve to find the mechanical energy $U(\Delta x/L, \phi)$ and normalize by the flexural rigidity D (Fig. 6.3(A); see SI). From the curves corresponding to

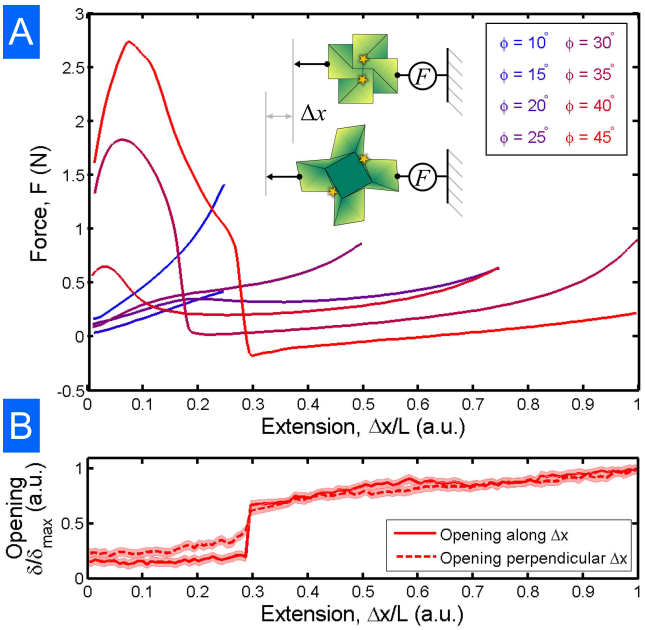

Figure 6.2: (A) Experimental measurements of the tensile force F as a function of the normalized extension $\Delta x/L$ in a strain controlled experiment reveals mechanical bistability between folded and unfolded configurations. The effect decreases with decreasing ϕ, eventually vanishing at a critical angle, $\phi_c = 30°$. Inset shows schematic of the experiment, definition of Δx, and location of the load cell that measures F. (B) Measurements of δ normalized by its maximum value taken both parallel and perpendicular to the loading direction show a discrete jump corresponding to a snap-through instability related to self-intersection.

bistable square twists, we identify each pair of local minima. Generally, the minima at $\Delta x/L = 0$ are more localized than the minima at higher extension. This observation is consistent with our zero-load data that exhibits a narrow range of possible δ/L on the folded branch and a wider range of values on the unfolded branch. When the energy minima are collected together as a function of ϕ, they form a coexistence curve for the system. Similarly, for each energy curve exhibiting bistability, we identify the inflection points that collectively define the stability limit known as a spinodal curve. For a force-controlled experiment, infinitesimal fluctuations crossing the spinodal lead to a sudden transition from

the folded to unfolded phase.

Projecting the coexistence and spinodal curves to the $(\phi, \Delta x/L)$ and $(FL/D, \phi)$ planes represent the data in a manner analogous to thermodynamic phase diagrams. Here, ϕ is the analog of inverse temperature, $\Delta x/L$ to volume, and FL/D to pressure. In the $(\phi, \Delta x/L)$ plane, we overlay the coexistence and spinodal curves onto contours of constant force showing how the stability limits are related to the displacement-controlled experiments (Fig. 6.3(B)). In the $(FL/D, \phi)$ plane, we plot the boundaries of the folded and unfolded phases, which terminate at a critical point ϕ_c. For $\phi < \phi_c$, we find a "supercritical phase." From thermodynamics, it is known that a supercritical fluid can not be distinguished as gas or liquid. Mapping this analogy back to origami, a supercritical square twist can not be distinguished as folded or unfolded, as was seen in the zero-load experiments (Fig. 6.1). Above ϕ_c the system phase separates into folded and unfolded phases separated by a mixed phase region.

While the geometric model with facet bending was able to reproduce key elements of the zero-load phase diagram, it is unable to map a specific trajectory through phase space during loading. The missing ingredient is an energetic expression that accounts for the mechanical energy of facet bending and crease folding. By adding this to the model, we can explore how material properties influence bistability of the system. Thus, we extend the model to allow for bending on all facets (Fig. 6.4(A)) and assign an elastic energy given by

$$\begin{aligned} U_{\text{total}} &= U_{\text{crease}} + U_{\text{bend}}, \\ &= \frac{L}{2}\left[k_c \sum_{i=1}^{12}(\theta_i - \theta_0)^2 + k_b \sum_{j=1}^{9} \lambda_j \psi_j^2\right], \qquad (6.1) \\ \text{where} \quad \lambda_j &= \begin{cases} \sqrt{2} & \text{for square facets,} \\ 2\sin(\phi/2) & \text{for rhombus facets.} \end{cases} \end{aligned}$$

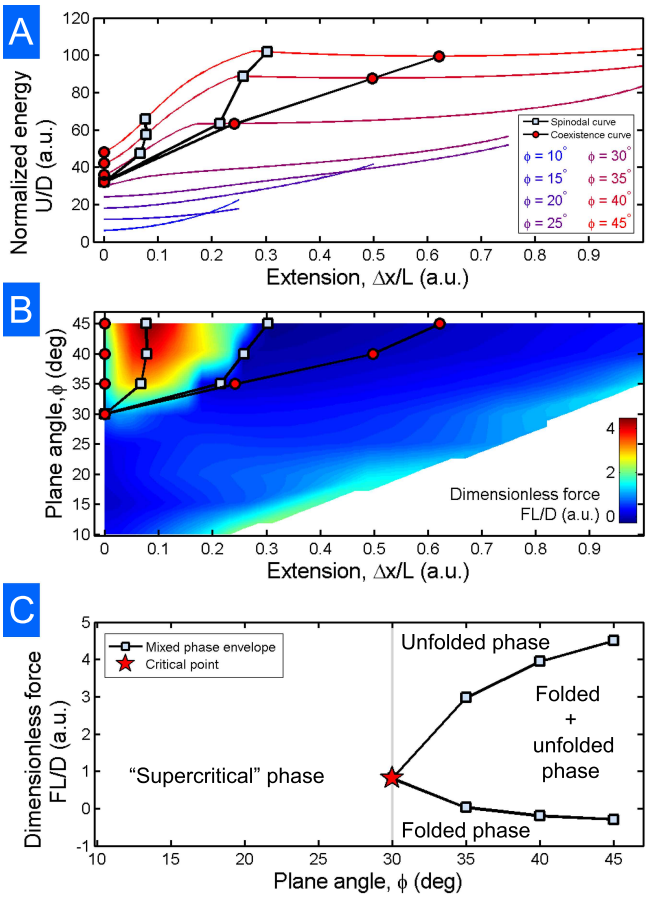

Figure 6.3: (A) From the normalized energy U/D, we identify local minima and inflection points wherever possible to construct coexistence and spinodal curves. Plotting these curves in the (B) $(\phi, \Delta x/L)$ and (C) $(FL/D, \phi)$ planes produces boundaries of the phase diagrams. We find well-defined boundaries between the folded/unfolded phases as well as the existence of a mixed-phase and a "supercritical" phase that is neither folded nor unfolded.

In this expression, the first term is the crease energy, which is proportional to the torsional elastic constant k_c times the length of the crease L, and is a function of the angular opening measured relative to an equilibrium value $\theta_0 = 10°$. The specific numerical value is taken from observations of isolated creases, which tend to have a small non-zero angle. The second term is the facet bending energy, which is proportional to the torsional elastic constant k_b times the length of

the bend $\lambda_j L$, and is a function of the angular deflection of ψ_j from 0°. Specifying ϕ and a target $\Delta x/L$, Eq. (6.1) was numerically minimized using the Levenberg-Marquardt algorithm in MATLAB. This process was repeated 5 times with initial conditions generated from a geometric interpolation between the folded and unfolded states that did not preserve facet areas. In each realization, the facet corners were perturbed by a random amount along x, y, and z that was uniformly distributed over the interval $[0, L/10]$. In this way, we used semi-random initial conditions to form an ensemble-averaged solution that minimized Eq. (6.1). We then averaged the facet bending angles of the ensemble-averaged solution producing an overall average rhombus bending angle ψ_{rhomb}, an overall average square facet bending angle ψ_{sqr}, and a center square facet bending angle ψ_{ctr}. Note that by its placement at the center of the square twist, ψ_{sqr} has no other facets on the structure to average with.

Taking $k_c = k_b \equiv k$, we plot the bending angles as a function of extension (Fig. 6.4(A)). We find both ψ_{rhomb} and ψ_{sqr} are deflected by an amount that increases with ϕ, whereas ψ_{ctr} has relatively smaller deflections that do not systematically vary with ϕ. 3D renders illustrate the overall configuration as the square twist is unfolded (Fig. 6.4(B)), which is in strong qualitative agreement with the paper model. Plotting the total energy reveals a double minimum with spinodal and coexistence points for $\phi > \phi_c = 30°$, and only a single minimum for $\phi \leq \phi_c$ (Fig. 6.4(C)). These results and corresponding phase diagram quantitatively agree with the experimental data (Fig. 6.3(A)), but indicate a non-negligible role for bending of the square facets. Indeed, the model predicts finite facet bending that becomes more pronounced with increasing ϕ in both folded and unfolded configurations. Experiments with paper agree with this prediction and show a small, but non-zero bending on both square and rhombi facets

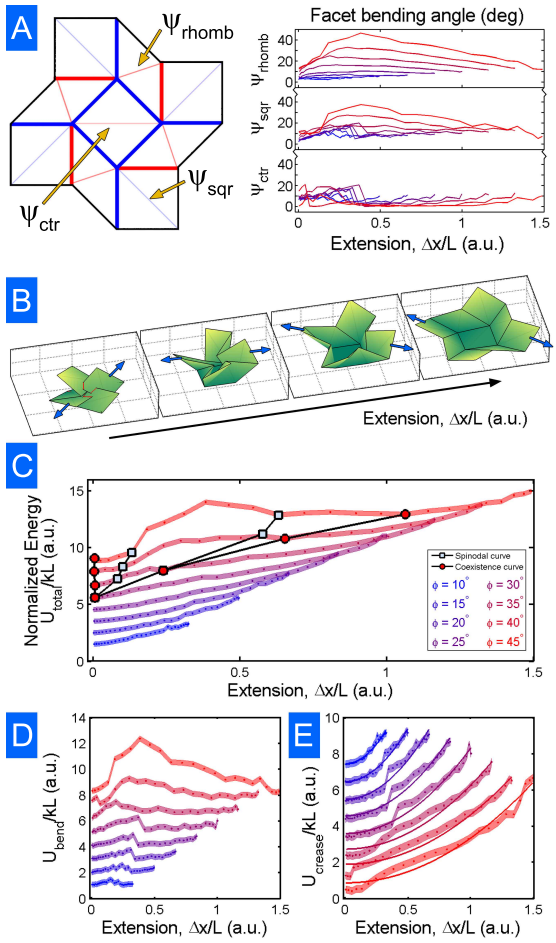

Figure 6.4: (A) Thin lines in this schematic diagram illustrates where facet bending is allowed to occur. In addition to labeling the bending angles, we show the extension-dependence in a simulation where $k_c = k_b \equiv k$. In these 3 plots, ψ_{rhomb} and ψ_{sqr} are averaged with the rotationally symmetric partners. (B) 3D renders from the same simulation illustrates the unfolding sequence. Blue arrows indicate the external load corresponding to strain-controlled conditions, wherein the loading orientation rotates relative to the central facet. (C) Plotting the total normalized energy as a function of extension shows mechanical bistability as indicated by the spinodal and coexistence curves. (D) The energetic contribution due to bending exhibits signature of bistability, while (E) the energetic contribution due to crease opening does not. For all energy plots, the band thickness is the error determined from an ensemble average and the data points are mean values at a given extension. In (E) the thin lines correspond to quadratic fits. Color coding for all data plots is self-consistent and given in the legend for (C).

exist, though the square facet bending is notably less pronounced (Fig. 6.1(A), side view).

A benefit of the combined geometric and mechanical model is that it allows us to separately examine the energetic contributions from facet bending, U_{bend}, and crease deformation, U_{crease}. Plotting these individual contributions to the total energy, we find the bending energy has two minima corresponding to the folded and unfolded states (Fig. 6.4(D)), while the crease energy follows an approximately quadratic dependence on extension (Fig. 6.4(E)). The double minima in bending energy is easily interpreted by recognizing the facets bend only during the transition between folded and unfolded states in order to satisfy the geometric constraints imposed by the crease geometry. The quadratic dependence of crease energy on extension is similarly understandable by noting that the crease angles θ_i increase with extension in an approximately linear fashion. Thus, bistability of the square twist requires the facet bending energy scale to be non-negligible compared to the crease energy scale. We therefore expect that in materials with $k_b/k_c \gg 1$, there should be a pronounced mechanical bistability for all ϕ that converges to the rigid geometry prediction as $k_b/k_c \to \infty$ (Fig. 6.1(B), black lines). Similarly, when $k_b/k_c \ll 1$, the energetics are dominated by the creases and hence should exhibit monostability as $k_b/k_c \to 0$. In the marginal regime where $k_b/k_c \sim 1$, the mono- or bistability varies with ϕ, and as already shown, exhibits a critical point with a first order phase transition (Fig. 6.4(C)).

Taken together, these results show that while the geometric structure of the square twist has the potential for mechanical bistability, whether or not it manifests depends on the underlying material's mechanical properties. This generalized design principle has important implications for engineering origami-

inspired structures and indicates that critical attention should be paid to the relative crease and bending energy scales. More broadly, we recall that in the analogy to thermodynamics, the plane angle ϕ took on the role of temperature. In the $(FL/D, \phi)$ phase diagram the folded/unfolded phase transition occurs at finite temperature, but due to the high energetic cost to induce in-plane shearing of paper, fluctuations in ϕ are essentially 0. Thus, a sheet of paper can not be expected to transition between folded and unfolded states by crossing into the supercritical phase. However, recently developed techniques in polymer engineering have demonstrated that temperature-dependent swelling[10] and bending[11] behaviors can be engineered to fabricate sub-mm origami structures. Therefore, with controlled in-plane swelling that varies ϕ, it is possible to construct a system that continuously transitions between folded and unfolded states by passing through the supercritical phase. Such a device would have interesting potential applications in biomedicine[19], soft robotics[20], and or micro-optics[21] as a temperature-dependent mechanical switch.

6.3 Acknowledgments

The authors thank R. J. Lang, B. Johnson, B. Parker, and M. Schneider for artistic inspiration, as well as O. Vincent, N. Bende, and the Cohen lab for useful discussions. We also thank F. Parish for assistance with the laser cutter. This work was funded by the National Science Foundation through award EFRI ODISSEI-1240441 and the GRFP, which funded J.L.S.

REFERENCES

[1] L. D. Landau and E. M. Lifshitz. *Landau and lifshitz course of theoretical physics volume 7: theory of elasticity*. Butterworth Heinemann, New Delhi, 3rd edition, 1986.

[2] Martin Wegener. Metamaterials beyond optics. *Science*, 342:939–940, 2013.

[3] Yongmin Liu and Xiang Zhang. Metamaterials: a new frontier of science and technology. *Chem. soc. rev.*, 40:2494–2507, 2011.

[4] Jae-Hwang Lee, Jonathan P. Singer, and Edwin L. Thomas. Micro-/nanostructured mechanical metamaterials. *Adv. mater.*, 24:4782–4810, 2012.

[5] A. Q. Liu, W. M. Zhu, D. P Tsai, and N. I. Zheludev. Micromachined tunable metamaterials: a review. *J. opt.*, 14:114009–1, 2012.

[6] Muamer Kadic, Tiemo Buckmann, Robert Schittny, and Martin Wegener. Metamaterials beyond electromagnetism. *Rep. prog. phys.*, 76:126501–1, 2013.

[7] Charlotte Py, Paul Reverdy, Lionel Doppler, Jose Bico, Benoit Roman, and Charles N. Baroud. Capillary origami: spontaneous wrapping of a droplet with an elastic sheet. *Phys. rev. lett.*, 98:156103–1, 2007. DOI: 10.1103/PhysRevLett.98.156103.

[8] Alessandro Papa and Sergio Pellegrino. Systematically creased thin-film membrane structures. *J. space rockets*, 45:10–18, 2008. DOI: 10.2514/1.18285.

[9] Noy Bassik, George M. Sten, and David H. Gracias. Microassembly based on hands free origami with bidirectional curvature. *Appl. phys. lett.*, 95:091901–1, 2009. DOI: 10.1063/1.3212896.

[10] Jungwook Kim, James A. Hanna, Myunghwan Byun, Christian D. Santangelo, and Ryan C. Hayward. Designing responsive buckled surfaces by halftone gel lithography. *Science*, 335:1201–1205, 2012. DOI: 10.1126/science.1215309.

[11] Jungwook Kim, James A. Hanna, Ryan C. Hayward, and Christian D. Santangelo. Thermally responsive rolling of thing gel strips with discrete variations in swelling. *Soft matter*, 8:2375–2381, 2012. DOI: 10.1039/c2sm06681e.

[12] Marcelo A. Dias, Levi H. Dudte, L. Mahadevan, and Christian D. Santangelo. Geometric mechanics of curved crease origami. *Phys. rev. lett.*, 109:114301–1, 2012. DOI: 10.1103/PhysRevLett.109.114301.

[13] Marcelo A. Dias and Christian D. Santangelo. The shape and mechanics of curved-fold origami structures. *Epl*, 100:54005–p1, 2012. DOI: 10.1209/0295-5075/100/54005.

[14] Jennie Ryu, Matteo D'Amato, Xiaodong Cui, Kevin N. Long, H. Jerry Qi, and Martin L. Dunn. Photo-origami: bending and folding polymers with light. *Appl. phys. lett.*, 100:161908–1, 2012. DOI: 10.1063/1.3700719.

[15] Mark Schenk and Simon D. Guest. Geometry of miura-folded metamaterials. *Proc. natl. acad. sci.*, 110:3276–3281, 2013. DOI: 10.1073/pnas.1217998110.

[16] Z. Y. Wei, Z. V. Guo, L. Dudte, H. Y. Liang, and L. Mahadevan. Geometric mechanics of periodic pleated origami. *Phys. rev. lett.*, 110:215501–1, 2013. DOI: 10.1103/PhysRevLett.110.215501.

[17] Mustapha Jamal, Sachin S. Kadam, Rui Xiao, Faraz Jivan, Tzia-Ming Onn, Rohan Fernandes, Thao D. Nguyen, and David H. Gracias. Bio-origami hydrogel scaffolds composed of photocrosslinked peg bilayers. *Adv. healthcare mater.*, 2:1142–1150, 2013. DOI: 10.1002/adhm.201200458.

[18] J. L. Silverberg, Arthur A. Evans, L. McLeod, C. D. Santangelo, T. Hull, and I. Cohen. Using origami design principles to fold reprogrammable mechanical metamaterials. *Under review*, 2014.

[19] Daisuke Nakayama, Yukikazu Takeoka, Masayoshi Watanabe, and Kazunori Kataoka. Simple and precise preparation of a porous gel for a colorimetric glucose sensor by a templating technique. *Angewandte chemie*, 115(35):4329–4332, 2003.

[20] Yoshihito Osada and Jian-Ping Gong. Soft and wet materials: polymer gels. *Advanced materials*, 10(11):827–837, 1998.

[21] Jongseong Kim, Michael J Serpe, and L Andrew Lyon. Hydrogel microparticles as dynamically tunable microlenses. *Journal of the american chemical society*, 126(31):9512–9513, 2004.

6.4 Supplemental Information

6.4.1 Measuring flexural rigidity

To normalize experimental force and energy data, the flexural rigidity D was measured from a strip of 120 lbs paper whose dimensions were $L \times 8.5L$, with $L = 2.54$ cm. To make this measurement, an apparatus was used to clamp the strip horizontally, allowing a controlled length to be suspended under gravity. Digital photographs were taken from a side view so that the strip could be seen edge-on and its deflection determined. Thus, we captured a series of images where the suspended arc length ℓ varied from L to $8L$, and with standard image tracking techniques, we extracted the vertical deflection z as a function of horizontal position x. This coordinate data was fit to the expression[1]

$$z = \left(\frac{\rho g t}{24D}\right)\left(x^4 - 4\ell x^3 + 6\ell^2 x^2\right), \tag{6.2}$$

where ρ is the measured paper density and t is the measured paper thickness. Eq. (6.2) was derived for the small deflection limit and allowed us to perform a one-parameter fit for D as ℓ was varied from L to $8L$. Generally, measurements for $\ell < 2L$ were dominated by an intrinsic curvature in the paper. For $\ell = 8L$ there were also noticeable deviations from to the small-deflection approximation used to derive Eq. (6.2). For all other values of ℓ, the fits were tightly clustered around some median value. Flipping the strip over and repeating the measurements on the opposite side produced another set of values for D as a function of ℓ that exhibited the same trends. Averaging the median values from each data set yielded the value used in the main text, $D = (15.6 \pm 0.7) \times 10^{-3}$ Nm.

6.4.2 Force measurement apparatus

A custom built tensile tester was developed to measure the mechanical properties of origami structures. This consisted of two smoothly polished aluminum compression plates, one mounted to a Haydon-Kerk linear translation stage (PCM4826X-K IDEA stepper motor), and the other to a Loadstar force measurement sensor (3 kg RSP1 load cell with DI-1000U interface). In a typical experiment, the distance between loading plates and load cell force data were simultaneously recorded by a single custom MATLAB program. Samples were suspended in air under minor tension to prevent interactions with the lower surface that might interfere with the unfolding process.

REFERENCES

[1] L. D. Landau and E. M. Lifshitz. *Landau and lifshitz course of theoretical physics volume 7: theory of elasticity*. Butterworth Heinemann, New Delhi, 3rd edition, 1986.

CHAPTER 7

COLLECTIVE MOTION OF HUMANS IN MOSH AND CIRCLE PITS AT HEAVY METAL CONCERTS

Jesse L. Silverberg, Matthew Bierbaum, James P. Sethna, and Itai Cohen, *Phys. Rev. Lett.* **110**, 228701-1 (2013).

7.1 Abstract

Human collective behavior can vary from calm to panicked depending on social context. Using videos publicly available online, we study the highly energized collective motion of attendees at heavy metal concerts. We find these extreme social gatherings generate similarly extreme behaviors: a disordered gas-like state called a *mosh pit* and an ordered vortex-like state called a *circle pit*. Both phenomena are reproduced in flocking simulations demonstrating that human collective behavior is consistent with the predictions of simplified models.

7.2 Main Text

Human collective behaviors vary considerably with social context. For example, lane formation in pedestrian traffic [1], jamming during escape panic [2], and Mexican waves at sporting events [3] are emergent phenomena that have been observed in specific social settings. Here, we study large crowds (10^2 – 10^5 attendees) of people under the extreme conditions typically found at heavy metal concerts [4]. Often resulting in injuries [5], the collective mood is influenced by the combination of loud (130 dB [6]), fast (*blast beats* exceeding 300 beats per

Figure 7.1: This photograph illustrates typical collective behavior found in a mosh pit at heavy metal concerts. Notice that some attendees are participating (foreground), while others are not (background). Image courtesy of Ulrike Biets.

minute) music, synchronized with bright flashing lights, and frequent intoxication [7]. This variety and magnitude of stimuli are atypical of more moderate settings, and contribute to the collective behaviors studied here (Fig. 7.1).

Thousands of videos filmed by attendees at heavy metal concerts [1] highlight a collective phenomenon consisting of $10^1 - 10^2$ participants commonly referred to as a *mosh pit*. In traditional mosh pits, the participants (moshers) move randomly, colliding with one another in an undirected fashion (Fig. 7.2(A); see SI for video metadata). Mosh pits can form spontaneously or at the suggestion of the performing band, but in both cases, no micromanagement of individual actions is generally involved. Qualitatively, this phenomenon resembles the kinetics of gaseous particles, even though moshers are self-propelled agents that

[1]Over 10^5 videos are available on YouTube.com illustrating mosh pits and circle pits. Some notable examples include: `http://youtu.be/5jKU7gdxncE`, `http://youtu.be/qkbOyg3NOiE`, `http://youtu.be/nOHY1YxX5iA`, `http://youtu.be/o7w7m4lb2ok`, `http://youtu.be/l6R7PiISaZw`.

experience dissipative collisions and exist at a much higher density then most gaseous systems. To explore this analogy quantitatively, we watched over 10^2 videos containing footage of mosh pits on YouTube.com, obtained six that were filmed from a suitably high position to provide a clear view of the crowd, corrected for perspective distortions [8] as well as camera instability, and used PIV analysis [9] to measure the two-dimensional (2D) velocity field on an interpolated grid (Fig. 7.2(B)).

Video data of mosh pits was used to calculate the velocity-velocity correlation function c_{vv}, where we noted an absence of the spatial oscillations typically found in liquid-like systems (Fig. 7.2(B) inset) [10]. Generally, c_{vv} was well fit by a pure exponential, and for the video used in Fig. (7.2), the decay length was 0.39 ± 0.03 m, which is approximately human shoulder width. Taken together, these findings offer strong support for the analogy between mosh pits and gases. As a further check, we examined the 2D speed distribution. Previous observations of human pedestrian traffic and escape panic led us to expect a broad distribution not well described by simple analytic expressions [11, 2]. However, the measured speed distribution in mosh pits was well fit by the 2D Maxwell-Boltzmann (MB) distribution, which is characterized by the probability distribution function $\mathrm{PDF}(v) = (2v/T)e^{-v^2/T}$ and temperature T (Fig. 7.2(C) and inset). These observations present an interesting question: why does an inherently non-equilibrium system exhibit equilibrium characteristics?

Studies of collective motion in living and complex systems have found notable success within the framework of flocking simulations [12, 13, 14, 15, 16, 17, 18, 19, 20]. Thus, we use a Vicsek-like model [20] to simplify the complex behavioral dynamics of each human mosher to that of a simple soft-bodied par-

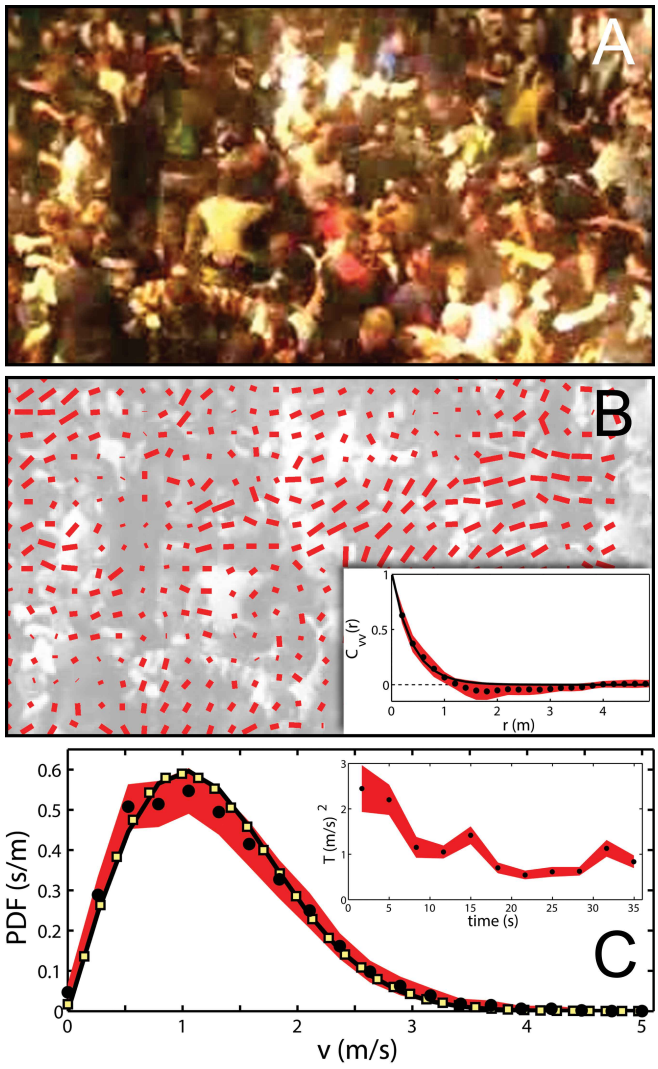

Figure 7.2: (A) Single video frame illustrating a characteristic mosh pit. (B) The same video image with overlaid velocity field. To facilitate comparisons with (A), this image is not corrected for perspective distortions. Inset shows the measured velocity-velocity correlation c_{vv} (solid black circles) as a function of distance r, as well as the best-fit to a pure exponential (black line, $R^2 = 0.97$). (C) The measured PDF for speed from the same video (solid black circles), the best fit to a 2D MB distribution (black line), and the speed distribution found in simulations (yellow squares). Inset shows the best-fit temperature as a function of time illustrating that an initially "hot" mosh pit "cools down". Error estimates are in red for all plots.

ticle we dub a Mobile Active Simulated Humanoid, or MASHer. Our model includes two species of MASHers to reflect the typical crowd at heavy metal concerts where we find both active and passive participants (Fig. 7.1, foreground and background, respectively) [21]. Active MASHers repel during collisions, exhibit self-propulsion, experience flocking interactions, and are subject to random fluctuations due to environmental stimuli. These effects are modeled as forces on the i^{th} MASHer by:

$$\vec{F}_i^{\text{repulsion}} = \begin{cases} \epsilon\left(1 - \frac{r_{ij}}{2r_0}\right)^{3/2} \hat{r}_{ij}, & r_{ij} < 2r_0 \\ 0, & \text{otherwise} \end{cases} \tag{7.1}$$

$$\vec{F}_i^{\text{propulsion}} = \mu(v_0 - v_i)\hat{v}_i, \tag{7.2}$$

$$\vec{F}_i^{\text{flocking}} = \alpha \sum_{j=0}^{N_i} \vec{v}_j \Big/ \left| \sum_{j=1}^{N_i} \vec{v}_j \right|, \tag{7.3}$$

$$\vec{F}_i^{\text{noise}} = \vec{\eta}_i. \tag{7.4}$$

The Hertzian repulsion force [22] has a strength ϵ, and is determined by the MASHer radius r_0, as well as the distance r_{ij} and direction $\hat{r}_{ij}$ between MASHers i and j. A variant of this expression with a 5/2 power-law was tested and found to produce quantitatively similar results. The self-propulsion force has a strength μ, is aligned with the MASHer heading $\hat{v}_i$, and is proportional to the difference between the current speed v_i and the preferred speed v_0. The flocking force has a strength α, and is in the direction found by vectorially averaging the headings of the N_i MASHers within a distance $r_{\text{flock}} = 4r_0$ of MASHer i. Consistent with previous work [13, 17, 20], this distance was fixed in our model so that $r_0 < r_{\text{flock}} < L$, where L is the system size. This choice minimizes the influence of finite-size effects on the flocking force [12]. Finally, the random force $\vec{\eta}_i$ is a vector whose components $\eta_{i,\lambda}$ are drawn from a Gaussian distribution with zero mean and standard deviation σ defined by the correlation function $\langle \eta_{i,\lambda}(t)\eta_{i,\kappa}(t')\rangle = 2\mu\sigma^2\delta_{\lambda\kappa}\delta(t-t')$; the noise is spatially and temporally

decorrelated. Based on observational evidence, the second species in our model, passive MASHers, prefer to remain stationary and are not subject to flocking interactions or random forces. Thus, in the appropriate units, we set $v_0 = 0$, $\alpha = 0$, and $\vec{\eta}_i = \vec{0}$ for passive MASHers. Active MASHers have $v_0 = 1$, while α and σ were varied to explore the phase space of the model. The remaining parameters are the same for all MASHers, and were set to $\epsilon = 25$, $\mu = 0.05$, and $r_0 = 1$.

We simulated concerts with $N = 500$ MASHers at a packing fraction of $\rho = 0.94$. 30% of the population was active, while the remaining was passive. Periodic boundary conditions were used to avoid edge effects, and numerical integration of $\ddot{\vec{r}}_i = \vec{F}_i^{\text{repulsion}} + \vec{F}_i^{\text{propulsion}} + \vec{F}_i^{\text{flocking}} + \vec{F}_i^{\text{noise}}$ was performed with the Newton-Stomer-Verlet algorithm with cell based neighbor lists to expedite computation. Initializing the simulation with uniformly mixed populations, we found that they spontaneously phase separated with a dense region of active MASHers confined by passive MASHers. This occurs generally across parameter space, and appears to be a product of the difference in preferred speeds between populations (SI). For the parameter values studied here, this occurs in about $\sim 10^3 \times (r_0/v_0)$ time units and once formed, remains stable for greater than $10^5 \times (r_0/v_0)$ time units.

We explored the model's phase space by varying α and σ for the active MASHers over the intervals $[0, 1]$ and $[0, 3]$, respectively (Fig. 7.3(A)). This led to 4.8×10^5 individual simulations sampled on 4.8×10^3 grid points. For each run, we measured the active MASHer RMS angular momentum about their center of mass $x_{cm} = (L/2\pi)\text{arctan}(\text{Im(A)}/\text{Re(A)})$, where $L = 1.03\sqrt{\pi r_0^2 N}$ is the simulation box size, $A = \sum_{i=1}^{N_a} \exp(-2\pi i x_i/L)$, N_a is the number of active MASHers, x_i is the x position of the i^{th} MASHer, and a similar expression holds for y_{cm}. In the low-

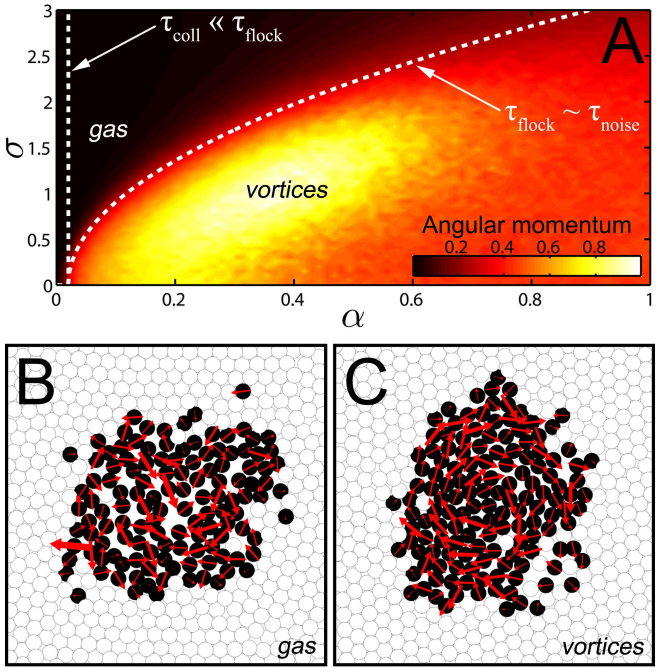

Figure 7.3: (A) The RMS angular momentum of active MASHers exhibits a disordered gas-like state in the high-noise low-flocking limit. The model also predicts an ordered vortex-like state in the low-noise moderate-flocking limit. Dashed white lines correspond to the bounds of the flocking-dominated regime. (B) Active MASHers (black) are confined by passive MASHers (white), and the velocity field (red arrows) resembles that found in actual mosh pits. (C) Active MASHers spontaneously self-organize into an ordered vortex-like state. (Supplemental Movie 1 and 2.)

flocking, high-noise limit, we found the angular momentum was near zero, and upon closer inspection, discovered a gas-like region (Fig. 7.3(B)) where MASHers quantitatively reproduced the statistics found in experimentally observed mosh pits (Fig. 7.2(C)).

To interpret these results, we note that our model has three time scales: (i) the flocking time $\tau_{\text{flock}} = v_0/\alpha$, which can be found by dimensional analysis of Eq.(7.3); (ii) the noise time $\tau_{\text{noise}} = v_0^2/2\mu\sigma^2$, which can be found by calculating the amount of time required for noise to change the correlation function

$\langle [v_i(\tau_{\text{noise}}) - v_i(0)]^2 \rangle = 2\mu\sigma^2\tau_{\text{noise}}$ by an amount equal to the characteristic speed squared; and (iii) the collision time $\tau_{\text{coll}} = 1/(2r_0v_0\rho)$, which is the mean-free-path $(2r_0\rho)^{-1}$ divided by the speed v_0. Both noise and collisions tend to randomize motion, whereas flocking tends to homogenize motion. Thus, when $\tau_{\text{noise}} \ll \tau_{\text{flock}}$, the statistical motion of the system is dominated by random forces. The boundary given by this condition occurs when $\tau_{\text{noise}} \sim \tau_{\text{flock}}$, or rather, $\sigma \sim \sqrt{\alpha/\mu}$ (Fig. 7.3(A)). Similarly, when the $\tau_{\text{coll}} \ll \tau_{\text{flock}}$, collisions cause disordered motion. This regime is bounded by $\alpha \ll 2r_0v_0^2\rho$, which is independent of σ, and for our choice of parameters is ~ 1; empirically, we find $\alpha \sim 10^{-2}$ in agreement with this condition. This demonstrates how a non-equilibrium system of moshers can have equilibrium characteristics: random motions induced by *collisions or noise* of self-propelled agents over a sufficient time reproduce the statistics of classical gases via the Central Limit Theorem.

Conversely, when $\tau_{\text{flock}} \ll \tau_{\text{noise}}$ and τ_{coll}, the flocking term dominates active MASHer motion. With sufficiently low noise, this limit of the model predicts a highly ordered vortex-like state [23, 24] where MASHers again phase separate, but the confined active MASHers move with a large non-zero angular momentum (Fig. 7.3(C)). Remarkably, this spontaneous phase separation and vortex formation is also observed at heavy metal concerts where they are conventionally called *circle pits* (Fig. 7.4; see SI for video metadata). In simulations, we found an even distribution between clockwise (CW) and counter-clockwise (CCW) motion (when viewed from above) that switches directions at random intervals [25]. However, observations from concerts show 5% flow CW with the remaining 95% flowing CCW ($p < 0.001$). This asymmetry is independent of regional conventions in motor vehicle traffic, as video data was collected from a variety of countries including the United State of America, the United King-

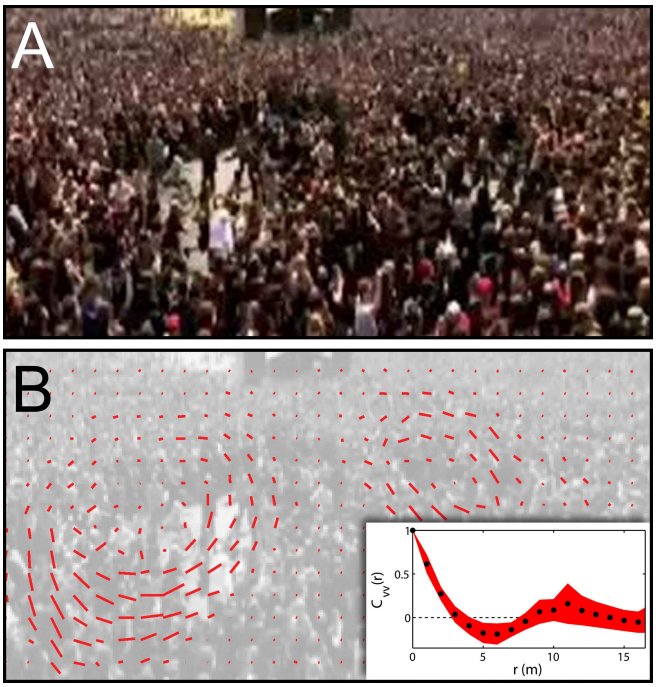

Figure 7.4: The vortex-like state predicted in simulations is also observed at heavy metal concerts, where it is called a circle pit. (A) Single video frame illustrating two side-by-side circle pits. (B) The same video image with overlaid velocity field. To facilitate comparisons with (A), this image is not corrected for perspective distortions. Inset shows the measured velocity-velocity correlation c_{vv} as a function of distance r (solid black circles, error estimates in red). Note that c_{vv} is maximally negative at $r \approx 6$ m, corresponding to the approximate diameter of the leftmost circle pit. Weak oscillations for $r > 6$ m are evident due to long-range correlations between the two circle pits.

dom, and Australia. Though the origin of this effect is unknown, we speculate it may be related to the dominant handedness/footedness found in humans, as it is known to bias turning behaviors [26].

The collective behavior described here has not been predicted on the basis of staged experiments with humans [27, 28], making heavy metal concerts a unique model system for reliably, consistently, and ethically studying human collective motion. Currently, the most significant obstacle to further progress

is the limited availability of publicly available high-quality video footage, and a general reluctance among concert organizers to allow filming at their events. Nevertheless, further studies in this unique environment may enhance our understanding of collective motion in riots, protests, and panicked crowds, as it sheds light on what collective behaviors become possible when traditional social rules are abandoned. Such studies may lead to new architectural safety design principles and crowd management strategies that limit the risk of injury at mass social gatherings [29]. For example, many heavy metal bands routinely announce during live performances "If you see someone fall down in the mosh pit, pick them back up." This simple rule is known to reduce the risk of injury by trampling, and if employed in other extreme social gatherings, would be expected to have similar social benefits. Similarly, within the MASHer model, we found that by setting the preferred speed $v_0 = 0$, all mosh and circle pit behaviors ceased, suggesting an alternative approach to real-world crowd safety management.

Heavy metal concerts have the further advantage of exhibiting a rich variety of collective behaviors such as: (i) the *wall of death* (moshers split into two groups separated by an open space and, when signaled, simultaneously run at the opposing group leading to a deliberate mass collision), (ii) *pogoing* (a locally correlated but globally decorrelated collective jumping), and (iii) propagating waves in jammed attendees [30]. In addition to these broadly defined types of collective motion, there are further variations that arise when concert organizers focus on specific musical subgenres that appeal to niché audiences. For example, *hardcore pits*, *ninja pits*, and *push pits* are all variants of the traditional mosh pit with their own unique characteristics that may not, when studied in detail, be well described by Eqs.(7.1-7.4). Thus, heavy metal concerts offer many

new opportunities to study the collective behaviors arising from large groups of humans in extreme social conditions.

7.3 Source Code

Source code and a phase diagram generating Python script are available under the M.I.T. license on github.com at `https://github.com/mattbierbaum/moshpits`. An interactive Javascript version of the simulation is available at `http://mattbierbaum.github.com/moshpits.js`.

7.4 Acknowledgments

The photo in Fig. 7.1 was taken and graciously provided by Ulrike Biets. JLS and MB also thank D. Porter, L. Ristroph, J. Freund, J. Mergo, A. Holmes, A. Alemi, M. Flashman, K. Prabhakara, J. Wang, R. Lovelace, P. McEuen, S. Strogatz, the Cohen Lab, and the Sethna Group. We would also like to thank the enormous number of people who wrote to us about the related arXiv pre-print manuscript (arXiv:1302.1886) for their support, interest, and suggestions. Fieldwork was independently funded by JLS.

REFERENCES

[1] Mehdi Moussaïd, Dirk Helbing, and Guy Theraulaz. How simple rules determine pedestrian behavior and crowd disasters. *Proceedings of the national academy of sciences*, 108(17):6884–6888, 2011.

[2] Dirk Helbing, Anders Johansson, and Habib Zein Al-Abideen. Dynamics of crowd disasters: an empirical study. *Physical review e*, 75(4):046109, 2007.

[3] Illés Farkas, Dirk Helbing, and Tamás Vicsek. Social behaviour: mexican waves in an excitable medium. *Nature*, 419(6903):131–132, 2002.

[4] Robert Walser. *Running with the devil: power, gender, and madness in heavy metal music*. Wesleyan University Press, 1993.

[5] Timothy Janchar, Chris Samaddar, and David Milzman. The mosh pit experience: emergency medical care for concert injuries. *The american journal of emergency medicine*, 18(1):62–63, 2000.

[6] AB Drake-Lee. Beyond music: auditory temporary threshold shift in rock musicians after a heavy metal concert. *Journal of the royal society of medicine*, 85(10):617–619, 1992.

[7] Megan SC Lim, Megan SC Lim, Margaret E Hellard, Megan SC Lim, Margaret E Hellard, Jane S Hocking, Megan SC Lim, Margaret E Hellard, Jane S Hocking, Campbell K Aitken, et al. A cross-sectional survey of young people attending a music festival: associations between drug use and musical preference. *Drug and alcohol review*, 27(4):439–441, 2008.

[8] Charlotte Py, Emmanuel de Langre, Bruno Moulia, and Pascal Hémon. Measurement of wind-induced motion of crop canopies from digital video images. *Agricultural and forest meteorology*, 130(3):223–236, 2005.

[9] EA Cowen and JK Sveen. Piv and water waves, chap. chapter 1: quantitative imaging techniques and their application to wavy flows, 1–49. 2003.

[10] NW Ashcroft. Liquid metals. *Scientific american*, 221:72–82, 1969.

[11] LF Henderson. The statistics of crowd fluids. *Nature*, 229:381–383, 1971.

[12] Iain D Couzin, Jens Krause, Richard James, Graeme D Ruxton, and Nigel R Franks. Collective memory and spatial sorting in animal groups. *Journal of theoretical biology*, 218(1):1–11, 2002.

[13] András Czirók, Eshel Ben-Jacob, Inon Cohen, and Tamás Vicsek. Formation of complex bacterial colonies via self-generated vortices. *Physical review e*, 54(2):1791, 1996.

[14] Volker Schaller, Christoph Weber, Christine Semmrich, Erwin Frey, and Andreas R Bausch. Polar patterns of driven filaments. *Nature*, 467(7311):73–77, 2010.

[15] Naomi E Leonard, Tian Shen, Benjamin Nabet, Luca Scardovi, Iain D Couzin, and Simon A Levin. Decision versus compromise for animal groups in motion. *Proceedings of the national academy of sciences*, 109(1):227–232, 2012.

[16] Dirk Helbing and Peter Molnar. Social force model for pedestrian dynamics. *Physical review e*, 51(5):4282, 1995.

[17] Tamás Vicsek and Anna Zafeiris. Collective motion. *Physics reports*, 517(3):71–140, 2012.

[18] William Bialek, Andrea Cavagna, Irene Giardina, Thierry Mora, Edmondo Silvestri, Massimiliano Viale, and Aleksandra M Walczak. Statistical mechanics for natural flocks of birds. *Proceedings of the national academy of sciences*, 109(13):4786–4791, 2012.

[19] Craig W Reynolds. Flocks, herds and schools: a distributed behavioral model. In *Acm siggraph computer graphics*. Volume 21. (4). ACM, 1987, pages 25–34.

[20] Tamás Vicsek, András Czirók, Eshel Ben-Jacob, Inon Cohen, and Ofer Shochet. Novel type of phase transition in a system of self-driven particles. *Physical review letters*, 75(6):1226, 1995.

[21] Sang Koo You, Dae Hyuk Kwon, Yong-ik Park, Sun Myong Kim, Myung-Hoon Chung, and Chul Koo Kim. Collective behaviors of two-component swarms. *Journal of theoretical biology*, 261(3):494–500, 2009.

[22] L. D. Landau and E. M. Lifshitz. *Landau and lifshitz course of theoretical physics volume 7: theory of elasticity*. Butterworth Heinemann, New Delhi, 3rd edition, 1986.

[23] Sepideh Bazazi, Karin S Pfennig, Nils Olav Handegard, and Iain D Couzin. Vortex formation and foraging in polyphenic spadefoot toad tadpoles. *Behavioral ecology and sociobiology*, 66(6):879–889, 2012.

[24] John Toner, Yuhai Tu, and Sriram Ramaswamy. Hydrodynamics and phases of flocks. *Annals of physics*, 318(1):170–244, 2005.

[25] Hanshuang Chen and Zhonghuai Hou. Noise-induced vortex reversal of self-propelled particles. *Physical review e*, 86(4):041122, 2012.

[26] Christine Mohr, T Landis, HS Bracha, and P Brugger. Opposite turning behavior in right-handers and non-right-handers suggests a link between handedness and cerebral dopamine asymmetries. *Behavioral neuroscience*, 117(6):1448, 2003.

[27] Motonari Isobe, Dirk Helbing, and Takashi Nagatani. Experiment, theory, and simulation of the evacuation of a room without visibility. *Physical review e*, 69(6):066132, 2004.

[28] Mehdi Moussaïd, Dirk Helbing, Simon Garnier, Anders Johansson, Maud Combe, and Guy Theraulaz. Experimental study of the behavioural mechanisms underlying self-organization in human crowds. *Proceedings of the royal society b: biological sciences*, 276(1668):2755–2762, 2009.

[29] Dirk Helbing, Illés Farkas, and Tamas Vicsek. Simulating dynamical features of escape panic. *Nature*, 407(6803):487–490, 2000.

[30] Leonardo E Silbert, Andrea J Liu, and Sidney R Nagel. Normal modes in model jammed systems in three dimensions. *Physical review e*, 79(2):021308, 2009.

7.5 Supplemental Information

7.5.1 Video metadata

A search on YouTube.com for the phrase "mosh pit" returns over 10^5 results. We watched over 10^2 videos that exhibited mosh pits and circle pits indicating that these collective behaviors are robust, reproducible, and largely independent of factors such as the musical subgenre, timing of performance, crowd size, arena size, suggestions from the band, time of year, and socioeconomic status of the moshers.

For the video shown in Fig. 7.2 of the manuscript, the following additional

data was available:

- Band: 36 Crazyfists
- Recorded on Dec. 4, 2008
- First of three bands performing
- Audience size $\sim 10^2$ attendees
- Venue: The NorVa, Norfolk, VA
- Venue capacity: 1,500
- Band encouraged moshing

For the video shown in Fig 7.4 of the manuscript, the following additional data was available:

- Band: Hatebreed
- Recorded on June 11, 2006
- Second of ten bands performing
- Audience size $\sim 10^5$ attendees
- Venue: Donington Park, Leicestershire, England
- Band encouraged moshing

7.5.2 PIV Analysis

To quantify the motion of moshers in videos filmed at heavy metal concerts, we used PIV analysis to measure the 2D velocity field on an interpolated grid.

In our analysis, we first correct for perspective distortions due to the camera position. This amounts to a linear transformation with two free parameters that define the skew angle and stretching factor. In turn, these parameters are set by the camera height and tilt, and can be estimated by looking at stationary objects in the field of view. The PIV algorithm then breaks up each video frame of width w and height h into a square grid spaced by an amount Δ, which is described more below. Each square tile has area Δ^2 and is centered on a position $\langle x_i, y_j \rangle$ where $i = 1 \ldots \lfloor w/\Delta \rfloor$, and $j = 1 \ldots \lfloor h/\Delta \rfloor$. To determine the velocity associated with a given tile at position $\langle x_i, y_j \rangle$ in frame f_n, the region given by $x_i - 2\Delta \ldots x_i + 2\Delta, y_j - 2\Delta \ldots y_j + 2\Delta$ in frame f_{n+1} is examined. Within this larger region, all positions of overlap are examined and a local correlation function is calculated. The region of maximum correlation is generally offset from $\langle x_i, y_j \rangle$ to $\langle x_i + \chi_i, y_j + \upsilon_j \rangle$, which in turn defines the displacement vector $\langle \chi_i, \upsilon_j \rangle$ associated with a given tile. This process is iterated for all tiles in a given frame, and all consecutive pairs of frames.

Various values for Δ were tested ranging from approximately $\ell/5$ to 2ℓ, where ℓ is the characteristic feature size in a given video, i.e., the approximate width of a human. Grid sizes between to $\ell/3$ and 1.5ℓ were found to have no substantial effect on the measured velocity field: in this range, we found consistent statistical results independent of ℓ. Outside this interval, the algorithm failed to track the motion of tiles more than 35% of the time.

The algorithm was further tested with calibration videos wherein spherical objects were translated across the field of view with small random fluctuations in the orthogonal direction. In these tests, the motion was tracked and a series of digital "tracer particles" were placed in the measured flow field. The tracer

particle positions were updated frame-by-frame according to the locally measured velocity field. The algorithm was thus validated when we found that the tracer particles followed the test objects throughout the video.

7.5.3 Phase Separation

In the main text, we note that an initially uniform mixture of active and passive MASHers spontaneously phase separate. In our observations, we see that both mosh pits and circle pits can form spontaneously, which lead us to simplify our computations by beginning with initial conditions where a circular group of active MASHers are surrounded by passive MASHers. However, we find this phase separation behavior much more general and striking. Even after removing the flocking and noise forces, self-propulsion alone is able to drive the separation of active and passive MASHers. Also, depending on our parameters, different morphologies arise with time. As shown in Supplemental Fig. 7.5, we can arrive at well-defined vortices, stringing colonies of coherent active populations, winding pathways of gas-like states, and well-defined circular gas-like states. Note that MASHer color coding is identical to that of Fig. 7.3 of the main text.

This patterning is reminiscent of that seen in driven granular materials. For example, clustering of grains has been reported in experiments [1] in which grains of a single type are excited by vertical vibrations. These clusters are thought to form due to the effect of high densities on dissipation of kinetic energy. We hypothesize a similar situation arises in our MASHer model due to the difference in velocities between the active and passive populations.

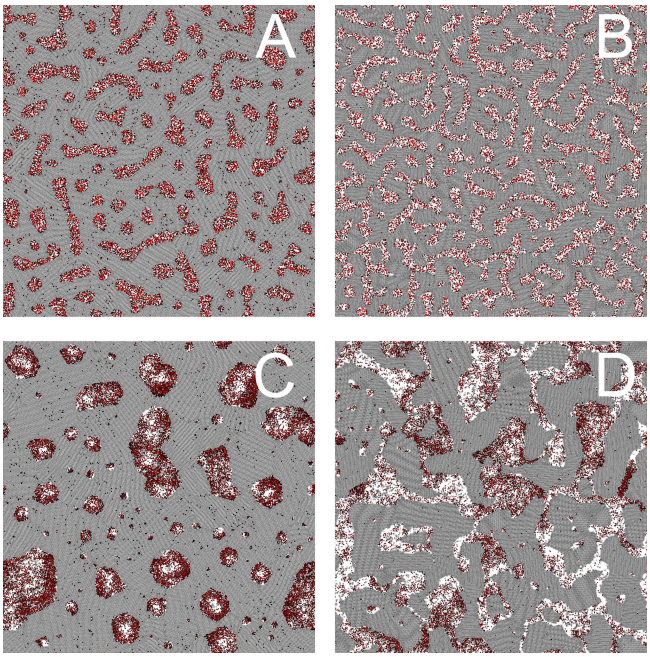

Figure 7.5: Simulations of 10^5 MASHers randomly assigned an active or passive status such that 30% were active reveal phase separation behaviors that vary with the model parameters. (A) and (B) have zero flocking and noise ($\alpha = \sigma = 0$), while (C) and (D) have finite flocking and noise ($\alpha = 0.25, \sigma = 1$). At zero flocking, we find more homogeneously distributed active MASHers within confined regions, whereas at finite flocking, we find larger density fluctuations due to flocking, which acts like a long-range attraction. (A) and (C) have a packing fraction of $\rho = 0.83$, while (B) and (D) have a packing fraction of $\rho = 0.69$. At higher packing fractions we see well confined groups of active MASHers, whereas at lower packing fractions, the active MASHers form a more network-like structure. All images represent the system after $\approx 10^4$ time steps, which is sufficient time for clusters of mosh/circle pits to coarsen and grow.

7.5.4 Expanded MASHer Phase Diagram

The phase diagram shown in Fig. 3 of the main text illustrates a region of gas-like and vortex-like collective motions by plotting the RMS angular momentum over a range of parameter values. Here, we expand on this plot (reproduced in Fig. 7.6(A)), by showing the standard deviation of the active MASHer angular momentum (Fig. 7.6(B)). We note that the largest fluctuations arise at high values of the flocking coefficient α relative to the values associated with vortex formation. Interestingly, this region in parameter space coincides with a region where the RMS linear momentum is also large (Fig. 7.6(C)). Simulations at high flocking and low noise demonstrate the formation of active MASHer lanes that push through the passive MASHers (Supplemental Movie 3). Indeed, fluctuations in the magnitude of the linear momeuntum (Fig. 7.6(D)) increase with the linear momentum illustrating that the lane mean free path shortens at higher flocking.

In the MASHer model, we found that setting the preferred speed of the active MASHers v_0 equal to zero suppressed both mosh and circle pits. While this region of parameter space appears to reflect a calm crowd, we must be careful when extrapolating a minimal flocking model, designed to explore the physics of collective motion, to real-world circumstances. For example, the model presented here does not account for (i) individual changes in moshing preferences, (ii) that people can fall down, or (iii) groups of people can be spatially coupled by social connections. While the MASHer model appears sufficient to predict large scale collective behavior, these additional features may be important for real-world applications such as crowd safety management.

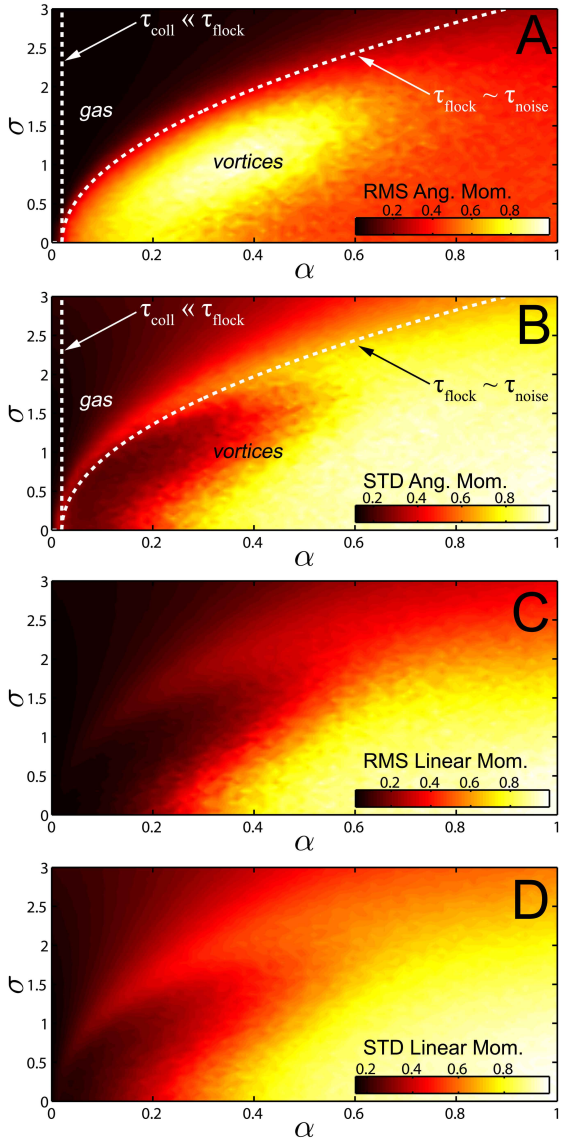

Figure 7.6: We show here additional features of the MASHer model in the region of phase space described in the main text. (A) Reproduction of the phase diagram in Fig. 3 of the main text showing the RMS angular momentum. (B) Standard deviation of the angular momentum with the identical contours from (A) superimposed. (C) Magnitude of active MASHer linear momentum illustrating a region of lane formation at high flocking and low noise. (D) Standard deviation of the linear momentum magnitude illustrating that fluctuations increase with the linear momentum. All order parameters have been normalized to their maximum value.

REFERENCES

[1] MV Sapozhnikov, IS Aranson, and JS Olafsen. Coarsening of granular clusters: two types of scaling behaviors. *Physical review e*, 67(1):010302, 2003.

CHAPTER 8

CONCLUSION

In this, the final chapter, we step back from the particulars of each project and look for broader lessons and open questions. Regarding broader lessons, the stark contrast between natural versus engineered materials is highlighted in this work. For example, in the projects that involved plants and cartilage, every sample grew of its own accord and was subject to essentially no external control. Consequently, it was impossible to vary the material properties of these living tissues in a rational manner, which for experimental purposes, would have been particularly useful. To overcome this limitation, we relied on biological variation to act as the knob that tunes these parameters, but even this was limited in range and reliability. Similarly with mosh pits, the experiments were inherently observational, and this generally limited the types of questions that could be asked or answered. Compared with the origami projects, where both material properties and geometric designs were trivially easy to vary, we find much greater control over the experiments. This enabled a whole host of questions to be addressed that wouldn't be as easily tackle in living systems.

Reflecting on the distinctions between natural and engineered materials leads us to wonder whether there is a rational way to modify material properties of living organisms. As it happens, recent developments in synthetic biology have begun to offer opportunities to accomplish exactly this. Through the manipulation of DNA, it is now possible to write genetic programs that have the ability to override cellular behavior. While this is generally demonstrated with apoptosis or expression of fluorescent markers, the same techniques could be used to control the structure and stiffness of biological tissues at a larger scale.

Indeed, this potential ability to "hack" a living organism opens vast new territory for studies of geometry, mechanics, and microstructure in the biological context.